NUMERICAL APPROACH FOR HYPERSONIC FLOW

Direct Simulation Monte Carlo in Reentry Flows

Erik Torres

Aeronautics and Aerospace Department, von Karman Institute for Fluid Dynamics, Belgium, erik.torres@vki.ac.be

Supervisor: Thierry Magin

Assistant Professor, Aeronautics and Aerospace Department, von Karman Institute for Fluid Dynamics, Belgium, thierry.magin@vki.ac.be

University Supervisor: Stefanos Fasoulas

Professor, Institute for Space Systems, University of Stuttgart, Germany, fasoulas@irs.uni-stuttgart.de

Abstract

The present project is focused on physical models applicable to the numerical simulation of rarefied gas flows. The main application considered in this work is the high-speed gas flow around vehicles returning from space at early stages of atmospheric entry. We to focus mainly on the improvement and extension of the physical models used with the most prevalent simulation technique for rarefied flows, the direct simulation Monte Carlo (DSMC) method. Specifically, the areas of interest include the high-fidelity modeling of internal energy exchange and chemical reaction processes occurring in the bulk gas, during its compression and heating in the bow shock region in front of the vehicle. The second topic to be studied is the influence of chemical reactions taking place at the surface of ablative materials on the gas flow.

Keywords: rarefied gas dynamics, RGD, reentry, hypersonics, direct simulation Monte Carlo, DSMC, non-equilibrium phenomena

1. Introduction

Taking into account rarefied gas effects is of importance in the correct prediction of the aerodynamic behavior of space vehicles entering a planetary atmosphere. A major factor in the success of such a mission is the correct determination of aerodynamic forces and moments affecting the stability of the vehicle. Under rarefied conditions the continuum description of the gas is no longer valid and traditional CFD techniques based on solving the Navier-Stokes equations produce inaccurate results. Nowadays, the preferred technique for the numerical simulation of rarefied flows is direct simulation Monte Carlo (DSMC). This is a particle-based method capable of describing the flow at a molecular level. It is very flexible in the sense that it can incorporate complex physical phenomena, such as excitation of internal energy modes and non-equilibrium chemistry directly into the collision algorithm.

As part of this doctoral project it was decided to implement a small DSMC code capable of handling simple one-dimensional flow problems, such as steady normal shock waves. After having used an existing DSMC software package (RGDAS) for preliminary studies in the previous year, it was concluded that restrictions in access to the sources and limited familiarity with the RGDAS code would prevent it from becoming a viable tool in the short term. This is the main reason for the development of the present code.

The first year of this project was dedicated to gaining familiarity with the subject matter of rarefied flows and with the DSMC technique. Several large-scale simulations of a classical reentry configuration (Apollo) were conducted to assess the capabilities of the method and to learn about properly setting the simulation parameters in order to obtain accurate results. The main effort in this second year of studies has been to go deeper into the details and implementation of already well-established models for inelastic collisions used in the DSMC method. For this purpose, a dedicated DSMC code has been written. It is capable of simulating simple one-dimensional, steady flow configurations, such as normal shock waves, as well as the unsteady relaxation of internal energy modes in an adiabatic heat bath. It has also been adapted for modeling stagnation streamline, as well as Couette-type flows. At present, it is capable of simulating rotational and vibrational energy exchange using the standard Larsen-Borgnakke model. The implementation of the Total Collision Energy (TCE) method for modeling chemical reactions is still underway. In this paper, several of the preliminary results obtained with this code are presented and, when possible, compared to experimental results.

This summary is organized as follows: Section 2 outlines some basic features of the code. This includes the physical models implemented so far, but also some details of the code itself. Then, in section 3, results for three different test cases are presented. They serve to highlight the present-day capabilities of the code. Finally, section 4 draws some conclusions and gives an outline of the work still to come.

2. Development of DSMC code

The initial reason for writing this DSMC code was the difficulty of simulating a simple normal shock wave in RGDAS. The RGDAS package is very powerful when it comes to simulating two- or three-dimensional external flows around complex body shapes. However, it does not include the capability of applying arbitrary boundary and initial conditions. This makes it very difficult to simulate the normal shock wave problem. One way to circumvent this issue was to simulate the flow around a blunt body (e.g. a cylinder in 2D, or a sphere in 3D) and to extract the flow properties along the stagnation stream line. However, this approach represents a huge waste of computational resources, because one always has to simulate a full 2D or 3D flow, for only a small amount of information required. Additionally, the stagnation stream line always includes interaction of the gas with the wall and prevents slow relaxation phenomena (i.e. taking place over long distances behind the shock) to be analyzed without interference of the wall.

2.1. Collision routines

Most of the core functions that make up the DSMC method are concerned with modeling intermolecular collisions. The collision step itself can be divided into several sub-steps. At the beginning of a collision step, every collision cell contains those particles which ended up in the given cell after completing the free motion step. Determining the correct local collision frequency is the first task in the collision step. In the code this is done using the No Time Counter (NTC) method, proposed by Bird [1].

The second step is the formation of random collision pairs within the cell. In the code, this is accomplished by arranging all particles in a list with a randomized sequence. Then, consecutive particles (i.e. particle 1 and 2, 3 and 4, etc.) will form collision pairs. The standard DSMC routines used in this code make no distinction between particles because of their location within a cell or their relative pre-collision velocities [1].

The next step in the collision procedure is determining whether a collision actually occurs between the previously defined pairs. In the NTC method, the probability of collision for a given pair is calculated from the expression:

$$P_{\text{coll}} = \frac{\sigma_T \cdot c_r}{\{\sigma_T \cdot c_r\}_{\max}}$$

where the product of the total collision cross section σ_T and the relative speed for each pair c_r is used in the numerator, while the maximum value for the cell is used in the denominator. In order to calculate the total cross section, a model for the intermolecular potential needs to be defined. The most widely used ones today in DSMC are arguably the Variable Hard Sphere (VHS) and Variable Soft Sphere (VSS) models, introduced by Bird [4] and Koura [5] respectively. Both of these models have been implemented in the code.

2.2. Internal Energy model

One of the main reasons for developing the present code is the study of internal energy exchange and other inelastic collision processes, such as chemical reactions in highly non-equilibrium flows, e.g. behind normal shock waves. Over the years, a considerable amount of effort has been invested into the development of models for internal energy exchange in DSMC. See, for example, the work of Haas et al [6], [7]. These papers, along with a contributions by Lumpkin [8], Boyd [9; 10; 11] and Bergemann [12] helped to establish the Larsen-Borgnakke [13] model as the most widely used one in the DSMC community nowadays. Most of the details of the method are explained thoroughly in Bird's reference text [14]. It

---

[1] Several DSMC implementations use the relative distance between particles for selecting collision pairs, see [2], [3]

is worth mentioning that the current implementation in the code assumes a continuous distribution of energy in the rotational mode and a quantized energy distribution of the vibrational levels. These vibrational levels are based on the simple harmonic oscillator (SHO) model of vibration. So far, these models have only been implemented for diatomic species, such as molecular nitrogen.

2.3. Boundary conditions

Another important aspect in the implementation of a DSMC code is the treatment of the boundaries. The current code allows for the application of so-called stream boundaries (i.e. flow inlets/outlets) and solid walls with either fully diffuse or fully specular reflection at the domain boundaries.

The stream boundaries are implemented using so-called "buffer cells". These cells are located outside of the flow domain, but immediately adjacent to the regular cells. They simulate a reservoir of particles with the correct Maxwell-Boltzmann equilibrium distribution of velocities and internal energies so as to be consistent with the macroscopic flow parameters imposed at the boundary. At the beginning of every time step, these buffer cells are filled with new particles. These particles are then displaced along with the ones already present inside the regular domain. Afterward, all particles which have crossed the boundaries into the domain are kept, whereas all particles lying outside of the boundaries are discarded.

Since the present code only allows for flow field gradients in one spatial dimension, walls reduce to a single point at the domain boundary and are necessarily oriented normal to the coordinate direction. For now, only the two most basic wall boundary conditions in DSMC are implemented: fully specular and fully diffuse reflection. They can be viewed as the two extremes between which all gas-surface interactions lie.

2.4. Mesh

In the current 1D code, the flow domain is divided into a group of equally-spaced cells. In this implementation a two-level grid is used, where sampling of macroscopic flow variables (such as density and temperature) occurs at the coarser level, the so-called sampling grid. The collision routines are implemented on the second level, also called the collision grid. Usually, a sampling cell contains one or more collision cells and the reason for this arrangement lies in the different resolution requirements for collision and sampling. Collision cells need to be made smaller than the local mean free path in the gas. This is crucial for the correct prediction of the local collision rate during the collision step. The sampling cells, on the other hand, are usually comprised of more than one collision cell. Using the the particles contained in several contiguous collision cells helps to increase the sample size for obtaining average macroscopic properties and will result in smoother flow field profiles. It should be noted, that the sampling cell size has no influence of the accuracy of the underlying simulation, as sampling does not influence the behavior of the particles. The sampling cell size is, thus only a function of the desired spatial flow field resolution.

At present, the sampling and collision grids need to be set by the user at the beginning of a simulation. Their sizes remain unchanged until the end of the run. This simple set up has been enough for the test cases considered so far (see section 3), because in most of these flow configurations the local mean free path can be estimated with sufficient accuracy beforehand, so as to provide a lower bound on the collision cell size. This is generally not the case for flows including obstacles to the flow (such as general 2D or 3D flows around solid bodies or the stagnation line flow). As a consequence, some form of automatic grid adaptation may need to be added to the code in the future.

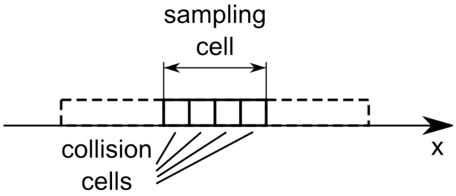

Figure 1: Two-level grid of sampling- and collision cells. There is always an integer number of collision cells, per sampling cell.

3. Results

In this section, the results of some simulations performed using the newly developed code, are presented. At the present time, the code is capable of simulating translational and internal energy relaxation in a cell, as well as in one-dimensional flows. Three test cases are mentioned in this paper, because of their relevance in testing several components of the code.

3.1. Normal shock wave in argon

One of the most simple flow configurations for studying non-equilibrium flow phenomena in gases, which can be simulated using a 1D code, is the normal shock wave. In order to be able to treat this phenomenon as a steady flow, it must be viewed in the shock frame of reference, i.e. the shock front remains stationary in space, while the incoming pre-shock equilibrium flow is supersonic and the post-shock equilibrium flow is subsonic. The relationship between pre-and post-shock flow conditions can be directly determined from the Rankine-Hugoniot normal shock relations. For non-reacting gas mixtures without vibrational excitation, these expressions have a closed, analytical form, allowing the calculation of post-shock density, temperature and velocity, as long as the pre-shock conditions are known.

Using the code, the simulations were set up as follows: The pre-shock flow conditions were taken to be equivalent to the ones studied by Alsmeyer [15]. In this paper, a number of density profiles were presented for normal shock waves in argon and nitrogen gas. These profiles were obtained from experimental investigations and are one of the few well-documented test cases to validate numerical simulations against. Alsmeyer reported profiles for argon at different Mach numbers, ranging from fairly low supersonic (M = 1.55) up to hypersonic (M = 9) speeds.

In the simulation set-up, both the pre- and post-shock conditions are imposed as boundary conditions at the left- and right-hand side of the flow domain. During the simulation, particles whose distribution functions conform to these conditions, are injected on both sides of the domain. At the beginning of the simulation, all the cells in the flow domain are already filled with particles. A specific location x_{step} separates two regions. To the left of it the flow is initialized at the pre-shock and to the right at the post-shock conditions. This initial condition fixes the initial shock location and "trips' the incoming supersonic flow to form the shock wave. After an initial transient phase, in which the shock structure is established, time-averaging of flow samples can begin. Time averaging is usually necessary in DSMC, because the number of particles in a given cell at a given time step is usually much too small to give accurate enough values for the macroscopic flow parameters. In order to obtain smooth profiles, the flow field samples need to be averaged over many time steps. Of course, this approach is only applicable to macroscopically steady flows.

A particularity of the normal shock wave problem is that, given the simulation set-up described before, the shock front location is not fixed in time. Since there is no solid obstacle holding the shock in place, it is possible for it to move from its initial position at x_{step} (sometimes referred to as random walk). This phenomenon has been observed in the present simulations and causes problems for time-averaging of flow samples. If such samples are taken over a large enough number of time steps, the shock front will have moved from its initial location. Consequently, the time averaged flow fields will be inaccurate, because of the "smearing out" of the shock front. There seems to be no direct solution to this problem. A way to minimize this effect is, of course to reduce the sampling time. Then, in order to compensate for the lower number of time-averaging steps, one may increase the number of particles per cell used in the simulation. This approach has been taken here and the number of particles per collision cell is on the order of several thousand, instead of the more usual ten to twenty particles per cell.

In the following, results for two different Mach numbers are shown. Figure 2(a) shows the density profile in a Mach 1.55 normal shock wave, with figure 2(b) presenting the corresponding profiles for the translational temperature components. The components of translational temperature in coordinate direction "i" is defined as:

$$T_{\mathrm{t},i} = \frac{m}{\mathrm{k}} \overline{(c_i - c_{0,i})^2}$$

where m is the mass of a single particle, k is the Boltzmann constant, c_i represents the i-component of velocity of a particle and $c_{0,i}$ the corresponding component of the hydrodynamic velocity. The over-bar symbolizes the average taken over all particles in the sample (i.e. the cell). The scalar translational temperature is then the average of all three components:

$$T_{\mathrm{t}} = \frac{1}{3}\left(T_{\mathrm{t},x} + T_{\mathrm{t},y} + T_{\mathrm{t},z}\right)$$

It can be seen in figure 2(b) that the different components of translational temperature do not exactly lie on top of each other inside the shock wave, as expected. This shows the degree of translational non-equilibrium locally present in the flow. The x-component of translational temperature has a small overshoot over the post-shock equilibrium value, while the temperature components normal to the flow direction (i.e. $T_{t,y}$ and $T_{t,z}$) lag behind. The flow then "relaxes" to the post-shock equilibrium where all temperature components take on the same value.

The degree of translational nonequilibrium at a given position in the flow field can also be observed as a departure from the local equilibrium velocity distribution function (i.e. Maxwell VDF) f_0:

$$f_0\left(c_x, c_y, c_z\right) = \left(\frac{m}{2\pi k T}\right)^{3/2} \times$$
$$\times \exp\left[-\frac{m}{2kT}\left((c_x-u)^2 + \left(c_y - v\right)^2 + (c_z - w)^2\right)\right]$$

Here, c_x, c_y and c_z are the molecular velocities in the x-, y- and z-directions respectively, with u, v and w the corresponding average flow velocities. The shape of the velocity distribution also depends on the mass m of the molecules and the local temperature T. If the distribution is symmetric in the y- and z-directions (as is the case for all 1D flows considered here), one may integrate f_0 over these two velocity components to obtain a "reduced" expression dependent only on c_x:

$$\Phi(c_x) = \int_{-\infty}^{\infty}\int_{-\infty}^{\infty} f_0\left(c_x, c_y, c_z\right) dc_y\, dc_z$$
$$= \left(\frac{m}{2\pi k T}\right)^{1/2} \exp\left[-\frac{m}{2kT}(c_x - u)^2\right]$$

Figure 2(c) shows these reduced velocity distribution functions for the x-components of molecular velocity at three different locations in the flow. The lines represent the VDF's obtained from the simulation, while the symbols show the theoretical Maxwell equilibrium distribution functions at the pre-shock and post-shock temperatures respectively. It can be seen that they match up very well with the simulation results. A third curve (the long dashed line) shows the VDF at a location "inside" the shock wave, approximately at the center of the shock, i.e. where the density is halfway between pre- and post-shock. It can be seen that the VDF is somewhere "between" the two equilibrium values. The location of the maximum of the VDF curves on the velocity axis corresponds to the hydrodynamic velocity at that particular location in the flow. It can be seen that it shifts from its pre-shock value of $500\,\mathrm{m\,s^{-1}}$ to the post-shock $280\,\mathrm{m\,s^{-1}}$. The temperature is related to the "width" of the distribution and this too shifts from a "narrow" curve at 300K, pre-shock, to a "wider" one at the post-shock temperature of 464.32K. Overall, at this Mach number the degree of translational non-equilibrium in the flow is fairly mild, and the distribution seems to remain near equilibrium throughout the shock. This seems to be a reason why Navier-Stokes equations are able to provide reasonably accurate solutions to the shock wave problem at low supersonic Mach numbers.

The other extreme of the cases investigated is the flow with an incoming Mach = 9. From the density profile in figure 3(a), one can immediately notice that the density ratio (post- to pre-shock) is much higher in this case. However, the density profile shape does not appear to be very different from the one at $M = 1.55$. The shock thickness is of the same order of magnitude. The differences are more pronounced when comparing the temperature profiles. In figure 3(b), the degree of translational non-equilibrium is evident, with $T_{t,x}$ showing an overshoot of more than 2000 K over the post-shock equilibrium temperature. The contrast with the low-speed case considered before is even more noticeable in figure 3(c). Now, the pre- and post-shock temperatures differ widely from one another (300 K vs. 7856 K) and the velocity distribution behind the shock widens and flattens out considerably as a result. At the center of the shock wave, the velocity distribution is now far from the typical Maxwell form. It is almost a bimodal distribution, with one "maximum" in the curve located near the pre-shock velocity and another closer to the post-shock velocity.

Figures 4(a) and 4(b) show a comparison of the density profiles obtained with the code with those reported by Alsmeyer. In general, there appears to be good agreement between the two sets of data. In these plots, the density has been normalized:

$$\rho' = \frac{\rho - \rho_1}{\rho_2 - \rho_1}$$

where the number index refers to pre-shock (ρ_1) and post-shock (ρ_2) conditions respectively. The abscissa has been normalized by use of the pre-shock mean free path λ_1. This highlights an important point. For the simple cases where non-reacting monoatomic gases are used, normal shock wave profiles have a general shape, only dependent on the Mach number. If the previous normalization is used, the exact conditions of pressure and temperature in the experiment should not affect the shape of the profiles. Thus, it is possible to match the results of experiments or simulations obtained at different free-stream densities.

From the two figures, one can argue that there is a good match between the experimental and DSMC results. It should be mentioned that the shape of shock wave obtained with DSMC is very sensitive to the viscosity model used and its dependence on temperature. In DSMC, the standard is to have a viscosity law such as:

$$\mu(T) = \mu_{\text{ref}} \left(\frac{T}{T_{\text{ref}}} \right)^{\omega}$$

where μ_{ref} is the viscosity of the gas known at a reference temperature T_{ref}. The exponent ω takes on values between 0.65 and 0.85 for most gases and is obtained from fitting this simple expression to experimental data. Depending on the temperature range of the fit, it can vary substantially, even for the same gas. In the simulations presented here, a value of $\omega = 0.72$ was used, which seems to give the best results for the "high" temperatures encountered in the post-shock regions. The value of $\omega = 0.81$ given by Bird in his book [14] is intended for low temperatures ($T_{\text{ref}} = 273$ K) and gives poor results in this case.

3.2. *Self-diffusion coefficient of argon*

In order to assess the behavior of the code when handling several species in the same flow, a simple test case was used. The details of the simulation parameters used can be found in section 12.5 of Bird's book [14]. Here, it is only important to mention that the flow set up consists of the domain bounded by two gas reservoirs. Both of these reservoirs are sources of argon gas at zero mean velocity and at the same temperature. The only difference between the two gases is that in the simulation they are labeled as different chemical species: "Argon blue" on the left and "Argon red" on the right. Besides this artificial difference, the molecules of both species behave exactly the same. The goal of this set up is to simulate the self-diffusion of argon and to determine the self-diffusion coefficient D_{11} from the results.

Figure 5(a) shows the species partial densities ρ_i of "Argon blue" and "Argon red", as well as the total density along the domain length. As expected, the concentration profiles are linear, with the highest concentration of each component near its "source". Due to the symmetry in the set up, at the center of the domain both components are present in exactly the same concentration. It can be seen that there is a small "concentration jump" at both boundaries for both components, i.e. the fraction of "Argon blue" is not exactly equal to 100 % at the left boundary and it does not drop to exactly 0 % at the other end. This is a result of the finite number of sampling cells used.

In figure 5(b) the diffusion velocities U_1 and U_2 are plotted for "Argon blue" and "Argon red" respectively. The diffusion velocity of species "i" is defined as:

$$U_i = \overline{u_i} - u_0$$

with $\overline{u_i}$ being the average over all particle velocities of species "i" in the sample and u_0 the momentum-average (i.e. hydrodynamic) velocity. The diffusion velocity for each species is nearly zero in the region where it is the main component of the mixture, but increases substantially at the other extreme of the domain. Again, since both "species" have exactly the same molecular properties, the picture is symmetric, i.e. the magnitudes of the diffusion velocities are mirrored along the x-axis.

The diffusion coefficient in a binary mixture, with concentration gradients in one dimension, can be determined from the expression:

$$D_{12} = -(U_1 - U_2) \frac{n_1 n_2}{n^2} \frac{dx}{d(n_1/n)}$$

where n_1 and n_2 are the number densities of "Argon blue" and "Argon red" respectively. Since both of these "species" have exactly the same molecular properties, this is also the self-diffusion coefficient D_{11}.

As indicated in figure 5(c), the average self-diffusion coefficient over the length of the domain is $2.89\,\text{m}^2\,\text{s}^{-1}$ (straight dashed line). This rather large value is a consequence of the low density specified in the simulation conditions. The diffusion coefficient is directly dependent on the number density and, converting it to standard conditions (i.e. $T = 273\,\text{K}$ and $p = 101325\,\text{K}$) gives a value of $1.51 \times 10^{-5}\text{m}^2\,\text{s}^{-1}$. This is in fairly good agreement with the value of $1.55 \times 10^{-5}\text{m}^2\,\text{s}^{-1}$ reported by Bird.

3.3. *Normal shock waves in nitrogen*

After being able to simulate a normal shock in a monoatomic gas such as argon, the next challenge is to move towards adding internal modes of energy, as is the case for molecular nitrogen. Before studying an actual shock wave, the internal energy exchange routines were tested in a single adiabatic cell (sometimes called a "0D" configuration). Unlike any of the other simulations presented in this summary, this is the only situation, in which the time-dependent evolution of the system is considered, meaning that all samples taken at a given time step are instantaneous and not time-averaged. This fact implies that instead of the usual 10-20 particles per cell, now up to several million particles need to be used in the cell, in order to provide accurate enough statistics.

The simulation setup is fairly simple. All particles in the cell are initialized with their translational and internal energy distributions corresponding to different temperatures, i.e. the translational, rotational and vibrational temperatures are not the same at $t = 0$. This, clearly is a situation of thermal non-equilibrium and, given enough time, the intermolecular exchange processes should force the gas to “relax” towards thermal equilibrium, i.e. a common temperature: $T_\mathrm{t} = T_\mathrm{r} = T_\mathrm{v}$. Thus, the first requirement is that all temperatures reach a single value at some time long after the process has started, while conserving the sum of energy contained in the translational and internal modes. The second requirement is that this relaxation process take place at the correct rate. This relaxation rate is usually defined in terms of the characteristic numbers for rotation and vibration (Z_r and Z_v) respectively. These numbers are used both in DSMC and in CFD codes to calculate local relaxation rates. It is important that the numbers be defined in a mutually consistent manner between DSMC and CFD. (This is not always the case. In the early years of DSMC, the definitions of Z_r and Z_v differed from those used in continuum CFD at the same time. As a consequence, the results would show poor correspondence between each other. This issue was already addressed in two papers by Haas [7] and Lumpkin [8]).

In figures 6(a) and 6(b), the time evolution of the different temperatures is shown for two different initial conditions. In the first case, the initial translational temperature was set equal to 2000 K, while the rotational temperature was initialized at 300 K. At such low temperatures, the vibrational mode is barely excited and therefore not considered. One can see in figure 6(a) that the two curves representing translational and rotational temperature approach each other over time, until they merge at around $t = 2.5 \times 10^{-9}$ s. After this time, the temperature in the cell remains at 1320 K, the expected equilibrium temperature. Along with the lines representing the results of the DSMC calculations, symbols show the same information, but obtained with a Navier-Stokes code. The close correspondence of both sets of results confirms the correct implementation of the rotational collision number in the DSMC code. A second simulation was conducted at a higher overall energy level, which now made the inclusion of the vibrational mode necessary. Figure 6(b) shows the time evolution of a gas reservoir initially at $T_\mathrm{t} = 10000$ K and $T_\mathrm{r} = T_\mathrm{v} = 300$ K. Again, this simulation shows relaxation of all thermal modes to the equilibrium temperature and a close match between the DSMC and Navier-Stokes results. The behavior is typical of rotation-translation and vibration-translation relaxation processes in a gas, where the rotational mode reaches equilibrium with the translational mode much faster than the vibrational mode does. It should be mentioned that in all simulations presented in this section, the collision numbers for rotation and vibration have been set to constant values: $Z_r = 10$, $Z_v = 120$. It is known that in reality these numbers show a temperature dependence, especially Z_v can increase several orders of magnitude for higher temperatures. Therefore, the results shown here may not provide the correct relaxation times one would observe in experiment. In order to achieve this, the collision numbers must be calculated according to the well-known empirical correlations by Parker [16], Millikan & White [17] and Park [18]. Implementation of these correlations into the code is still ongoing.

Figure 7(a) shows the normalized density profile in a Mach 1.71 shock wave of molecular nitrogen. Again, the density profile is compared with the experimental data given by Alsmeyer and the correspondence is seen to be very good. In figure7(b), the temperature profile is plotted. The solid line represents the translational temperature, whereas the dashed line shows the rotational temperature lagging behind. Once again, the symbols represent results obtained with a Navier-Stokes code. For this relatively low Mach number of 1.71, the correspondence between the DSMC and CFD results is very good. However, this picture is expected to deteriorate for higher Mach numbers, as the Navier-Stokes equations are known to give inaccurate results for strong non-equilibrium flows.

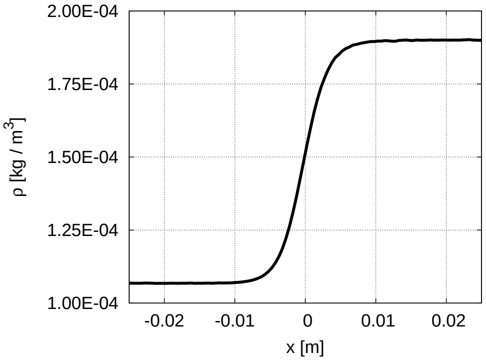

(a) Density profile

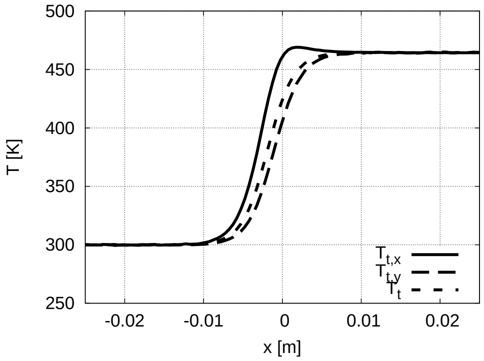

(b) Translational temperature profiles.
solid line: $T_{t,x}$,
dashed long: $T_{t,y}$,
dashed short: T_t

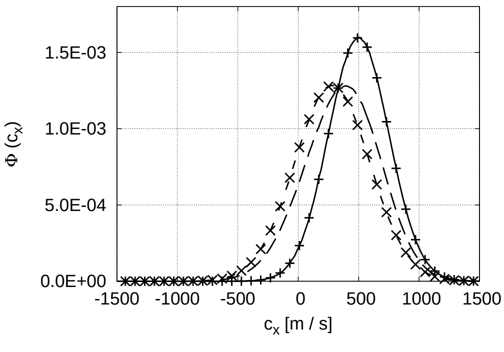

(c) Velocity distribution functions (VDF) for the x-velocity component.
solid line: DSMC at inlet (x = −0.05 m),
dashed long: DSMC at shock center (x = 0.0 m),
dashed short: DSMC at outlet (x = 0.05 m)
+: Maxwell for $T = 300$ K
×: Maxwell for $T = 464.32$ K

Figure 2: Macroscopic flow parameters and Velocity distribution functions for a normal shock wave in Argon, at Mach = 1.55

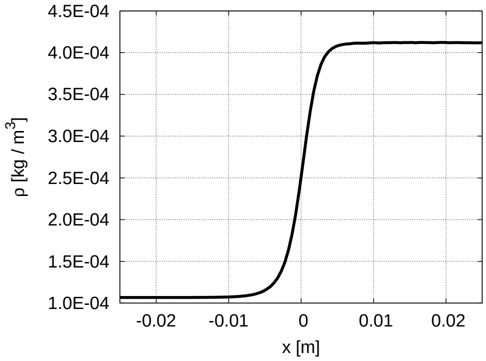

(a) Density profile

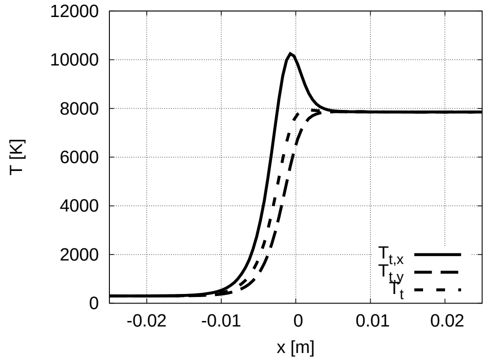

(b) Translational temperature profiles.
solid line: $T_{t,x}$,
dashed long: $T_{t,y}$,
dashed short: T_t

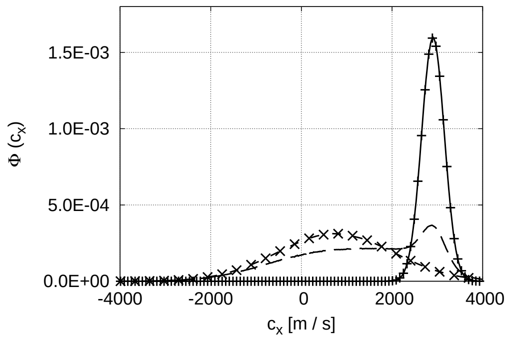

(c) Velocity distribution functions (VDF) for the x-velocity component.
solid line: DSMC at inlet (x = −0.05 m),
dashed long: DSMC at shock center (x = 0.0 m),
dashed short: DSMC at outlet (x = 0.05 m)
+: Maxwell for $T = 300$ K
×: Maxwell for $T = 7855.56$ K

Figure 3: Macroscopic flow parameters and Velocity distribution functions for a normal shock wave in Argon, at Mach = 9

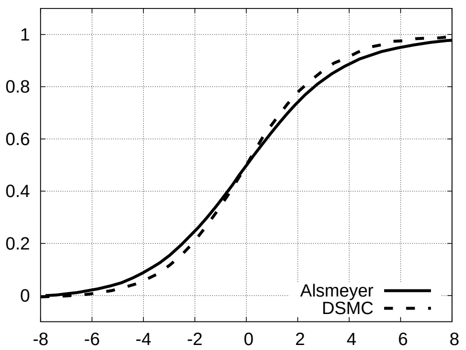

(a) Mach = 1.55

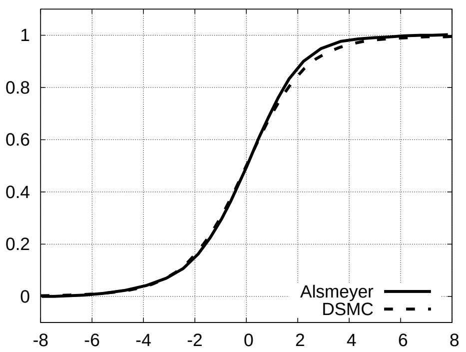

(b) Mach = 9

Figure 4: Comparison of normalized density $((\rho - \rho_1)\,/\,(\rho_2 - \rho_1))$ profiles between DSMC (dashed line) and experimental results obtained by Alsmeyer (solid line). The abscissa has been normalized with the free-stream mean free path λ_1

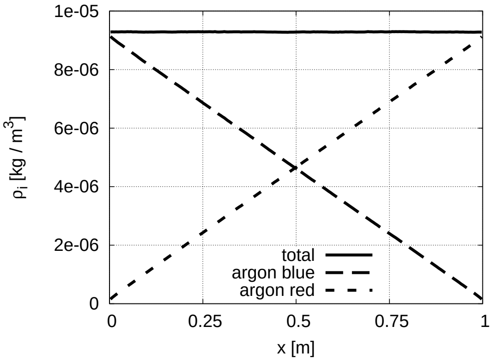

(a) Density profiles

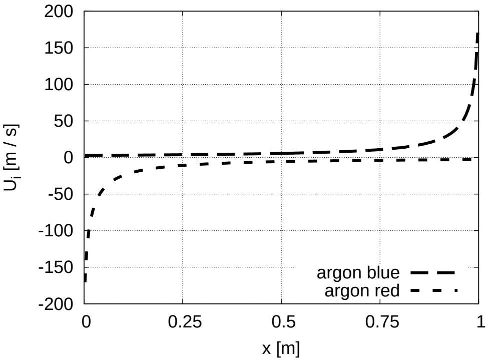

(b) Diffusion velocities

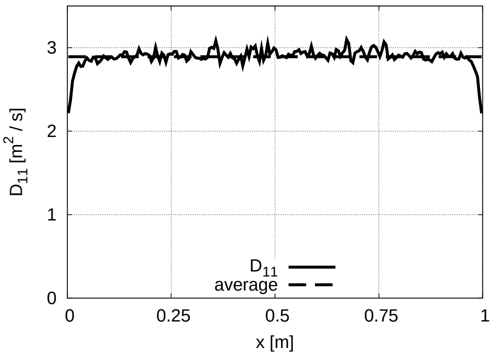

(c) Self diffusion coefficient

Figure 5: Profiles of density and diffusion velocity for a binary mixture of argon gas

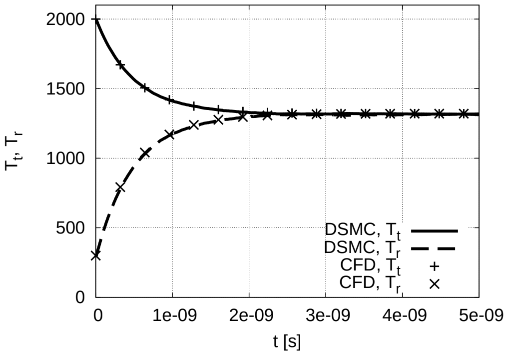

(a) R-T relaxation of N_2, time evolution of translational and rotational temperatures, comparison between DSMC and continuum CFD formulation

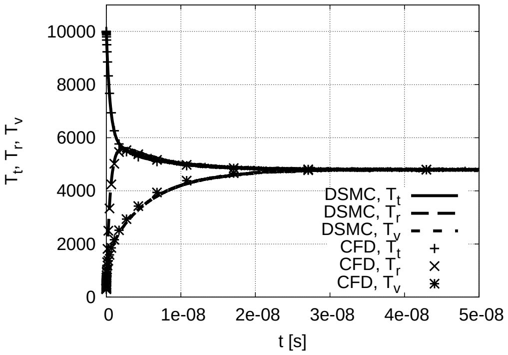

(b) R-T and V-T relaxation of N_2, time evolution of translational, rotational and vibrational temperatures, comparison between DSMC and continuum CFD formulation

Figure 6: Relaxation of internal energy modes of molecular nitrogen in an adiabatic heat bath for $Z_r = 10$ and $Z_v = 120$

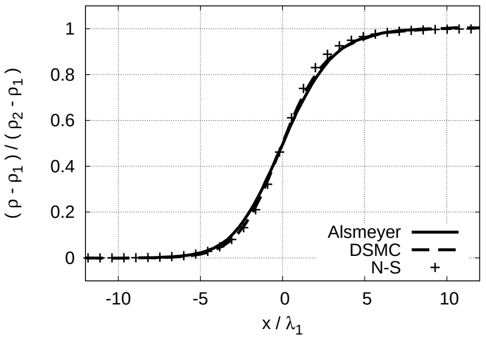

(a) Density

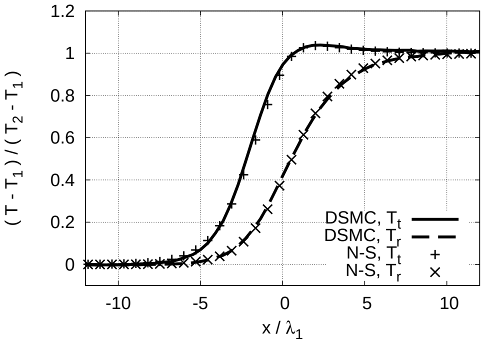

(b) Translational and rotational temperatures

Figure 7: Profiles of normalized density and temperature for a nitrogen Mach = 1.71, comparison between DSMC solution and continuum CFD based on Navier-Stokes

4. Conclusions and Future work

Some selected results obtained during the last year with a newly written DSMC code have been presented. The main elements of the code are functioning and it is possible to obtain accurate results with it for a number of test cases. Specifically, steady flow with a high degree of translational non-equilibrium, as in normal shock waves with monoatomic gases can be simulated. The treatment of internal energy exchange processes, present in all polyatomic gases, such as rotational-translational and vibrational-translational relaxation has been implemented using the standard model of DSMC [13].

However, work on the conventional models for internal energy exchange and especially for chemical reactions has not yet been completed. The inclusion of temperature-dependent rotational and vibrational collision numbers Z_r and Z_v, based on the empirical correlations of Parker, Millikan & White and Park has been implemented, but not yet thoroughly tested. The implementation of the TCE method for chemical reactions has yet to be started. Another topic, which will become relevant in reacting multi-species flows is the use of species-specific weighting factors. Instead of having a global value for the ratio of real to simulated particles F_{Num}, weighting factors result in individual F_{Num}'s for each component of the mixture. The inclusion of this feature should improve the treatment of trace species in the flow, which might often not be accounted for, due to the limited number of particles used.

So far, the computational performance of the code has been of secondary importance. The problems considered until now were rather manageable in terms of CPU run-time and memory usage, such that a serial implementation provided enough performance. However, it has been recognized, that as the problem size grows (specifically, the number of particles needed), significant improvements in speed and code efficiency have to be realized. This includes optimization of the code, as well as adding parallel processing capabilities. This work is underway.

Finally, it is important to mention that the main reason for the development of the code is still its future use with novel models for inelastic collision processes. In the future, the aim is to improve the existing models in DSMC for rotational and vibrational exchange by using a reduced model developed from a detailed chemical mechanism based on rovibrational cross sections for reactions in nitrogen. These models will be based on the cross sections for the N_2 + N system obtained from detailed quantum mechanical calculations obtained at NASA Ames Research Center. The N_2 + N system consists of approximately 10000 rovibrational levels and its implementation in DSMC, even for simple types of flows, becomes a challenge, due to the large number of particles needed for populating the possible states in a realistic fashion. Consequently, our efforts will be directed towards developing a model for lumping together energy states lying close to one another and thus reducing the total number of levels required. A similar effort is already underway in developing such reduced models for continuum CFD solvers [19]. The final goal will be again to compare simulations between consistent CFD and DSMC models.

Acknowledgments

I wish to thank Prof. Tom Schwartzentruber from the University of Minnesota for his advice and for providing reference material, which has been invaluable in developing the present DSMC code. Many thanks also to Alessandro Munafò for providing continuum CFD solutions for comparison.

References

[1] G. Bird, Perception of numerical methods in rarefied gasdynamics, in: 16th International Symposium on rarefied gas dynamics, 1988.

[2] G. LeBeau, K. Boyles, F. Lumpkin III, Virtual sub-cells for the direct simulation monte carlo method, in: 41st AIAA Aerospace Sciences Meeting and Exhibit, 2003.

[3] C. Su, K. Tseng, H. Cave, S. Wu, J, Y. Lian, T. Kuo, M. Jermy, Implementation of a transient adaptive sub-cell module for the parallel-dsmc code using unstructured grids, Computers & Fluids 39(7) (2010) 1136–1145.

[4] G. Bird, Monte-carlo simulation in an engineering context, in: 12 th International Symposium on rarefied gas dynamics, 1980.

[5] K. Koura, H. Matsumoto, Variable soft sphere molecular model for inverse-power-law or lennard-jones potential, Physics of Fluids A 3(10) (1991) 2459–2465.

[6] B. Haas, J. McDonald, L. Dagum, Models of thermal relaxation mechanics for particle simulation methods, Journal of Computational Physics 107 (1993) 348–358.

[7] B. Haas, D. Hash, G. Bird, E. I. Forrest, H. Hassan, Rates of thermal relaxation in direct simulation monte carlo methods, Physics of Fluids 6(6) (1994) 2191–2201.

[8] F. Lumpkin III, B. Haas, I. Boyd, Resolution of differences between collision number definitions in particle and continuum simulations, Physics of Fluids A 3(9) (1991) 2282–2284.

[9] I. Boyd, Rotational-translational energy transfer in rarefied nonequilibrium flows, Physics of Fluids A 2(3) (1990) 447–452.

[10] I. Boyd, Analysis of rotational nonequilibrium in standing shock waves of nitrogen, AIAA Journal 28(11) (1990) 1997–1999.

[11] B. Haas, I. Boyd, Models for vibrationally-favored dissociation applicable to a particle simulation, in: 29th Aerospace Sciences Meeting, 1991.

[12] F. Bergemann, I. Boyd, Rarefied Gas Dynamics: Experimental Techniques and Physical Systems (Progress in Aeronautics and Astronautics), American Institute of Aeronautics and Astronautics, 1994, Ch. 3. New Discrete Vibrational Energy Model for the Direct Simulation Monte Carlo Method, pp. 174–183.

[13] C. Borgnakke, P. Larsen, Statistical collision model for monte carlo simulation of polyatomic gas mixture, Journal of Computational Physics 18 (1975) 405–420.

[14] G. Bird, Molecular Gas Dynamics and the Direct Simulation of Gas Flows, Oxford University Press, 1994.

[15] H. Alsmeyer, Density profiles in argon and nitrogen shock waves measured by the absorption of an electron beam, Journal of Fluid Mechanics 74(3) (1976) 497–513.

[16] J. Parker, Rotational and vibrational relaxation in diatomic gases, Physics of Fluids 2(4) (1959) 449–462.

[17] R. Millikan, D. White, Systematics of vibrational relaxation, Journal of Chemical Physics 39(12) (1963) 3209–3214.

[18] C. Park, Nonequilibrium hypersonic aerothermodynamics, Wiley, New York, 1990.

[19] T. Magin, M. Panesi, A. Bourdon, R. Jaffe, D. Schwenke, Coarse-grain model for internal energy excitation and dissociation of molecular nitrogen, submitted to Chemical Physics.

In-flight Experiment Design and Ground Testing of a Re-Entry CubeSat

Işıl Şakraker

Aeronautics and Aerospace Department, von Karman Institute for Fluid Dynamics, Belgium, isil.sakraker@vki.ac.be

Supervisor: Olivier Chazot

Associate Professor, Aeronautics and Aerospace Department, von Karman Institute for Fluid Dynamics, Belgium, chazot@vki.ac.be

University Supervisor: Gaëtan Kerschen

Professor , Department of Aerospace and Mechanical Engineering, University of Liege, Belgium, g.kerschen@ulg.ac.be

---

Abstract

Spacecraft, returning back to Earth, experience a very harsh environment during the re-entry. One of the major issues of the re-entry is the extreme aerodynamic heating and the exothermic chemical reactions due to the gas-surface interaction at hypersonic free stream velocities. There is a constant effort by the space agencies to increase the understanding of the re-entry flight dynamics to optimize the spacecraft design. The re-entry phenomena are investigated using three powerful tools with their advantages and inconveniences: flight tests, numerical simulations and ground testing. The most valuable among all is the real flight testing however they come with very high costs and they have to be designed with ground tests. Different from low speed aerodynamics, high enthalpy flows cannot be fully simulated on ground but only partial simulations are possible. The approach at VKI is the Local Heat Transfer Simulation (LHTS) which says that the stagnation region behind the shock can be simulated only if the total pressure and the boundary layer edge enthalpy and velocity gradient are reproduced.

The first part of this study is to develop methods the **Plasmatron flow characteristics** eventually to make sure the boundary layer edge and velocity gradient are kept. Two methods are initially proposed: free stream temperature measurement by emission spectroscopy and direct enthalpy measurement. Subsequently an **Aerothermodynamic Database** will be built and an envelope, where the mission trajectory will later be imposed, will be defined to develop Gas-Surface Interaction models for further design steps. The last step is then called **Flight Extrapolation** where the ground test conditions are pinpointed to the mission flight trajectory. The reference mission of this study is VKI's QARMAN (QubeSat for Aerothermodynamic Research and Measurements on Ablation) in the framework of QB50. Different from the rest of the QB50 satellites, the Re-Entry CubeSat is a double CubeSat, with an extra ablative thermal protection system (TPS) unit, resulting in the external dimensions of a triple CubeSat.

The major scientific return of QARMAN project is the contribution of flight data on an Earth re-entry trajectory by a very low cost mission compared to other similar missions such as ARD, EXPERT, IXV, etc. The re-entry conditions of QARMAN are representative of a real spacecraft re-entry (starting altitude of 120 km, V=7.5 km/s and $q \geq 2MW/m^2$). It is the first time that such a low-resource vehicle will be used for re-entry studies.

Several important issues at different phases of the re-entry flight are the starting points of the scientific questions that will be answered through the PhD study. The phenomena under consideration are: Aerothermodynamic environment, thermal protection system, gas-surface interaction (mainly ablation), telecommunications blackout, different stability regimes, turbulence effects, radiation, rarefied flow aerodynamics, atmospheric effects, stability, attitude control and controlled re-entry, disintegration, subsystem functionality and safety aspects. Using the ground testing methodology developed in the first part, it is aimed to investigate how those phenomena can be measured during the flight on such a constraining platform. The goal is propose eventually a flight qualified payload for in-flight experiment.

Mission Analysis and Design of a CubeSat Network

Thorsten Scholz

Aeronautics and Aerospace Department, von Karman Institute for Fluid Dynamics, Belgium, scholz@vki.ac.be

Supervisor: Patrick Rambaud

Associate Professor, Aeronautics and Aerospace Department, von Karman Institute for Fluid Dynamics, Belgium, rambaud@vki.ac.be

Co-Supervisor: Cem O. Asma

Research Engineer, Aeronautics and Aerospace Department, von Karman Institute for Fluid Dynamics, Belgium, asma@vki.ac.be

Keywords: QB50, satellite network, CubeSat, thermosphere, orbital dynamics, atmospheric model, DSMC

1. Motivation & Objectives

In the framework of the QB50 project a network of 50 CubeSats will be launched to perform in-situ measurements of the spatial and temporal variation of atmospheric properties in the lower thermosphere at an altitude of 350 km to 150 km [1]. The project will demonstrate the possibility of using the small satellites as efficient and low-cost technology demonstrators. QB50 will be the first simultaneously launched CubeSat network and helps in gaining a better understanding of such complex missions.

The choice for conducting measurements in the lower thermosphere is influenced by several factors and constraints. The atmospheric properties in this region and their relationship to Earth's climate and space-weather like sun storms are yet not well known. This leads to larger uncertainties in lifetime and trajectory simulations, which the recently uncontrolled re-entries of UARS, Rosat or Phobos-Grunt have shown. Another influence factor is the mitigation of space debri creation and fulfillment of the 25 year lifetime requirement. The performance envelope of the chosen launch vehicle Shtil-1.2, which shall provide sustained and low-cost access to Earth orbit, restricts the reachable maximum altitude and a trade-off between number of satellites and altitude has to be performed.

The PhD main tasks will be the assessment of the atmospheric and aerodynamic input data, the mission design for QB50 with focus on the orbital dynamics of the network of 50 CubeSats and finally analyzing of concepts for deorbiting of satellites.

The first task deals with the aerodynamic characterization of the CubeSats. The flow-field around the satellite will be obtained with DSCM simulations using the software RGDAS. A database with the aerodynamic coefficient for different altitudes, attitudes and configurations will be generated. For the simulations a proper knowledge of the atmospheric conditions is mandatory. Therefore a detailed analysis of different existing atmospheric models will be made to assess the variations in the density distribution and the composition. Since the properties in the lower thermosphere are not well known, the uncertainty quantification is an important factor for the latter mission design.

The mission design of QB50 will be challenging and include several points to be looked at. First the development of an suitable deployment strategy for the 50 CubeSats is mandatory to reduce the collision risk to a minimum. The deployment also effects the spreading and therefore the global distribution of the satellites. This will be analyzed to obtain a suitable strategy and spreading for the distributed measurements in the thermosphere. Simultaneously 6 degree of freedom simulations of the 50 CubeSats will be performed using the software STK[1] or ASTOS[2] to obtain the trajectories and the behavior of the network. The

---

[1] Satellite Tool Kit, Analytical Graphics, Inc.

[2] AeroSpace Trajectory Optimization Software, Astos Solutions GmbH

network will be analyzed in terms of necessary number of satellites for global measurements. The results from the previous studies of the atmosphere and aerodynamics of the CubeSats will be used to predict the orbital life-time. The communication with the ground stations will be investigated in terms of coverage and communication time. A study of the collision risk with other satellites or debris could be performed.

The third task of the PhD deals with the effect of deorbiting concepts on the trajectory. These concepts like sails, fins or tethers are experiencing increasing popularity. DSMC simulations for different concepts and types mounted on a CubeSat demonstrator should be performed. In addition to that, 6 degree of freedom trajectory calculations will be performed to investigate their efficiency and effects on lifetime.

If the CubeSats will be launched in time during this PhD, the obtained measurements and trajectories will be analyzed and compared with the results from the atmospheric study and the mission design. This will help to further improve the atmospheric models for the lower thermosphere.

2. Challenges & Uncertainties

The challenge in the mission design of QB50 consists of the large number of parameters, the interconnection between them and their associated uncertainties. The proper prediction of the sun's activity for the launch time is difficult and only a crude statement according to the 11 year solar cycle can be made. Strong sun eruptions which are quite common during high activity periods can easily affect the lifetime of the CubeSats. Since the atmospheric models are based on the solar fluxes, the errors and uncertainties coming from the models will be amplified. Comparing different models, even with similar input, lead to discrepancies in terms of density values and global distribution. The inaccuracy for the density is still around 10 % to 15 % [2], even with the models improving over the last few years due to measurements obtained by the GRACE and CHAMP mission [3].

Since each CubeSat will be designed by a different university and the scientific payload will differ in terms of weight, size and external parts like additional sensors and communications links, the ballistic coefficient can not be assumed to be equal. The coefficient is also influenced by the satellite attitude and, most probably not all CubeSats will be perfectly aligned to the free-stream velocity direction. This results in varying atmospheric drag forces which have to be considered during the mission planing and especially for the deployment strategy.

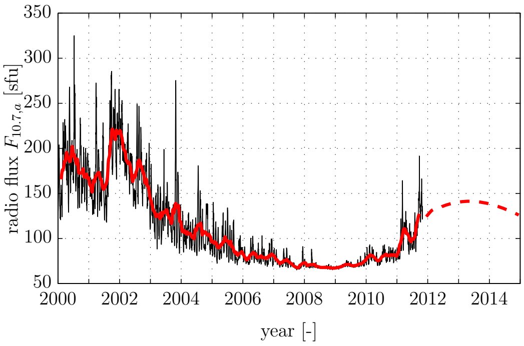

Figure 1: 10.7cm radio flux with prediction

3. Comparison of atmospheric models

Currently the two experimental models JB2008 and NRLMSISE00 and the physical model TIEGCM have been analyzed. The launch of QB50 is scheduled for the summer 2014 and the input values have been chosen according to the prediction for this date, e.g. shown in Fig. 1. The deviation of the prediction has been coupled with the $1\,\sigma$ standard deviation of a comparable situation in the past.

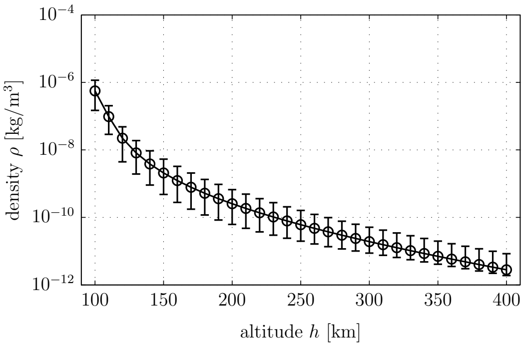

Figure 2: Density from US76 with obtained uncertainty

For the comparison all input parameters have been varied by the obtained deviations to simulate all realistic combinations. A horizontal grid resolution of 5^o and vertical resolution of 5 km have been used. The mean, maximum, minimum and the values of the daylight and night side of the earth have been calculated for each horizontal layer and then afterwards compared to the U.S. Standard Atmosphere US76. Combining the results of all models a possible uncertainty can be obtained for the density, shown in Fig. 2, or other values like neutral temperature.

Acknowledgments

The research leading to these results has received funding from the European Community's Seventh Framework Programme ([FP7/2007-2013]) under grant agreement n^o 284427 for the QB50 Project.

References

[1] J. Muylaert, QB50, an international network of 50 double CubeSats for multi-point, in-situ measurements in the lower thermosphere and for re-entry research, 1st QB50 Workshop (2009).

[2] D. A. Vallado, D. Finkleman, A Critical Assessment of Satellite Drag and Atmospheric Density Modeling, Revision to paper AIAA-2008-6442.

[3] B. R. Bowman, W. K. Tobiska, F. A. Marcos, C. Y. Huang, C. S. Lin, W. J. Burke, A New Empirical Thermospheric Density Model JB2008 Using New Solar and Geomagnetic Indices.

Development of Multiphysics Numerical Methods to Study Coupled Flow, Radiation, and Ablation Phenomena for Planetary Entry Vehicles

James B. Scoggins

Aeronautics and Aerospace Department, von Karman Institute for Fluid Dynamics, Belgium, james.scoggins@vki.ac.be

Supervisor and University Supervisor: Thierry Magin

Assistant Professor, Aeronautics and Aerospace Department, von Karman Institute for Fluid Dynamics, Belgium, magin@vki.ac.be
EM2C Laboratory, École Centrale Paris, France

Abstract

This report briefly outlines the proposed research of developing numerical methods for the coupling of fluid flow, radiation, and ablation physics surrounding planetary entry vehicles.

Keywords: multiphysics coupling, numerical methods, hypersonics, radiation, ablation, planetary entry

1. Introduction and Motivation

Space exploration is one of the boldest and most exciting endeavors that humanity has undertaken, and it holds enormous promise for the future. After the successful manned missions to the Moon and many probe entries in the atmospheres of our outer planets, our next challenges for spatial conquest include bringing back samples to Earth by means of robotic missions and continued manned exploration, which aims at sending human beings to Mars and returning them safely home.

Of the many design challenges associated with these goals is the exceptionally difficult task of accurately predicting the heat-flux to the surface of the spacecraft thermal protection system (TPS) during planetary entry. An inaccurate prediction can be fatal for the crew or the success of robotic missions. Large safety factors are often added to vehicle TPS thicknesses to avoid such catastrophes at the expense of additional cost, weight, and reduced payload margins. Thus it is necessarily important to understand and accurately model the complex phenomena that affect the surface heat-flux such as the following potential "mission killers:" 1) Radiation of the plasma in the shock layer, and 2) Complex surface chemistry on the thermal protection system material (Fig. 1). However, current entry vehicle design paradigms largely decouple many of the physico-chemical processes due to numerical and modeling constraints, making it difficult to infer from current design tools the complex, coupled phenomena occurring for any given entry problem. Thus, our poor understanding of the coupled mechanisms of flow, radiation, and ablation leads to the difficulties in flux prediction.

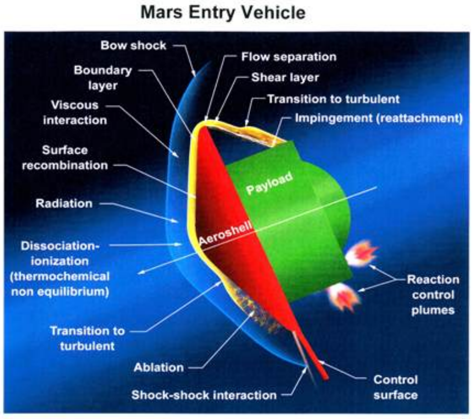

Figure 1: Diagram depicting physical phenomena surrounding a spacecraft during a Martian atmospheric entry. Credit: NASA Hypersonics Project [1]

2. Research Objectives

The AEROSPACEPHYS project is focused on improving our predictive capabilities by *"Integrating* *new advanced physico-chemical models and computational methods, based on a multidisciplinary approach developed together with physicists, chemists, and applied mathmaticians, to create a top-notch multiphysics and multiscale numerical platform for simulations of planetary atmosphere entries, crucial to the new challenges of the manned space exploration program. Experimental data will also be used for validation, following state-of-the-art uncertainty quantification methods.*" The proposed research project, aimed at developing a complete multiphysics tool which fully couples flow, radiation, and ablation models, will be an integral component of the overall objectives of the AEROSPACEPHYS project.

Currently, other researchers are working on state-of-the-art modeling capabilities for the various decoupled systems necessary for the accurate description of the flow physics associated with hypersonic flight [2]. These include the development of advanced collisional-radiative models for thermochemical nonequilibrium and radiation modeling via strong collaboration with the computational chemistry group at NASA Ames Research Center (ARC) [3; 4; 5], improved carbon-phenolic ablation models through Direct Simulation Monte Carlo methods [6], accurate and efficient modeling of atmospheric entry plasmas in the transition and continuum regimes, as well as a previously developed state-of-the-art treatment of transport properties for ionized plasmas [7; 8]. In addition to these advanced modeling efforts, an experimental investigation of various thermal protection materials is also under way with the use of the VKI Plasmatron facility [9; 10]. The next step in developing a complete multiphysics tool for studying hypersonic entries will be to couple these efforts, including contributions from outside VKI such as a new ablation code from NASA ARC (PATO [11]), into a comprehensive, 3-dimensional, multiphysics code which couples the various models being developed into a complete flow/radiation/ablation tool.

The development of this multiphysics framework will be completed through a series of important milestones during the research project at VKI. During the first phase, the Mutation library, which provides chemistry, transport, and equilibrium computations for ionized plasmas, will be upgraded to use C++ and incorporate improved algorithms and models for the transport and equilibrium calculations. The improved library will be designated Mutation++. Additionally, during the first phase of development, a 3-dimensional hypersonics CFD code will be implemented with the use of the OpenFOAM library. OpenFOAM is a natural choice because it offers extensive features to aid the development of a hypersonics solver including grid/mesh data structures, built-in parallel framework, and linear algebra routines. The flow solver will also make extensive use of Mutation++. Following this work, the task of coupling radiation into the flow solver will be completed alongside a detailed development of a general multiphysics framework for hypersonic problems. Next an ablation tool being developed by NASA ARC will be additionally coupled to the flow/radiation solver, finally allowing the computation of a fully coupled flow/radiation/ablation simulation.

Apart from improved simulation fidelity provided by the implementation of various physico-chemical models developed in the Aeronautics and Aerospace Department, the new multiphysics tool will finally allow a detailed study of the various coupled phenomena that have been largely overlooked due to lack of existing computational models. These include the coupled relationships between shock layer radiation and absorption by pyrolysis and ablation products in the boundary layer and gas-surface interactions and in-depth ablation due to boundary layer chemistry. The final goal of this research will be to study these effects as they pertain to specific experimental and flight test situations such as plasmatron simulations and post-flight analysis of the EXPERT mission (Fig. 2).

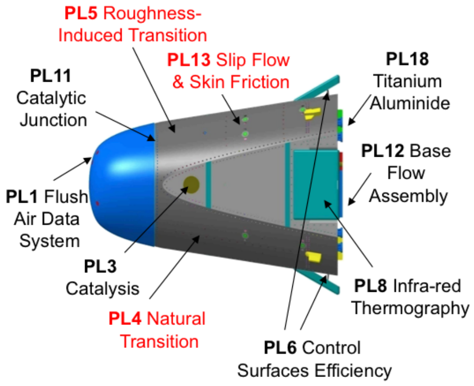

Figure 2: ESA Expert Vehicle & Payloads

3. Mutation++

As mentioned in Section 2, the first task in developing a complete multiphysics tool will be to update the Mutation library to a modern, object oriented library written in C++ which can be coupled to new or existing CFD tools. This effort is in fact already underway. The MUTATION library provides **mul**ticomponent **t**ransport **a**nd **t**hermodynamic properties/chemistry for **ion**ized plasmas.

MUTATION++ will incorporate all of the same features as its predecessor, however a number of algorithmic changes will be made to improve the library's robustness and performance. In particular, the equilibrium composition solver in MUTATION can fail for some mixtures and thermodynamic states for which the nonlinear set of equations to be solved becomes numerically stiff. Such conditions have been encountered in certain pyrolysis gas mixtures making it impossible to solve some boundary layer problems with ablation and pyrolysis species. MUTATION currently employees the Newton-Raphson iterative procedure to solve the set of equilibrium equations with the fast Schur complement method for the linear update. This algorithm has proven to be very fast, however it does not handle numerical stiffness well. MUTATION++ will instead implement a method known as the Gibbs function continuation (GFC) method developed by Pope [12; 13], which is guaranteed to find the equilibrium composition for all well posed problems regardless of the numerical stiffness of the mixture.

To help increase the performance of the MUTATION++ over its predecessor, specialized lookup tables will be incorporated for the calculation of expensive model parameters such as Arrhenius rates laws, equilibrium constants, collision integrals, etc. This lookup table feature has already been incorporated into the MUTATION++ library and can compute lookup tables at start-up given a function and desired accuracy (error tolerance) or can be loaded from precomputed tables. More testing is still required to determine the exact speedup generated by using such lookup tables but initial tests with randomly generated functions shows that an order of magnitude decrease in computational time can be achieved for some model parameter calculations.

Additional features will also be added in MUTATION++ which will enable coupling to implicit CFD solvers such as the calculation of the species production rate Jacobian matrix for finite-rate chemistry.

4. Concluding Remarks

The focus of this research will be to develop state-of-the-art numerical methods that allow the coupling of fluid flow, radiation, and ablation modeling for planetary entry simulations that is computationally competitive with current uncoupled methodologies. To this extent, the basic ground work has been laid through planning and collaboration internal to VKI and abroad. However, this research is still in the preliminary phases, leaving much work left to be completed.

Acknowledgments

This research is funded through a Fellowship provided by the European Research Council Starting Grant #259354: "*Multiphysics models and simulations for reacting and plasma flows applied to the space exploration program.*"

References

[1] Depiction of Marsian atmospheric entry. Web address: `http://www.aeronautics.nasa.gov/fap/hypersonic.html`.

[2] T. E. Magin, O. Chazot, Review of the vki research on nonequilibrium phenomena in hypersonics, AIAA (2012-725).

[3] A. Munafó, M. Panesi, R. Jaffe, A. Lani, T. Magin, Vibrational state to state kinetics in expanding and compressing nitrogen flows, AIAA (2010-4335).

[4] A. Munafó, M. Panesi, R. Jaffe, A. Bourdon, T. Magin, Mechanism reduction for rovibrational energy excitation and dissociation of molecular nitrogen in hypersonic flows, AIAA (2010-3623).

[5] A. Munafó, M. Kapper, J. Cambier, T. Magin, Investigation of nonequilibrium effects in axisymmetric nozzle and blunt body nitrogen flows by means of a reduced rovibrational collisional model, AIAA (2010-0647).

[6] E. Torres, A. Munafó, T. Magin, Influence of internal energy excitation and molecular dissociation on normal shock structure, 7th European Aerothermodynamics Symposium, Brugge, Belgium.

[7] T. E. Magin, G. Degrez, Transport of partially ionized and unmagnetized plasmas, Physical Review E 70.

[8] T. E. Magin, G. Degrez, Transport algorithms for partially ionized and unmagnetized plasmas, Journal of Computational Physics 198 (2004) 424–449.

[9] B. Helber, C. O. Asma, Y. Babou, O. Chazot, T. Magin, Experimental investigation of the material response of carbon composite ablators in the vki plasmatron facility, AIAA (2011-2302).

[10] B. Helber, Methodology for ablation investigations of innovative ablators in the vki plasmatron facility: First results on a carbon fiber preform, Ph.d. symposium report, von Karman Institute for Fluid Dynamics (2012).

[11] J. Lachaud, H. Wong, I. Cozmuta, G. Reinisch, Develpment and validation of a physics-based multi-scale model for low-density carbon/phenolic ablators, Step 2 proposal - hyp1-2. 2.1.2: High fidelity modeling of low-density carbon/phenolic ablators (edl), NASA-NRA (2011).

[12] S. B. Pope, The computation of constrained and unconstrained equilibrium compositions of ideal gas mixtures using gibbs function continuation, Report FDA 03-02, Cornell University (2003).

[13] S. B. Pope, Gibbs function continuation for the stable computation of chemical equilibrium, Combustion and Flame 139 (2004) 222–226.

Multidisciplinary Gradient-Based Optimization of Turbomachinery Components using CAD Parameterization

Lasse Müller

Turbomachinery and Propulsion Department, von Karman Institute for Fluid Dynamics, Belgium, lasse.mueller@vki.ac.be

Supervisor: Tom Verstraete

Assistant Professor, Turbomachinery and Propulsion Department, von Karman Institute for Fluid Dynamics, Belgium,
tom.verstraete@vki.ac.be.

Abstract

This PhD research aims to extend the VKI optimization system towards gradient-based algorithms to be utilized on turbomachinery components. Due to the industrial applicability, a CAD based parameterization will be used.

Keywords: Multidisciplinary Optimization, Gradient-Based Optimization, Turbomachinery Components, CAD

Over one decade of research has been conducted at the *von Karman Institute* (VKI) to develop a fully automatic multidisciplinary and multi-objective optimization system with focus on turbomachinery components (e.g. [1],[2],[3],[4],[5]). Evolutionary algorithms (EA), based on mechanisms found in nature according to the Darwinian theory such as mutation, crossover, and selection are used to find designs with minimal objective values ([6][7]). EA's have certain advantages [6] as they can handle non-differentiable, nonlinear, and multi-modal objective functions. These features make EA's particularly suitable to explore the complete design space without the risk of becoming trapped in a local minimum.

However, once the region of the global optimum within the design space is identified (see Fig. 1) gradient-based methods become attractive as they make directly use of the gradient of the objective function [8]. Moreover gradient-based methods provide the sensitivity of the gradients, i.e. the direction in which parameters need to be relocated to minimize the objective values. This is an important feed-back in the overall design process of turbomachinery components.

Regarding the terminology of CAD-based and CAD-free parameterization, a clear distinction is necessary. CAD-based parameterization refers to curves and surfaces defined by Bézier and B-Spline curves and surfaces [9], respectively. In CAD-free parameterization, surfaces are represented by the nodes of the surface mesh of the body. According to Fudge et al. [10] the CAD-free approach is intended for academic studies of relatively simple geometries, while the CAD-based system is suitable for geometries that are more complex and for industrial use. The CAD-based approach has certain advantages, e.g. it guarantees G2 continuity of the curves and surfaces and allows to use engineering parameters like lean, sweep, and stagger angle [11]. The main disadvantage is the inaccessibility of the source code of commercial CAD systems to compute the gradients. However, in recent years, great efforts were made to develop an in-house CAD system at VKI [12], hence being fully differentiable.

The main objective of this PhD research is to im-

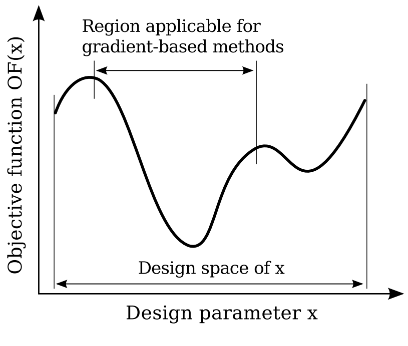

Figure 1: Feasible region of gradient-based methods for a single-objective function

plement gradient-based algorithms in the VKI optimization system based on CAD parameterization and to investigate the possible improvement as compared to evolutionary algorithms when applied to turbomachinery components. Computing the gradient of the objective function with respect to the design variables is an active field of research. Hence, many methods exist, e.g. the adjoint approach or automatic differentiation (AD). The feasibility of these methods will be assessed within the scope of this project and the most promising will be realized.

References

[1] S. Pierret, Designing Turbomachinery Blades by Means of the Function Approximation Concept Based on Artificial Neural Network, Genetic Algorithm and the Navier-Stokes Equations, Ph.D. thesis, von Karman Institute for Fluid Dynamics (1999).

[2] P. Rini, Z. Alsalihi, R. Van den Braembussche, Evaluation of a Design Method for Radial Impellers Based on Artificial Neural Network and Genetic Algorithm, in: Proceedings of the 5th ISAIF Conference, 2001, pp. 535–543.

[3] T. Verstraete, Z. Alsalihi, R. Van den Braembussche, Multidisciplinary Optimization of a Radial Compressor for Micro Gas Turbine Applications, in: ASME Turbo Expo 2007: Power for Land, Sea and Air, no. GT2007-27484, 2007.

[4] T. Verstraete, S. Amaral, R. A. Van den Braembussche, T. Arts, Design and Optimization of the Internal Cooling Channels of a HP Turbine Blade – Part II, Optimization, in: ASME Turbo Expo, Vol. GT2008-51080, 2008.

[5] T. Verstraete, Multidisciplinary Turbomachinery Component Optimization Considering Performance, Stress, and Internal Heat Transfer, Ph.D. thesis, Von Karman Institute for Fluid Dynamics - University of Gent (2008).

[6] R. Storn, K. Price, Differential Evolution - A Simple and Efficient Heuristic for Global Optimization over Continuous Spaces, Journal of Global Optimization 11 (1997) 341–359.

[7] G. Goldberg, Genetic Algorithms in Search, Optimization and Machine Learning, Addison-Wesley, 1989.

[8] A. Jameson, Gradient Based Optimization Methods, http://aero-comlab.stanford.edu/jameson/ (2005).

[9] G. Farin, Curves and Surfaces for Computer Aided Geometric Design, Academic Press. (1993).

[10] D. M. Fudge, D. W. Zingg, R. Haimes, A CAD-Free and a CAD-Based Geometry Control System for Aerodynamic Shape Optimization, American Institute of Aeronautics and Astronautics, 2005, 43.

[11] S. Shahpar, Challanges to Overcome for Routine Usage of Automatic Optimisation in Industry, in: VKI Lecture Series: Introduction to Optimization and Multidisciplinary Design in Aeronautics and Turbomachinery, 2011.

[12] T. Verstraete, CADO: a Computer Aided Design and Optimization Tool for Turbomachinery Applications, in: 2nd International Conference on Engineering Optimization, 2010.

Re-entry Platform for In-flight Demonstration and In-situ Measurement

Gilles Bailet

Aeronautics and Aerospace Department, von Karman Institute for Fluid Dynamics, Belgium,gilles.bailet@vki.ac.be

Supervisor: Jean Muylaert

Director, von Karman Institute for Fluid Dynamics, Belgium, jean.muylaert@vki.ac.be

University Supervisor: Christophe Laux

Professor, Laboratoire EM2C, Ecole Centrale Paris, France, christophe.laux@ecp.fr

---

Abstract

The von Karman Institute for fluid dynamics is aiming to develop and launch a re-entry vehicle by June 2015. Based on the CubeSat standard, with a highly constraining form factor (34x10x10cm), the vehicle will be developed in the frame of the PhD thesis and will represents a low-cost approach for the study of ablation and radiation in the harsh aerothermodynamics environment.

Keywords: re-entry, CubeSat, ablation, radiation, de-orbitation

---

1. Introduction

In the frame of the QB50 project led by the von Karman Institute for Fluid Dynamics (VKI) the paper exposes the preliminary results of the PhD thesis for the development of a re-entry CubeSat. More detailed data could be found in Bailet et al. (2011). The scientific objective of the QB50 project is to study the temporal and spatial variations of a number of key constituents and parameters in the lower thermosphere (50-320 km) with an international network of 50 double CubeSats (Fig. 1), miniaturized satellites weighing 2 kg in a 20x10x10 cm3 volume. The 50 CubeSats in a circular orbit will be separated by a few hundred kilometers and will carry identical sensors that will perform in-situ, long duration (~3 months) and multi- point measurements. QB50 will also study the re-entry process by measuring a number of key parameters during the re-entry process with the vehicle presented in this paper.

2. Re-entry CubeSat concept

A low cost nano-size re-entry spacecraft for in-situ measurements and in-orbit demonstration will permit huge opportunities for independent research institutions and industries to test materials or subsystems in real flight conditions as it is not fully duplicable on ground. A very attractive part of such a mission is to provide an affordable low cost platform to validate ground testing and numerical simulations that are designed to understand the scientific background of the atmospheric re-entry of spacecraft.

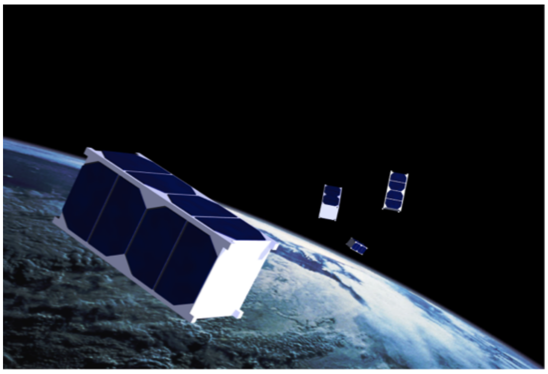

Figure 1: Artistic impression of few double-unit CubeSats of the QB50 constellation

The main difference between the proposed re-entry CubeSat platform and the 49 other QB50 CubeSats of the program is the need of an extra unit for the thermal protection system (TPS) to deal with the re-entry constraints. Such CubeSat standard, a 3-Unit (3U) CubeSat, imposes a platform that does not exceed 34x10x10 cm in shape and 3 kg in mass. The challenging part of the re-entry is located below 120 km of altitude. The first step of the study has focused on a target minimum altitude expected between 50 and 70 km. A low altitude target is a challenge, because for every other re-entry vehicle, the payload is designed first and then the external shape of the spacecraft is defined such that it covers the integrity of the payload and permits a defined mission scenario to be executed. A major mission-constraint is to enforce the destruction of the vehicle before it reaches the ground thus avoiding any problem of collision with ground assets.

3. Feasibility analysis and conceptual design

After a shape definition by means of multi-criteria optimization (Bailet et al., 2011), it clearly appeared that the thermal protection system is one of the most crucial subsystems. Two different parts can be distinguished, the heat shield (first third of the vehicle) and the side panels. The heat shield part has been shown to be realistically feasible, through plasmatron tests and thermal response simulations. The Cork P50 has been chosen as TPS for its high thermal resistance capability and its affordability and availability. It appears in the second part that the thermal limitations would come from the side panels. In fact, the side panels in the standard concept (1.5 mm thick of aluminum) are not suitable at all to reach the most interesting part of the trajectory and should be two times and half the original size for an increased thermal protection of the sub-systems. This option is not desirable at all and a composite panel with the adjunction of a Nextel insulation layer has been selected as appropriate for the mass/volume budget and the thermal viability of the vehicle during the re-entry.

The proposed spacecraft design permits to carry out the experiment in-flight as expected. To provide these data as exploitable, the necessity to recover them without loss and with a suitable data rate according to the experiment sampling is needed. It has been shown that the most feasible system is to transmit the data up to the LEO/MEO orbit and then transmit it down to the ground stations. This methodology permits to avoid the re-entry black out and so have scientific return during the most interesting part of the trajectory hardly accessible otherwise. The choice of the scientific experiments in accordance with the available mass/volume capacity will permit in future studies to size the communication system in more details as applying new constrains on the power budget.

An adequate power budget is needed to avoid any incertitude in the orbital dynamic calculations. Actually, the re-entry will be extremely demanding for the power supply system. In only 10 minutes all flight experiments and subsystems of the vehicle will work in full regime and the antenna will need lots of energy to transmit the signal with an efficient gain. The next table presents the power budget with margins required to perform the experiments and transmit the data. A security margin equal to two is applied to the payload and the amplifier power budget to ensure that the designed equipment will be within this power consumption. The Communication system uses the HISPICO patch antenna (5 W) and the Iridium transceiver (¡1 W) to be the interface between the data acquisition system and the satellite relay communication system. A synthesis of the power budget is presented hereafter in Table 1.

Table 1: Power budget of the nano-size re-entry vehicle

Subsystem	*Power needed including margins W*
Functional unit (Avionic)	2
Telecommunication system	2
Payload + amplifier	6
Total	10

The available batteries are able to bring 10 Whr for each with a maximum of 30 Whr with three stackable batteries. The lifetime of the vehicle between 120 km (re-entry interface) and 50 km (targeted altitude) is 600 seconds but the power system have to be conceive in the optic to provide energy as soon as the solar panels stop their jobs. In the worst case, the Vehicle will have to spend a half of orbit before the re-entry (20 000 km at an altitude superior at 120 km) in the shadow of the earth and so the batteries should sustain the power supplement of the vehicle during this time estimate at 45 minutes. In reality, at an altitude above 120 km and so during this time, all subsystems will not be used. Actually, only the subsystems of the functional unit will consume some power and then, the real power budget will be lower. The most critical case (55 minutes of flight on the batteries) will consume 10 W of power. Considering this case, the power supply should have a capacity of at least 9 Whr. A single battery is at the limit of the needed power.

By adding a security margin, two batteries will be sufficient to perform the minimal experiments required and furnish 12.2 W of supplementary power for more demanding experiments. In the aim to add supplementary payloads a third battery (maximum a stackable batteries) could be needed to reach the limit of 33.3 W in total.

4. Conclusion

The feasibility study has shown the multi-disciplinary complexity of a nano-scale re-entry CubeSat and the necessity for each sub-system to be considered in a mass/volume optimization point of view, for the purpose of respecting the 3-unit CubeSat standard (3kg total weight limit and 3000cm3). Although the methodologies and results presented in this study have their limitations in both physical modeling and accuracy, the first approach permits to draw up the mass budget of the mission (Table 2).

All the work performed has been compiled to give the mass and power budgets for the vehicle and so demonstrate the interesting and feasibility of the proposed platform with a payload mass of minimum 0.612 kg. The mass available, associated to the payload mass, and the extra margins permits to be confident on the expected scientific return. Future studies within the PhD will permit to select the payloads according to the scientific objectives (ablation and radiation) through aerothermodynamics and line of sight simulations. The work presented in this paper has identified and treated the different critical challenges of the re-entry mission including the system view on the vehicle.

From the feasibility analysis to the final conceptual design every aspect of the mission have been covered and analyzed. The result of the study is promising for both system view and potential scientific return. For illustration purpose, Fig. 2 shows the proposed configuration for the re-entry CubeSat with external and internal composition.

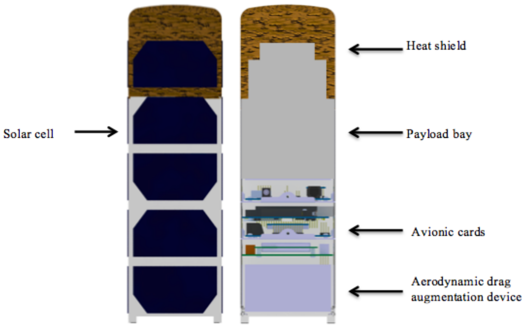

Figure 2: Re-entry CubeSat configuration external view (left) and internal view (right)

The nano-scale reentry vehicle remains an extraordinary opportunity for science and engineering in terms of in-situ experiment and in-flight demonstration capabilities and should be consider as the future low cost platform for in-flight experimentations.

Table 2: Mass budget of the nano-size re-entry vehicle

Subsystem	*Mass*	*Margins*	*Mass including margins*
	kg	*%*	*kg*
Heat shield	0.317	20	0.380
Functional unit (Avionic, Structure, Side panels, (Telecommunication system	1008 +0.036 (nose support) +0.173(Nextel blanket) +0.03 (transceiver)	0 30 10 10	1.248
Deorbiting system	0.400	30	520
Stability system	0.200	20	240
Total	1.937	-	2.388
		Payload	0.612-1.063

Acknowledgments

I would like to thank Mr. Jean-Marc Bouilly and his company EADS Astrium for their support and interest in this project.

References

[1] Bailet et al., Feasability Analysis and Preliminary Design of an Atmospheric Re-Entry Cubesat Demonstrator, 7th symposium on aerothermodynamics, ESA conference, Bruges, May 2011.

Multiscale Models and Computational Methods for Aerothermodynamics

Alessandro Munafò

Aeronautics and Aerospace Department, von Karman Institute for Fluid Dynamics, Belgium, munafo@vki.ac.be

Supervisor: Thierry Magin

Assistant Professor, Aeronautics and Aerospace Department, von Karman Institute for Fluid Dynamics, Belgium, magin@vki.ac.be

University Supervisor: Anne Bourdon

Chargée de recherche CNRS, Laboratoire EM2C CNRS UPR 288, École Central Paris, France, anne.bourdon@em2c.ecp.fr

---

Abstract

We propose to develop physical models and numerical methods for an accurate description of nonequilibrium physico-chemical phenomena in aerothermodynamics flows. Applications in aerospace range from space vehicle heat shield design to interpretation of experimental diagnostic measurements in high enthalpy facilities. In this work, we focus on the development of reduced collisional models for continuum nonequilibrium flows.

Keywords: Aerothermodynamics, Nonequilibrium, Collisional models, Coarse grain models, Finite volume method.

---

1. Introduction

Understanding nonequilibrium phenomena occurring in aerothermodynamic flows (such as the one around a spacecraft entering a planetary atmosphere) is of fundamental importance for many applications. Typical examples, taken from the aerospace domain, are the design of heat shields for space vehicles and interpretation of experiments carried out in high enthalpy wind tunnels. Nonequilibrium phenomena are also present in industrial processes making use of lasers, discharges and plasma torches. Progresses made in developing physical models and computational methods for aerospace applications, on which we focus here, could also be used in other areas (such as plasma enhanced combustion and electric propulsion) where the occurrence of nonequilibrium must be taken into account as well.

Before proceeding further, it is necessary to define nonequilibrium in aerospace applications. This concept can be introduced by recalling what occurs around a spacecraft entering a planetary atmosphere at hypersonic speeds. A strong bow shock is formed in front of the vehicle. The flow experiences a sudden compression. Pressure increases and, at the same time, most of the flow macroscopic kinetic energy is converted into thermal energy, leading to a steep temperature increase. The combined effects of pressure and temperature lead to higher values of collision frequencies between atoms and molecules and to more energetic collisions. These cause excitation of internal energy degrees of freedom and, if the collisions are energetic enough, breaking of chemical bonds can occur (molecular dissociation). If the entry speed is high enough ionization may also occur, and the gas becomes a partially ionized plasma where the presence of radiative transitions must be taken into account.

The description of these flows is extremely complicated because all collisional processes need a finite time to occur. If this time is very small compared to some macroscopic characteristic time scale (such as the time needed for a fluid particle to pass across a shock wave or through the boundary layer), the flow is in thermochemical equilibrium as it can immediately adapt to the varying conditions of pressure and temperature without any lag. If the inverse situation occurs, the flow is said to be frozen. The intermediate situation, where a finite lag exists, is that of nonequilibrium flows. In this case, a correct description of the flowfield can be achieved only if the finite rate nature of collisional processes is taken into account in the flow governing equations.

The starting point for the description of nonequilibrium flows are the Navier-Stokes equations, where nonequilibrium effects can be taken into account by means of multi-temperature or collisional models [1; 2]. Multi-temperature are based on Boltzmann distributions of the internal energy levels at distinct temperatures and are valid only in case of small departure from equilibrium [3]. However, they are widely used outside of their range of validity because of the lack of more accurate physical models, their easy implementation and their reasonable computational cost for 3D simulations.

State-to-state or collisional models [4; 5; 6; 7; 8; 9; 10] treat each energy level as a separate pseudo-species. This approach provides more flexibility and accuracy, since effects of non-Boltzmann distributions are accounted for. However, a very large number of processes have to be considered and, for each one, rate coefficient values have to be obtained. Also, the number of equations to be solved rapidly increases with the number of internal energy levels. Applications of collisional models to 2D problems have become feasible as shown in [11; 12; 13].

A further complication in the study of nonequilibrium flows comes from the presence of rarefied gas effects [14]. These occur in flow regions (such as bow shocks and wakes) where the macroscopic spatial scales becomes of the same order of the local mean free path (average distance traveled by atoms/molecules between successive collisions). The main consequence of that is the failure of the Navier-Stokes equations where the shear stress tensor and heat flux vector are given by the Newton and Fourier laws (as it can be shown by means of the Kinetic theory of gases [15; 16]), respectively. If an accurate description of rarefied gas effects is wished, one should move towards numerical solutions of the Boltzmann equation for dilute gases. This equation expresses a balance in the phase space (velocity and position) for the species velocity distribution function and has a wider range of applications than the Navier-Stokes equations[1]. Stochastic numerical solutions of the Boltzmann equation can be obtained by means of DSMC (Direct-Simulation-Monte-Carlo) methods [17], the main reasons being (when aiming at a deterministic numerical solution) the necessity of solving an equation in a high dimensional space (the phase space) and the complicated mathematical structure of the elastic and inelastic collision operators. On the other hand, deterministic methods based on discrete velocity models [18] or on a spectral representation of the collision operator [19; 20] are gaining more and more popularity and have started to be used also for multi-dimensional flows [21].

We conclude this introduction by mentioning that nonequilibrium and rarefied gas effects are also present in recombining flows such as those occurring in nozzles. The latter are adopted in high enthalpy wind tunnels where understanding nonequilibrium is of crucial importance for a correct interpretation of experimental measurements.

2. Motivation

For the present doctoral period, it was decided to concentrate our research activity on the following topics:

- Development of reduced (coarse grain) collisional models for CFD applications. This activity will be performed within an innovative context at the interface between computational quantum chemistry and computational fluid dynamics.
- Development of computational methods for the numerical solution of the Boltzmann equation with chemical reactions and internal energy excitation. Applications will focus on flows out of the range of applicability of the Navier-Stokes equations (such as shock waves).

In this paper, the first topic is studied.

3. QCT-based coarse grain models for dissociation and internal energy excitation

3.1. The NASA Ames database

The development of coarse grain models for continuum nonequilibrium flows is based on the N + N_2 system database recently developed by the Computational Quantum Chemistry group at NASA Ames Research Center [4; 22; 5]. The NASA Ames database comprises 9390 (v, J) rovibrational levels for the electronic ground-state of nitrogen, where index v stands for the vibrational quantum number, and index J, the rotational quantum number. These levels can also be denoted by means of a global index i, sorting them by

---

[1] The Navier-Stokes equations are a first order perturbation solution to the Boltzmann equation as obtained independently by S. Chapman and D. Enskog [15].

increasing value of energy. The relation between the i and (v, J) notations is expressed as:

$$i = i(v, J),\ v = 0, \ldots, v_{\max},\ J = 0, \ldots, J_{\max}(v) \quad (1)$$

Conversely, the relation between the (v, J) and i notations is given by the relations:

$$v = v(i), \quad J = J(i), \quad i \in \mathrm{I_{BP}} \quad (2)$$

where $\mathrm{I_{BP}}$ is the set of global indices for the nitrogen energy levels. Most of these levels are truly bound, *i.e.*, their energy is lower than the dissociation energy relative to the level $(v = 0, J = 0)$, equal to 9.75 eV for the electronic ground-state of nitrogen, while some of the energy levels are predissociated, *i.e.*, their energy is higher than the dissociation energy relative to the level $(v = 0, J = 0)$.

The bound energy levels are denoted by the set $\mathrm{I_B}$, and the predissociated energy levels, by the set $\mathrm{I_P}$. The set for all the levels is then given by $\mathrm{I_{BP}} = \mathrm{I_B} \cup \mathrm{I_P}$. The database for the N + N_2 system comprises more than 23 million reactions, for the following collisional processes:

- Dissociation of truly bound states and predissociated states:

$$\mathrm{N_2}(i) + \mathrm{N} \underset{k_i^{Db}}{\overset{k_i^{Df}}{\rightleftharpoons}} \mathrm{N} + \mathrm{N} + \mathrm{N}, \quad i \in \mathrm{I_{BP}} \quad (3)$$

- Predissociation of the predissociated states:

$$\mathrm{N_2}(i) \underset{k_i^{Pb}}{\overset{k_i^{Pf}}{\rightleftharpoons}} \mathrm{N} + \mathrm{N}, \quad i \in \mathrm{I_P} \quad (4)$$

- Excitation between all states:

$$\mathrm{N_2}(i) + \mathrm{N} \underset{k_{ji}^{E}}{\overset{k_{ij}^{E}}{\rightleftharpoons}} \mathrm{N_2}(j) + \mathrm{N}, \quad i, j \in \mathrm{I_{BP}}, \quad j > i \quad (5)$$

The direct reaction rate coefficients k_i^{Df}, k_i^{Pf}, and k_{ij}^{E}, $j > i$, are obtained based on the reaction cross-sections for nine values of the gas translational temperature between 7,500 and 50,000 K. The reverse reaction rate coefficients k_i^{Db}, k_i^{Pb}, and k_{ij}^{E}, $j < i$, are computed based on micro reversibility.

3.2. Strategies for coarse grain model development

Different strategies have been considered for the development of coarse grain models for the quantitative description of nonequilibrium rovibrational dissociation and excitation.

3.2.1. Vibrational Collisional (VC) model

The development of a new Vibrational Collisional (VC) model for the N + N_2 system is the first step of coarse grain model development. The procedure employed for obtaining vibrationally averaged rate coefficients has been presented in [23; 24]. In [24] applications of the VC model to normal shock wave and quasi 1D nozzle flows have been shown and the results obtained have been compared with those obtained by means of multi-temperature (MT) models. Recently, rate coefficients for N_2 + N_2 inelastic collisional processes among vibrational levels (VT and VV processes) have been added. Numerical values for them have been obtained by adapting the existing set of Billing data [25] to the vibrational energy levels of the NASA Ames database (the procedure is explained in [26]).

3.2.2. Boltzmann Rovibrational Collisional (BRVC) model

A new coarse grain approach has been proposed and investigated in parallel to the enrichment of the VC model recalled in the previous section. In this new coarse grain model, the energy levels of the N_2 molecule are firstly sorted according to their values and then lumped into energy bins for which bin-averaged rate coefficients are obtained by means of the following procedure.

The energy E_i for level i within bin k is defined based on the energy $\hat{E}_k$ for the first level in the bin and the relative energy contribution with respect to this energy level:

$$E_i = \hat{E}_k + \Delta\hat{E}_k(i), \quad i \in \mathrm{I}_k. \quad (6)$$

The energy level populations are assumed to follow a Boltzmann distribution at the translational temperature T within the bin $k \in \mathrm{K_{BP}}$:

$$\frac{n_i}{\hat{n}_k} = \frac{1}{\hat{Q}_k(T)} g_i \exp\left(\frac{-\Delta\hat{E}_k(i)}{\mathrm{k_B} T}\right), \quad i \in \mathrm{I}_k \quad (7)$$

where the partition function $\hat{Q}_k(T)$ and number density for the bin $\hat{n}_k$ are defined as:

$$\hat{Q}_k(T) = \sum_{i \in \mathrm{I}_k} g_i \exp\left(\frac{-\Delta\hat{E}_k(i)}{\mathrm{k_B} T}\right), \quad \hat{n}_k = \sum_{i \in \mathrm{I}_k} n_i \quad (8)$$

where the symbols $\mathrm{k_B}$ stands for Boltzmann's constant and $g_i = g_i^{\mathrm{NS}}(2J(i) + 1)$ (with g_i^{NS} representing the nuclear and spin contributions to the degeneracy of the ground electronic state of the N_2 molecule). As an alternative to Boltzmann Rovibrational Collisional

(BRVC) model presented in eq. (7), one could assume a uniform distribution within each bin leading to a Uniform Rovibrational Collisional (URVC) model that has successfully applied in [27]. This type of distribution does not allow to retrieve equilibrium when the number of bins is small.

The average rate coefficients for dissociation, predissociation and excitation for the BRVC model are:

$$\hat{k}_k^{Df}(T) = \frac{1}{\hat{Q}_k(T)} \sum_{i \in \mathrm{I}_k} g_i \exp\left(\frac{-\Delta \hat{E}_k(i)}{\mathrm{k_B} T}\right) k_i^{Df}(T), \tag{9}$$

$$\hat{k}_k^{Pf}(T) = \frac{1}{\hat{Q}_k(T)} \sum_{i \in \mathrm{I}_k} g_i \exp\left(\frac{-\Delta \hat{E}_k(i)}{\mathrm{k_B} T}\right) k_i^{Pf}(T), \tag{10}$$

$$\hat{k}_{kl}^{E}(T) = \frac{1}{\hat{Q}_k(T)} \sum_{i \in \mathrm{I}_k} g_i \exp\left(\frac{-\Delta \hat{E}_k(i)}{\mathrm{k_B} T}\right) \sum_{j \in \mathrm{I}_l} k_{ij}^{E}(T) \tag{11}$$

with $k \in \mathrm{K_B}$ in eq. (9), $k \in \mathrm{K_P}$ in eq. (10) and $k, l \in \mathrm{K_{BP}}$, $k < l$ in eq. (11). Reverse rate coefficients are computed by means of micro reversibility:

$$\frac{\hat{k}_k^{Db}}{\hat{k}_k^{Df}} = \frac{Q_{\mathrm{N_2}}^t(T)\, \hat{Q}_k(T) \exp(\frac{-(\hat{E}_k - 2E_\mathrm{N})}{\mathrm{k_B} T})}{[g_\mathrm{N} Q_\mathrm{N}^t(T)]^2}, \tag{12}$$

$$\frac{\hat{k}_k^{Pb}}{\hat{k}_k^{Pf}} = \frac{Q_{\mathrm{N_2}}^t(T) \hat{Q}_k(T) \exp(\frac{-(\hat{E}_k - 2E_\mathrm{N})}{\mathrm{k_B} T})}{[g_\mathrm{N} Q_\mathrm{N}^t(T)]^2}, \tag{13}$$

$$\frac{\hat{k}_{lk}^{E}}{\hat{k}_{kl}^{E}} = \frac{\hat{Q}_k(T) \exp(\frac{-(\hat{E}_k - \hat{E}_l)}{\mathrm{k_B} T})}{\hat{Q}_l(T)} \tag{14}$$

with $k \in \mathrm{K_B}$ in eq. (12), $k \in \mathrm{K_P}$ in eq. (13) and $k, l \in \mathrm{K_{BP}}$, $k < l$ in eq. (14). The quantity $g_\mathrm{N} = 12$ in eqs. (12) - (13) is the degeneracy of the N atom in the ground electronic state ($\mathrm{N}(^4\mathrm{S})$ nuclear and spin contributions) while $Q_\mathrm{N}^t(T)$ and $Q_{\mathrm{N_2}}^t(T)$ are the translational partition functions of the N atom and the $\mathrm{N_2}$ molecule, respectively:

$$Q_\mathrm{N}^t(T) = \left(\frac{2\pi \mathrm{k_B} m_\mathrm{N} T}{\mathrm{h_P^2}}\right)^{3/2}, Q_{\mathrm{N_2}}^t(T) = \left(\frac{2\pi \mathrm{k_B} m_{\mathrm{N_2}} T}{\mathrm{h_P^2}}\right)^{3/2} \tag{15}$$

where the symbol $\mathrm{h_P}$ stands for Planck's constant.

3.3. Governing equations

The coarse grain models described in the previous sections have been applied to 1D/2D inviscid flows, for which, the governing equations can be written in the usual conservation law form:

$$\frac{\partial r^\epsilon \mathbf{U}}{\partial t} + \frac{\partial r^\epsilon \mathbf{F}}{\partial x} + \frac{\partial r^\epsilon \mathbf{G}}{\partial r} = r^\epsilon \mathbf{S}^{\mathrm{col}} + \epsilon\, \mathbf{S}^{\mathrm{axi}} \tag{16}$$

where $\epsilon = 0$, 1 for plane and axisymmetric flows, respectively. In eq. (16), **U** is the conservative variable vector, **F** and **G** are, respectively, the inviscid flux vectors along the x and r directions, $\mathbf{S}^{\mathrm{col}}$ is the source term vector due to collisional processes and $\mathbf{S}^{\mathrm{axi}}$ is an additional geometrical source term due to axial symmetry. The mathematical expressions for the quantities in eq. (16) change according to the physical model being used. If the BRVC model is considered, the following expressions are obtained:

$$\mathbf{U} = \begin{bmatrix} \rho_\mathrm{N} & \tilde{\rho}_k & \rho u & \rho v & \rho E \end{bmatrix}^\mathrm{T}, \tag{17}$$

$$\mathbf{F} = \begin{bmatrix} \rho_\mathrm{N} u & \tilde{\rho}_k u & p + \rho u^2 & \rho u v & \rho u H \end{bmatrix}^\mathrm{T}, \tag{18}$$

$$\mathbf{G} = \begin{bmatrix} \rho_\mathrm{N} v & \tilde{\rho}_k v & \rho u v & p + \rho v^2 & \rho v H \end{bmatrix}^\mathrm{T}, \tag{19}$$

$$\mathbf{S}^{\mathrm{col}} = \begin{bmatrix} \omega_\mathrm{N} & \tilde{\omega}_k & 0 & 0 & 0 \end{bmatrix}^\mathrm{T}, \quad k \in \mathrm{K_{BP}}, \tag{20}$$

$$\mathbf{S}^{\mathrm{axi}} = \begin{bmatrix} 0 & 0 & 0 & p & 0 \end{bmatrix}^\mathrm{T} \tag{21}$$

In eq. (20), the components ω_N and $\tilde{\omega}_k$ of the source term vector $\mathbf{S}^{\mathrm{col}}$ represent the production rates for the N atom and the $\mathrm{N_2}$ bins due to collisional excitation and dissociation and predissociation:

$$\begin{aligned} \omega_\mathrm{N} &= 2M_\mathrm{N}[X_\mathrm{N}] \sum_{k \in \mathrm{K_B}} \left[\hat{k}_k^{Df}(T)\, X_k - \hat{k}_k^{Db}(T)\, [X_\mathrm{N}]^2\right] \\ &+ 2M_\mathrm{N} \sum_{k \in \mathrm{K_P}} \left[\hat{k}_k^{Pf}(T)\, X_k - \hat{k}_k^{Pb}(T)\, [X_\mathrm{N}]^2\right], \end{aligned} \tag{22}$$

$$\begin{aligned} \tilde{\omega}_k &= -M_{\mathrm{N_2}}[X_\mathrm{N}] \left[\hat{k}_k^{Df}(T)\, X_k - \hat{k}_k^{Db}(T)\, [X_\mathrm{N}]^2\right] \\ &- M_{\mathrm{N_2}} \left[\hat{k}_k^{Pf}(T)\, X_k - \hat{k}_k^{Pb}(T)\, [X_\mathrm{N}]^2\right] \\ &- M_{\mathrm{N_2}}[X_\mathrm{N}] \left\{ \sum_{l \in \mathrm{K_{BP}}}^{k>l} \left[\hat{k}_{kl}^{E}(T)\, X_k - \hat{k}_{lk}^{E}(T)\, X_l\right] \right. \\ &+ \left. \sum_{l \in \mathrm{K_{BP}}}^{k<l} \left[\hat{k}_{lk}^{E}(T)\, X_l - \hat{k}_{kl}^{E}(T)\, X_k\right] \right\}, \; k \in \mathrm{K_{BP}} \end{aligned} \tag{23}$$

For the VC model, the expressions for the vectors in eq. (16) and the production rates ω_N and $\tilde{\omega}_v$ for the N atom and $\mathrm{N_2}$ vibrational levels are similar as given in [24; 26]. The only difference is that molecular energy exchange (VT and VV) and molecular impact dissociation processes are considered. Hence, their presence must be taken into account in the expression for ω_N and $\tilde{\omega}_v$ (see [26] for more details).

Eq. (16) can also be used for the investigation of nonequilibrium effects in quasi 1D nozzle flows. The only modification (after dropping all quantities relative to the r direction and setting $\epsilon = 0$) is the inclusion of a geometrical source term $\mathbf{S}^{\mathrm{area}}$ (due to cross sectional area variation) in the right-hand-side of eq.

(16):

$$\mathbf{S}^{\text{area}} = -\frac{\partial \ln A}{\partial x}\left[\begin{array}{cccc} \rho_{\mathrm{N}} u & \tilde{\rho}_k u & \rho u^2 & \rho u H \end{array}\right]^{\mathrm{T}}, k \in \mathrm{K}_{\mathrm{BP}} \tag{24}$$

3.4. Numerical method

Eq. (16) is discretized in space by means of the Finite volume method [28]. Roe's approximate Riemann solver [29] is used for inviscid fluxes. Roe's averaged state is computed by using the linearization proposed in [30]. Higher order spatial accuracy is reached through a polynomial reconstruction performed on primitive [31] or characteristic variables [12; 13]. The van Albada and minmod limiters [28] are used in order to preserve solution monotonicity close to discontinuities.

Time integration of the space discretized system of equations is performed by means of a fully implicit method for 1D/quasi 1D flows [31], while an operator splitting approach [12; 13; 26] is used for 2D flows.

3.5. Applications

3.5.1. VC model

The VC model of Sec. 3.2.1 has been used for investigating the 2D axisymmetric nonequilibrium flow within the nozzle of the EAST (Electric Arc Shock Tube) facility at NASA Ames Research Center (see Fig. 1).

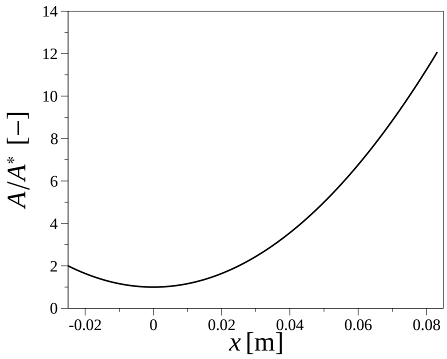

Figure 1: Normalized area distribution of the EAST facility nozzle (throat at $x = 0$ m).

Reservoir values of total pressure and temperature are 100 atm and 5,600 K, respectively. They correspond to operating conditions of the facility for which Raman spectroscopy measurements of the relative populations of vibrational levels are available [32]. Computations have been performed under the assumption of local thermodynamic equilibrium at the nozzle inlet. In order to get more physical insight from the simulation, a vibrational temperature T^{v} has been extracted from the vibrational energy level populations by solving the following algebraic non-linear equation:

$$\frac{\sum_{v=0}^{v_{\max}} \tilde{n}_v \tilde{E}_v}{n_{\mathrm{N}_2}} = \frac{\sum_{v=0}^{v_{\max}} \tilde{E}_v \exp\left(-\frac{\tilde{E}_v}{k_{\mathrm{B}} T^{\mathrm{v}}}\right)}{\sum_{v=0}^{v_{\max}} \exp\left(-\frac{\tilde{E}_v}{k_{\mathrm{B}} T^{\mathrm{v}}}\right)} \tag{25}$$

at each mesh cell. Fig. 2 shows the temperatures together with the distribution of the same quantities along the nozzle axis.

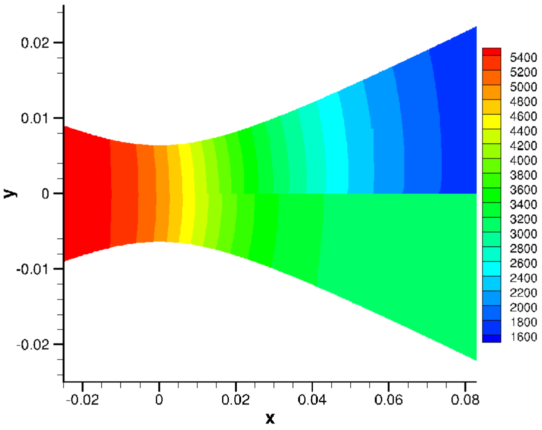

(a) Temperature distribution (upper part T - lower part T^{v}).

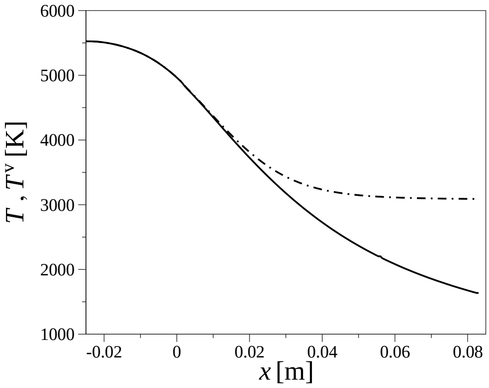

(b) Temperatures along the nozzle axis (—— T, −·− T^{v}).

Figure 2: Translational and vibrational temperatures.

The flow remains in thermal equilibrium for the entire converging part of the nozzle. Once it crosses the throat ($x = 0$ m), the expansion becomes significant and nonequilibrium effects start to appear. This is caused by a reduction of the flow macroscopic timescales due to the velocity increase. The translational and vibrational temperatures start deviating from each other, with the latter becoming frozen around $x \simeq 0.04\,\mathrm{m}$. Downstream of this location, the flow further expands as if the inelastic collisional processes taken into account were not occurring.

The usage of a VC model allows for a detailed investigation of the energy level dynamics. Moreover, since no hypothesis is done on the population distribution, it is possible to check the approximation introduced by conventional multi-temperature models (where a Boltzmann distribution at its own temperature is supposed to exist for each species internal degree of freedom). Fig. 3 shows the evolution of the distribution along the nozzle axis.

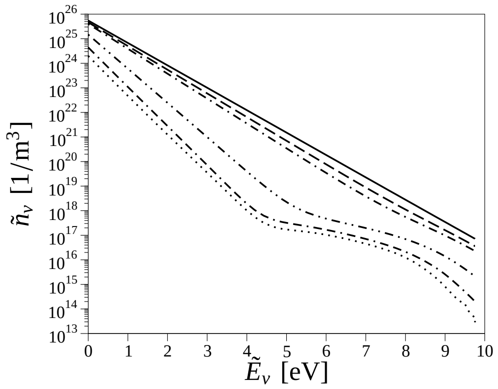

Figure 3: Population evolution along the nozzle axis (── $x = -0.025\,\mathrm{m}$, − − − $x = -0.006\,\mathrm{m}$, − · − $x = 0\,\mathrm{m}$, − · · · − $x = 0.024\,\mathrm{m}$, − − − · − − − $x = 0.054\,\mathrm{m}$, · · · · $x = 0.083\,\mathrm{m}$).

At the inlet, where equilibrium is imposed, all levels lie along a straight line. When the flow begins to expand in the converging part of the nozzle, the shape of the distribution remains the same. Only the slope changes as an effect of the cooling. A small overpopulation starts to appear (for high-lying levels) at the throat and this becomes more and more pronounced when the flow becomes supersonic. At the outlet, the ground state and low-lying levels are aligned along a straight line (whose slope is proportional to the inverse of the vibrational temperature T^{v} previously shown) while high-lying levels experience overpopulation. The latter is an indication that lumping all the levels within a Boltzmann distribution (as done within the context of multi-temperature models) is not possible (for the reservoir conditions adopted here).

The computed population distributions (for the first 9 vibrational levels) have been compared against experimental data acquired by means of Raman spectroscopy [32] at the locations $x = -0.006$, $x = 0.024$ and $x = 0.054\,\mathrm{m}$ (see Fig. 4). The agreement is excellent for the first location, where the flow is close to equilibrium. For the second and third locations, the agreement is good for the ground state and the first four excited levels, while discrepancies start to appear

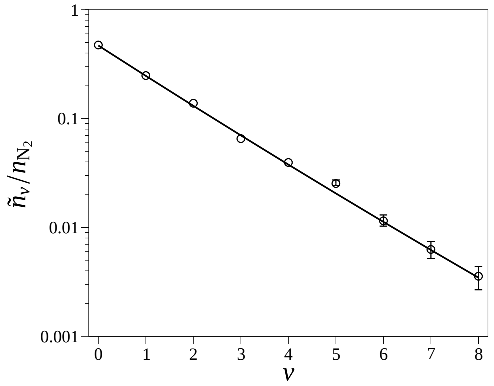

(a) Position 1 ($x = -0.006\,\mathrm{m}$).

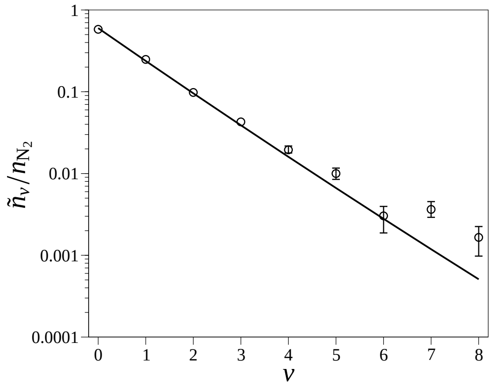

(b) Position 2 ($x = 0.024\,\mathrm{m}$).

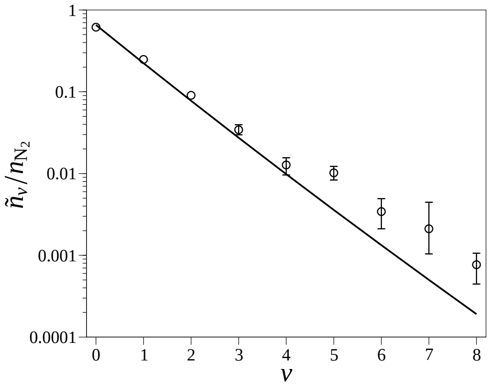

(c) Position 3 ($x = 0.054\,\mathrm{m}$).

Figure 4: Comparison between computed and experimental normalized vibrational energy level population distributions (── Comp., ○ Exp.).

for the higher states. In this zone (where measurement errors are more significant), the computational model adopted predicts a Boltzmann distribution at the temperature T^{v}, while an overpopulation appears in experimental data. The latter could be due to the presence of some nonequilibrium at the nozzle inlet (not accounted for in the computations). Moreover, the actual flow in the facility is characterized by the presence of viscous effects and unsteadiness. None of these factors has been taken into account within the computational model adopted. In view of that, the comparison between computational and experimental data can be considered satisfactory.

3.5.2. BRVC model

The BRVC model (see Sec. 3.2.2) has been applied to study nonequilibrium effects in simple flows, such as the flow downstream a normal shock wave and the quasi 1D flow within a nozzle. Computations have been performed by using different numbers of energy bins for the N_2 molecule for an estimation of how many bins are needed in order to get a flowfield description being both accurate (when compared with the Rovibrational Collisional (RVC) model) and computationally cheap. In this case, only $N + N_2$ collisions have been taken into account and computational results have been compared against the VC model of Sec. 3.2.1 and the classical Park MT model [33]. In all simulations, an internal temperature T^{int} has been extracted by solving the following non linear algebraic equation:

$$\frac{\sum_{k\in \mathrm{K}_{\mathrm{BP}}} \hat{n}_k \hat{E}_k}{n_{\mathrm{N}_2}} = \frac{\sum_{k\in \mathrm{K}_{\mathrm{BP}}} \hat{E}_k \, \hat{Q}_k(T) \, \exp(-\frac{\hat{E}_k}{\mathrm{k_B} T^{\mathrm{int}}})}{\sum_{k\in \mathrm{K}_{\mathrm{BP}}} \hat{Q}_k(T) \, \exp(-\frac{\hat{E}_k}{\mathrm{k_B} T^{\mathrm{int}}})} \qquad (26)$$

at each mesh cell in order to characterize macroscopically thermal nonequilibrium.

For the computation of nonequilibrium quasi 1D nozzle flow, the EAST nozzle shape (see Fig. 1) has been considered. In this case, the length of its diverging portion has been increased up to 0.15 m in order to enhance the gas expansion. The reservoir values of pressure and temperature have been artificially set to 1 atm and 10,000 K, respectively, in order to ensure $N + N_2$ collisions to be the dominant mechanism within the flow. Fig. 5 shows the temperature (translational, internal and vibrational) and N_2 molar fraction variations along the nozzle axis (75 bins for the BRVC model). The translation temperature for the VC and MT is not shown but it is very close to the one obtained by means of the BRVC model.

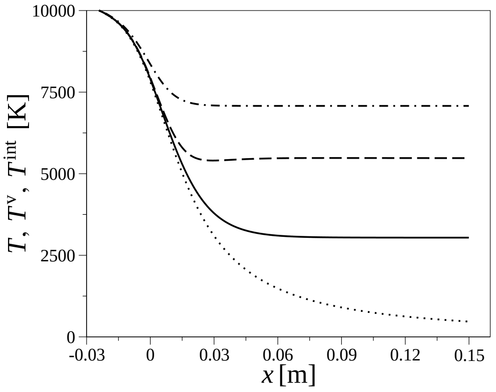

(a) Temperatures (· · · · T BRVC, —— T^{int} BRVC, − − − T^{v} VC, − · − T^{v} MT.

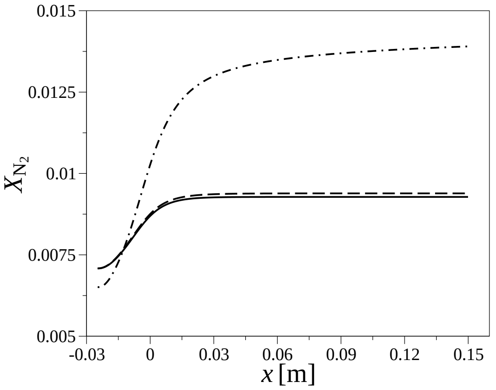

(b) N_2 molar fraction (—— BRVC, − − − VC, − · − MT).

Figure 5: Comparison between results provided by the BRVC (75 bins), VC and MT models (expanding flow).

The behavior of the vibrational and internal temperatures is very different for all models and this is due to the way the coupling between chemistry and internal energy (vibrational energy for VC and MT models) is realized in each model under consideration. In MT models, it is usually assumed that the average vibrational energy lost/gained during dissociation/recombination is equal to bulk vibrational energy of the flow (non preferential dissociation model [3]). However, the former does not take into account that molecules tend to preferentially recombine in highlying states, as done by contrast by both VC and BRVC models. This inaccurate description has consequences not only on the temperatures, but also on the degree of recombination due to the coupling between chemistry and internal energy. This can be appreciated in Fig. 5, where it is shown that MT model provides the highest value. No appreciable differences (for the N_2 molar fraction) arise between the VC and

BRVC models. This fact could be explained by recalling that, for the conditions here adopted, rotational nonequilibrium effects (automatically taken into account in the BRVC) are negligible.

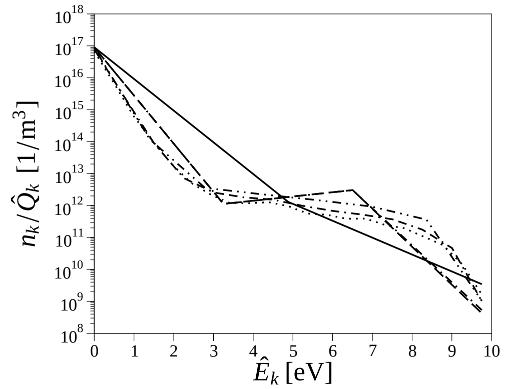

(a) —— 3 bins, – – – 4 bins, – · – 5 bins, – · · – 10 bins, – – · – – 20 bins, · · · · 30 bins.

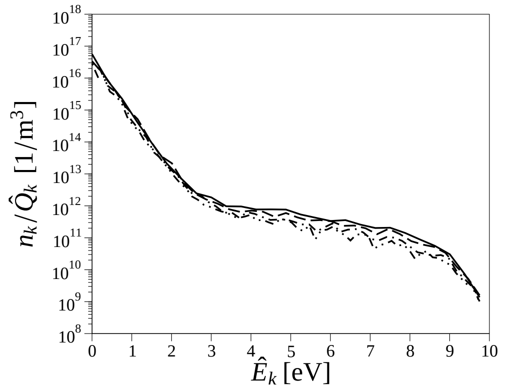

(b) —— 40 bins, – – – 50 bins, – · – 75 bins, – · · – 100 bins.

Figure 6: Bin number convergence study on the normalized population distribution at the nozzle outlet.

The same testcase has been run by using different number of bins (3, 4, 5, 10, 20, 30, 40, 50, 75 and 100) in order to understand its influence on the accuracy of the energy level dynamics. Fig. 6 shows the population distributions at the nozzle outlet with different number of bins. As already observed before for the VC model, the distributions experience in all cases departure from a Boltzmann distribution. In particular, heavy distortions due to overpopulation can be observed in the tail region. The former feature is common to all cases analyzed here. However, the accuracy of the description of the level dynamics is too poor when using 3-4 bins. The main features of the converged population distribution (straight line and plateau regions) are already retrieved with 10 bins. If the bin number is then increased, it is possible to obtain more accurate descriptions though the distributions look qualitatively the same. A good compromise between accuracy and computational efficiency (as suggested by the present testcase) would be to use 20-30 bins.

For the investigation of the nonequilibrium flow behind a normal shock wave, free-stream values of pressure, velocity and temperature have been set to 13.3 Pa, 10 km/s and 300 K, respectively. The free-stream has been seeded with 0.28 % of N since only $N + N_2$ collisions are taken into account.

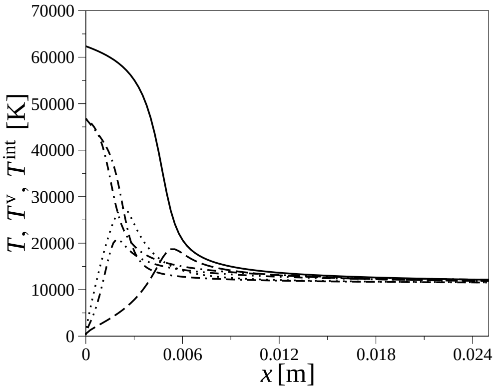

(a) Temperatures (—— T BRVC, – – – T^{int} BRVC, – · – T VC, – · · – T^{v} VC, – – · – – T MT, · · · · T^{v} MT).

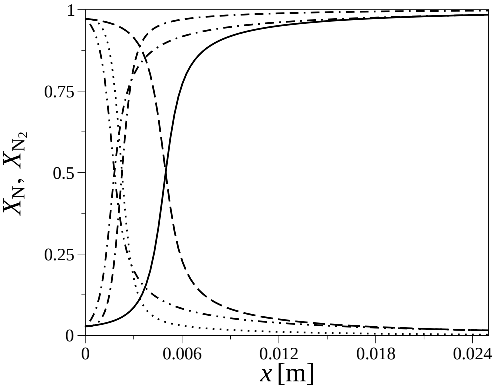

(b) Molar fractions (—— N BRVC, – – – N_2 BRVC, – · – N VC, – · · – N_2 VC, – – · – – N MT, · · · · N_2 MT).

Figure 7: Comparison between results provided by the BRVC (100 bins), VC and MT models (compressing flow).

A convergence study on the number of bins (see [31]), has allowed to retrieve the same conclusions as those found for the expansion case (i.e. only 20-30 bins are needed for a reasonably accurate description of the level dynamics).

Computational results have been compared with those provided by the VC and MT models. Fig. 7 shows temperatures (translational, vibrational and internal) and N and N_2 molar fractions (100 bins for the BRVC model). The MT model leads to the fastest dissociation, while the BRVC is the slowest among the three models.

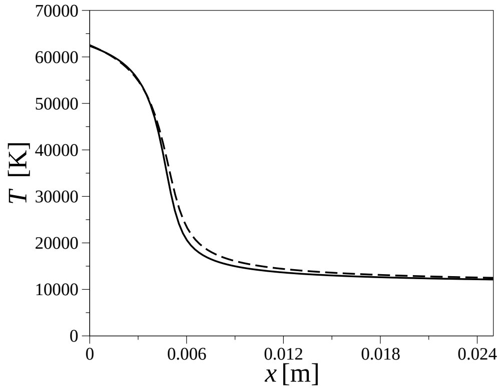

(a) Temperature (—— BRVC, – – – RVC).

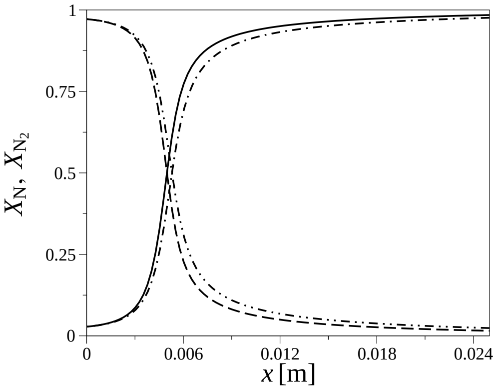

(b) Molar fractions (—— N BRVC, – – – N_2 BRVC, – · – N RVC, – · · – N_2 RVC).

Figure 8: Comparison between results provided by the BRVC (100 bins) and RVC models (compressing flow).

Differences between the BRVC and VC models arise now also for the chemical composition (while they are negligible in the expanding case). The faster dissociation obtained by means of the VC model is due to the hypothesis of rotational equilibrium. Indeed, in a previous work [34] it is has been shown that, for the free-stream conditions adopted here, the former hypothesis does not hold. On the other hand, the BRVC model does not make any assumption on the population of rotational levels. Hence, it automatically takes into account for rotational nonequilibrium effects. A confirmation is provided by the consistency observed for the translational temperature and N and N_2 molar fractions between the RVC and BRVC model solutions (see Fig. 8).

4. Conclusions

Coarse grain collisional models based on the NASA Ames Database for the N + N_2 system have been applied for the investigation of nonequilibrium effects in compressing and expanding flows. A VC model previously developed from the same database has been enriched in order to take into account for $N_2 + N_2$ inelastic collisions and been applied for computing the flow within the nozzle of the EAST facility. Computed vibrational energy level populations have been compared with experimental data. A good agreement has been observed. A new coarse grain BRVC model has been formulated and applied to 1D/quasi 1D flows. The results obtained have shown its higher flexibility (over the VC model) due to the possibility of taking into account for rotational nonequilibrium effects across shock waves.

Future work will focus on the multi-temperature reformulation of the BRVC and RVC models.

Acknowledgments

The research activity of the author is supported by the European Research Council Starting Grant #259354. The author would like to thank R. L. Jaffe and D. W. Schwenke, at NASA Ames Research Center, for providing the QCT rate coefficients used for obtaining the coarse grain models presented here, J. L. Cambier, at Edwards Air Force Base, and M. G. Kapper, at von Karman Institute, for their support and for providing the code used for the multi-dimensional simulations, and M. Panesi, at the University of Texas at Austin, for the help and the useful discussions while developing the Boltzmann Rovibrational Collisional model.

References

[1] C. Park, Nonequilibrium hypersonic aerothermodynamics, Wiley, New York, 1990.

[2] M. Capitelli, C. M. Ferreira, B. F. Gordiets, A. I. Osipov, Plasma kinetics in atmospheric gases, Springer, 2000.

[3] C. Park, The limits of two temperature model, AIAA Paper 2010–911, 48th AIAA Aerospace Sciences Meeting including the new Horizons Forum and Aerospace Exposition, Orlando, Florida (2010).

[4] R. L. Jaffe, D. W. Schwenke, G. Chaban, W. Huo, Vibrational and rotational excitation and relaxation of nitrogen from accurate theoretical calculations, AIAA Paper 2008-1208, 46th AIAA Aerospace Sciences Meeting and Exhibit, Reno, Nevada (2008).

[5] D. W. Schwenke, Dissociation cross-sections and rates for nitrogen, in: Non-equilibrium Gas Dynamics: from Physical Models to Hypersonic Flights, Lecture Series, von Karman Institute for Fluid Dynamics, 2008.

[6] F. Esposito, M. Capitelli, Quasi-classical molecular dynamic calculations of vibrationally and rotationally state selected dissociation cross sections: $N + N_2 \rightarrow 3N$, Chemical Physics Letters 302 (1) (1999) 49–54.

[7] J. G. Kim, O. J. Kwon, C. Park, Master equation study and nonequilibrium chemical reactions for $H + H_2$ and $He + H_2$, Journal of Thermophysics and Heat Transfer 23 (3) (2009) 443–453.

[8] A. Bultel, B. G. Chéron, A. Bourdon, O. Motapon, I. F. Schneider, Collisional-radiative model in air for earth re-entry problems, Physics of Plasmas 13 (4) (2006) 11.

[9] M. Panesi, T. E. Magin, A. Bourdon, A. Bultel, O. Chazot, Analysis of the fire II flight experiment by means of a collisional radiative model, Journal of Thermophysics and Heat Transfer 23 (2) (2009) 236–248.

[10] J. L. Cambier, S. Moreau, Simulation of a molecular plasma in collisional-radiative nonequilibrium, AIAA Paper 1993-3196, 24th AIAA Plasmadynamics & Lasers Conference, Orlando, Florida (1993).

[11] E. Josyula, W. F. Bailey, Vibration-dissociation coupling using master equations in nonequilibrium hypersonic blunt-body flow, Journal of Thermophysics and Heat Transfer 15 (2) (2001) 157–167.

[12] M. G. Kapper, J. Cambier, Ionizing shocks in argon. part I: Collisional-radiative model and steady-state structure, Journal of Applied Physics 109 (11) (2011) 113308.

[13] M. G. Kapper, J. Cambier, Ionizing shocks in argon. part II: Transient and multi-dimensional effects, Journal of Applied Physics 109 (11) (2011) 113309.

[14] C. Cercignani, Rarefied gasdynamics, Cambridge University Press, Cambridge, UK, 2000.

[15] S. Chapman, T. G. Cowling, The mathematical theory of non uniform gases, Cambridge University Press, Cambridge, UK, 1970.

[16] W. J. Vincenti, C. H. Kruger, Introduction to physical gasdynamics, Wiley, New York, 1965.

[17] G. A. Bird, Molecular Gas Dynamics and the Direct Simulation of Gas Flows, Clarendon press, Oxford, UK, 1994.

[18] F. G. Tcheremissine, Solution of the boltzmann equation for high-speed flows, Computational mathematics and mathematical physics 46 (2) (2006) 329–343.

[19] I. M. Gamba, S. H. Tharkabhushanam, Shock and boundary structure formation by spectral-lagrangian methods for the inhomogenesous boltzmann transport equation, Journal of Computational Mathematics 28 (4) (2010) 430–460.

[20] F. Filbet, G. Russo, High order numerical methods for the space non-homogeneous boltzmann equation, Journal of Computational Physics 186 (2) (2003) 457–480.

[21] L. Mieussens, Discrete-velocity models and numerical schemes for the boltzmann-bgk equation in plane and axisymmetric geometrieis, Journal of Computational physics 162 (2) (2000) 429–466.

[22] R. L. Jaffe, D. W. Schwenke, G. Chaban, Theoretical analysis of N_2 collisional dissociation and rotation-vibration energy transfer, AIAA Paper 2009–1569, 47th AIAA Aerospace Sciences Meeting and Exhibit, Orlando, Florida (2009).

[23] T. E. Magin, M. Panesi, A. Bourdon, R. L. Jaffe, D. W. Schwenke, Internal energy excitation and dissociation of molecular nitrogen in a compressing flow, AIAA Paper 2009–3837, 41st AIAA Thermophysics Conference, San Antonio, Texas (2009).

[24] A. Munafò, M. Panesi, R. L. Jaffe, A. Lani, T. E. Magin, Vibrational state to state kinetics in expanding and compressing nitrogen flows, AIAA Paper 2010–4335, 10th AIAA/ASME Joint Thermophysics and Heat Transfer Conference, Chicago, Illinois (2010).

[25] G. D. Billing, E. R. Fisher, VV and VT rate coefficients in N_2 by a quantum-classical mode, Chemical Physics 43 (3) (1979) 395–401.

[26] A. Munafò, M. G. Kapper, J. L. Cambier, T. E. Magin, Investigation of nonequolibrium effects in axisymmetric nozzle and blunt body nitrogen flows by means of a reduced rovibrational collisional model, AIAA Paper 2012-0647, 50th AIAA Aerospace Science Meeting, Nashville, Tennessee (2012).

[27] T. E. Magin, M. Panesi, A. Bourdon, R. L. Jaffe., D. W. Schwenke, Coarse-grain model for internal energy excitation and dissociation of molecular nitrogen, Chemical PhysicsIn press.

[28] C. Hirsch, Numerical computation of internal and external flows, John Wiley and Sons, Chichester, UK, 1988.

[29] P. L. Roe, Approximate riemann solvers, parameter vectors and difference schemes, Journal of Computational Physics 43 (2) (1981) 357–372.

[30] R. K. Prabhu, An implementation of a chemical and thermal nonequilibrium flow solver on unstructured meshes and application to blunt bodies:s, NASA CR 194867 (1994).

[31] A. Munafò, M. Panesi, R. L. Jaffe, A. Bourdon, T. E. Magin, Mechanism reduction for rovibrational energy excitation and dissociation of molecular nitrogen in hypersonic flows, AIAA Paper 2011-3623, 11th AIAA/ASME Joint Thermophysics and Heat Transfer Conference, Honolulu, Hawaii (2011).

[32] S. P. Sharma, M. R. Ruffin, W. D. Gillespie, S. A. Meyer, Vibrational relaxation measurements in an expanding flow using spontaneous raman scattering, Journal of Thermophysics and Heat Transfer 7 (4) (1993) 697–703.

[33] C. Park, Review of chemical-kinetic problems of future nasa mission, i: Earth entries, Journal of Thermophysics and Heat Transfer 7 (3) (1993) 385–398.

[34] T. E. Magin, M. Panesi, A. Bourdon, R. L. Jaffe, D. W. Schwenke, Rovibrational internal energy excitation and dissociation of molecular nitrogen in hypersonic flows, AIAA Paper 2010–4336, 10th AIAA/ASME Joint Thermophysics and Heat Transfer Conference, Chicago, Illinois (2010).

Arbitrary Lagrangian-Eulerian Simulation of a moving Piston in Hypersonic Ground Test Facility

Khalil Bensassi

von Karman Institute for fluid Dynamics, Aeronautics and Aerospace Department, bensassi@vki.ac.be

Supervisor: Patrick Rambaud

Associate Professor, Aeronautics and Aerospace Department, von Karman Institute for Fluid Dynamics, Belgium, rambaud@vki.ac.be

Co-Supervisor: Herman Deconinck

Associate Professor, Aeronautics and Aerospace Department, von Karman Institute for Fluid Dynamics, Belgium, deconinck@vki.ac.be

Abstract

Numerical simulation of a moving piston by means of an arbitrary Lagrangian-Eulerian solver in a two-dimensional field is performed in order to investigate the flow physics inside VKI-Longshot hypersonic ground test facility. The dynamics of the piston is coupled with the fluid using a moving boundaries. Rigid mesh strategy was used for the mesh adaptation algorithm. The numerical methods and time integration scheme are described. The space-time diagram shows the speed and the trajectory of the piston as well as the flow pattern involving expansion fan and shock waves in the driver-driven part of the facility.

Keywords: Unsteady Hypersonic flow, arbitrary Lagrangian-Eulerian, hypersonic facility

1. Introduction

The Development of future space vehicle requires hypersonic ground testing and extensive computations before the real flight. The success of a mission will depend on the reliability of the experimental data, the accuracy of the CFD and the methodology used to extrapolate these data from ground test to flight. The increase of the computational resources, the recent development in physical modeling and numerical schemes have gave the computational part much more important role in the space missions. The validation of the computational codes with experimental data is more than necessary , therefore accurate ground test conditions are needed. The free stream conditions in most hypersonic wind tunnel are very difficult to assess and remain on of the most challenging task even in the recent hypersonic facility. The uncertainties on their values could reach 20%. It's mostly due to a lack of experimental data on some part of the facility like inside the nozzle or the driven/driven tube and also to some technical difficulties to measure some main flow parameters. The full simulation of the facility is a complex task because it involves multi-physics and up to date it remains a challenging task.

In the current work we focus on the VKI-Longshot wind tunnel which is is a short duration facility (Fig.1) that can be operated with either nitrogen or carbon dioxide and it is designed to reach very high Reynolds number hypersonic flows. It is essentially based on two tubes (driver and driven tubes) and a nozzle which discharges into a test chamber. It has a Mach 14 contoured nozzle [5] of 0.42 m exit diameter and a 6° conical nozzle of 0.60 m exit diameter which can be used throughout a Mach number range from 15 to 20.

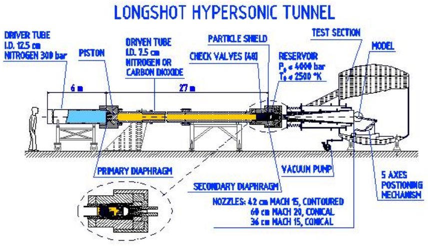

Figure 1: Schematic online of the Longshot tunnel

The driver gas, usually nitrogen operates at a pressure between 300 and 1000 bars at room temperature, in a 12.5 cm diameter tube which is 6 m long. The initial pressure of the gas in the driven tube can vary from 1 to 15 bars and its temperature is the room temperature. The nozzle and chamber are evacuated down to about 1 Pa pressure. In order to release the piston, a valve opens and applies the initial pressure on an extra surface of the piston front which is enough to break the diaphragm. The piston, then moves in the driven tube and it is accelerated at speeds of the order of 600 m/s, compressing the gas through a shock wave standing ahead at the end of the piston course there is a 48 check valves that allow the gas to be trapped. the gas expand through the nozzle into a $16m^3$vacuum vessel. A series of reflection occur between the piston head and the driver tube end which finally stops the piston. A decompression wave appears at the rear of the piston due to the rarefaction of the gas. It travels from the driver tube to eventually reach the rear part of the piston and causes the piston rebound. When the piston moves back in the driven tube, the pressure ahead of the piston decreases and finally becomes lower than in the reservoir. Therefore, in order to trap the gas in the $320cm^3$ reservoir, a plate check valves is installed at the end of the piston course which causes the closure of the 48 check valves. Once the gas is trapped, the second diaphragm breaks and this allows the gas to expand through the nozzle into a $16m^3$ vacuum vessel. In order to prevent the biggest particles caused by the rupture of the diaphragm from obstructing the nozzle or destroying the model, a particle shield has been placed just upstream the diaphragm.

2. Governing Equations

The conservative Navier-Stokes or Euler equations are usually solved on a computational domain $\Omega(t)$ that is constant in time, i.e $\Omega(t) = \Omega(t_0)$ for both steady and unsteady cases. the formulation used for those cases is called Eulerian form of the equations. In some cases, it is practical to use the velocity of the flow as a speed of the computational domain $\Omega(t)$, we then refer to a Lagrangian formulation. The formulation used for intermediate cases, in which the computational domain evolves and deforms independently, is called an Arbitrary Eulerian-Lagrangian formulation (ALE). The space discretization and time integration methods used in Eulerian framework were extended for Arbitrary Eulerian-Lagrangian formulation [2].

In the current work, Finite Volume method is used as a space discretization technique. The two-dimensional conservative Euler equations for a time dependent computational domain $\Omega(t)$ i.e in an Arbitrary Eulerian-Lagrangian formulation are:

$$\int_{\Omega(t)} \frac{\partial \mathbf{U}}{\partial t} d\Omega + \int_{\Omega(t)} \left(\frac{\partial \mathbf{F}_x}{\partial x} + \frac{\partial \mathbf{F}_y}{\partial y} \right) d\Omega = \int_{\Omega(t)} \mathbf{S} d\Omega \tag{1}$$

using Gauss theorem, we have:

$$\int_{\Omega(t)} \frac{\partial \mathbf{U}}{\partial t} d\Omega + \oint_{\partial\Omega(t)} \left(\mathbf{F}_x n_x + \mathbf{F}_y n_y \right) d\partial\Omega = \int_{\Omega(t)} \mathbf{S} d\Omega \tag{2}$$

where $\vec{n}$ is the outward normal to $\partial\Omega(t)$, and $\mathbf{F}_n$ is the normal flux defined as:

$$\mathbf{F}_n = \mathbf{F}_x n_x + \mathbf{F}_y n_y = (u n_x + v n_y)\mathbf{U} + \begin{pmatrix} 0 \\ p n_x \\ p n_y \\ p(\vec{v}_F \cdot \vec{n}) \end{pmatrix} \tag{3}$$

where $\vec{v}_F = (u, v)$ is the fluid velocity vector. Using Reynolds transport theorem to extract the time derivative:

$$\int_{\Omega(t)} \frac{\partial \mathbf{U}}{\partial t} d\Omega = \frac{d}{dt} \int_{\Omega(t)} \mathbf{U} d\Omega - \oint_{\partial\Omega(t)} \mathbf{U}(\vec{v}_G \cdot \vec{n}) d\partial\Omega \tag{4}$$

with $\vec{v}_G$ the velocity of $\partial\Omega(t)$ and we finally obtain :

$$\frac{d}{dt} \int_{\Omega(t)} \mathbf{U} d\Omega + \oint_{\partial\Omega(t)} \left[\mathbf{U}(\vec{v}_F - \vec{v}_G) \cdot \vec{n} \begin{pmatrix} 0 \\ p n_x \\ p n_y \\ p(\vec{v}_F \cdot \vec{n}) \end{pmatrix} \right]$$

$$d\partial\Omega = \int_{\Omega(t)} \mathbf{S} d\Omega \tag{5}$$

Eq. (5) shows that there are three contributions to the rate of change of $\mathbf{U}$ in $\Omega(t)$:

- Convection through $\partial\Omega(t)$ with speed $\vec{v}_r = (\vec{v}_F - \vec{v}_G)$
- Pressure surface terms
- Source terms

The domain $\Omega(t)$ is approximated by a set of N control volumes $\Omega_i(t)$. Thus, the second term of Eq. (5) is written as :

$$\oint_{\partial\Omega_i(t)} [\mathbf{F}_n - \mathbf{U}(\vec{v}_G \cdot \vec{n})] \, d\partial\Omega_i(t) = \sum_{m\in\partial\Omega_i(t)} F_m^{\perp} S_m \qquad (6)$$

where $\Omega_i(t)$ is approximated by a sum of numerical fluxes. The numerical methods for the Arbitrary Lagrangian-Eulerian formulation are described in the next section.

3. Numerical Technique

3.1. Convective fluxes

AUSM scheme [4] was used this work. its Arbitrary Lagrangian Eulerian formulation have been described in [6], [1]. We have:

$$\mathbf{F} = \begin{bmatrix} \rho \cdot \vec{v}_r \cdot \vec{n} \\ \rho \cdot \vec{v}_F \cdot \vec{v}_r \cdot \vec{n} + p \cdot \vec{n} \\ \rho \cdot H \cdot \vec{v}_r \cdot \vec{n} + p \cdot \vec{v}_G \cdot \vec{n} \end{bmatrix} \qquad (7)$$

where $\vec{v}_r = \vec{v}_F - \vec{v}_G$ is now the relative velocity.

As for the standard AUSM scheme, the convective ($\mathbf{F}^c$) and pressure ($\mathbf{F}^p$) fluxes are treated separately. The convective flux is written as:

$$\mathbf{F}^c = M_r \cdot a \cdot \Phi, \qquad \mathbf{\Phi} = \begin{bmatrix} \rho \\ \rho\vec{v}_F \\ \rho H \end{bmatrix} \qquad (8)$$

where the local Mach number is now the relative local Mach number M_r. The flux $\mathbf{F}^p$ corresponding to the acoustic waves is described as:

$$\mathbf{F}^p = \begin{bmatrix} 0 \\ p \cdot \vec{n} \\ p \cdot \vec{v}_G \cdot \vec{n} \end{bmatrix} \qquad (9)$$

in which we can note the appearance of an extra term $p \cdot \vec{v}_G \cdot \vec{n}$ depending on the mesh velocity $\vec{v}_G$.

where x_i denotes the centroid position of the control volume Ω_i. The linearly reconstructed state variables $\tilde{u}$ is calculated using least-squares method . In order to prevent the appearance of oscillations near discontinuities a flux limiter ϕ_i is needed on the reconstructed states. In the present work Venkatakrishnans limiter [7] is used.

3.2. Implicit Time integration

The time integration scheme proposed by Wuilbaut [8] which is a blending between a first-order positive time integration scheme (Backward Euler) and the 2^{nd} order accurate Backward Differentiation scheme.

$$\frac{\mathbf{U}(\mathbf{P^{n+1}}) - \mathbf{U}(\mathbf{P}^n)}{\Delta t} + \theta\left(\frac{\mathbf{U}(\mathbf{P^{n+)}}) - 2\mathbf{U}(\mathbf{P}^n) + \mathbf{U}(\mathbf{P}^{n-1})}{\Delta t}\right)$$

$$= -\mathbf{R}(\mathbf{P}^{n+1}) \qquad (10)$$

where θ is a blending coefficient $\theta \in [0, 1]$. This blending is defined such that when $\theta = 1.$, the scheme is the 2nd order Backward Differentiation scheme while when $\theta = 0.$, the scheme transforms into a 1st order Backward Euler scheme. The resulting scheme is of order two in smooth flows ($\theta = 1.$) while reducing to 1^{st} order at discontinuities ($\theta = 0$). This blending coefficient depends only on the evolution of the variable in time and acts like a time limiter defined as:

$$\theta_i = \begin{cases} \sqrt{\frac{\phi_i(r_i)}{max(1,|r_i|)}} & if \; |r_i| \geq \alpha \\ 1 & otherwise \end{cases} \qquad (11)$$

Where ϕ_i is one of the space limiter function, in this work we use MINMOD limiter , α is a threshold parameter and r_i is the ratio of temporal slopes at any given point :

$$r_i = \frac{\frac{U_i^{n+1} - U_i^n}{\Delta t}}{\frac{U_i^n - U_i^{n-1}}{\Delta t}} \qquad (12)$$

. This definition preserves the 2^{nd} order accuracy for sufficiently smooth solution. At each time step, the system (10) is solved implicitly until convergence through a Newton iteration. At each of the inner time step iterations, the value of θ is updated using the solution $U^{n+1,k}$ where k is the inner iterations index. The GMRES algorithm with an Additive Schwartz preconditioner provided by the PETSC library serves to solve in parallel the corresponding linear systems arising from Newton linearization. The solution update is also performed in natural variables.

4. Flow prediction in the driver-driven tube

Numerical investigations of the flow in the diver-driven part the VKI-Longshot facility is performed using ALE solver in COOLFluiD framework [3] [8]. Fig. 2 shows a schematic of the driver-driven part of the VKI-Longshot facility. The driver tube has a length of 6.095 m and an internal diameter of 127 mm. The driven tube is 27.50m long and an internal diameter of 76.2mm.

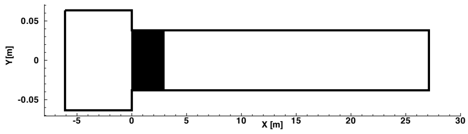

Figure 2: VKI-Longhost: driver-driven part

In the current work, the driver and the driven were considered as a one tube with the same diameter. The length of the driver tube was modified in order to keep the same volume of the gas as it is used in the real geometry. This approximation simplify the re-meshing algorithm, and eliminate the chamber effect.

Figure 3: VKI-Longshot : simplified driver-driven geometry

The test condition concerning the pressures in the dirver and driven tubes are given un table 1 and the data related to the piston are given in table 2.

P_{driver} [Pa]	P_{driven} [Pa]
344.7	275800

Table 1: Initial driver-driven pressure for high Reynolds test conditions

Mass [kg]	Length [m]
4.592	0.355

Table 2: Piston Mass and length for high Reynolds test conditions

The numerical problem to be solved and the computational domain that is used are shown in Fig. 4.

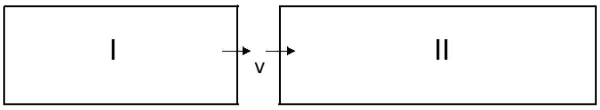

Figure 4: Computational domain

s

The physical domain (driver-driven tube) is divided into two subdomains, the left domain represents the driver tube and the right domain is the driven tube. The piston is simulated using moving boundaries of the two subdomains. The dynamic of the piston is implemented using Newton law. The only force (considered in this work) that apply on the piston are the sum of pressures on each face. Each time step, the displacement of the piston is computed allowing it advancement in time. Rigid mesh strategy is used to compute the mesh at each time steps, the nodes are equally redistributed on the boundaries allowing strong mesh deformation.

5. Results

Unsteady numerical simulation of the moving piston inside the driven tube has been performed. The initial conditions are given in table 1, the end of the driven tube is closed, and a wall is imposed as a boundary condition. This analysis is valid only during the first 5 ms of the full experimental test. In real conditions the diaphragm at the end of the driven tube beaks after the initial shock created by the piston strikes the end of the driven tube, then the dynamic of the piston depends also on what is happening outside the driven-driven tubes, i.e the flow in the nozzle.

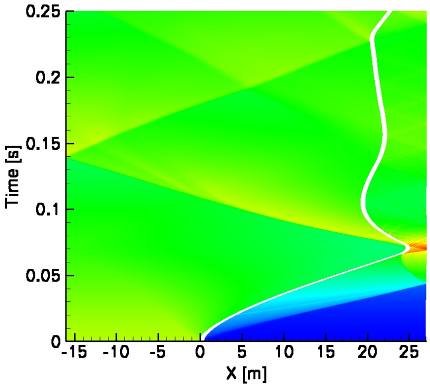

Figure 5: X-time Diagram : $Log[p]$ field

Fig. 5 shows pressure field in logarithmic scale, the white space in the filed shows the trajectory of the piston during the 25 ms. The expansion waves and the shock ahead of the piston before its rebound are shown in Fig. 6. After colliding with the reflected shock from the end of the driven tube, the piston is decelerated before a complete stop and changing its directions speed, thus creating anther compression wave which is traveling to the driver tube. The primary shock hits the end of the driver tube after 4.3 ms, time at which the diaphragm breaks.

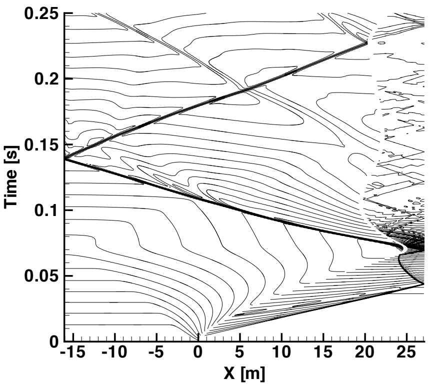

Figure 6: X-time Diagram : iso-pressure [Log_p] lines

Fig. 7 shows the pressure on the back face of the piston, It decreases due to the expansion fan behind the piston then it starts increasing when the piston decelerates. The pic conditions are reached when the piston changes its direction.

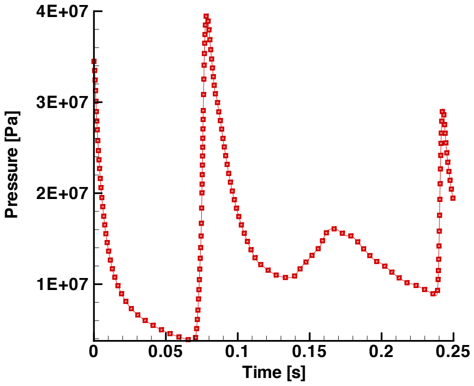

Figure 7: Pison: pressure at the back face

Fig. 8 shows the speed and the position of the piston along time. The maximum speed of 475 m/s is reached after 6ms. The piston stops at 24.75 m, goes back in the opposite direction and continue going back and forth driven by the pressure gradient on its back and front faces. There is no mechanism to stop the piston inside the facility, however a check valves are used in order to maintain the pressure in the reservoir when the piston starts going backward. These check valve were not taken into account in this current work.

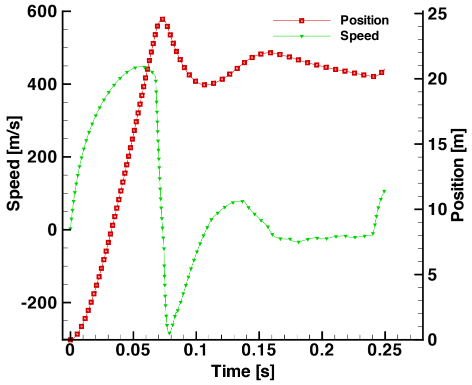

Figure 8: Piston: speed and position

6. Conclusions

Numerical simulation of a moving piston in VKI-Longshot hypersonic facility was performed using Arbitrary Lagrangian-Eulerian solver. This work was a first step throughout a complete simulation of the facility. It was necessary in order to understand the dynamic of the piston inside the driven-driver part of the facility before going any step further. The range of velocities and pressures involved in the first stage of the test were identified. The next step is a validation of the ALE solver with experimental data. Finally, diaphragm boundary condition has to be developed in order to couple the driver-driven tube with the hypersonic contoured nozzle and achieve the simulation the the full facility.

References

[1] D. Darracq, S. Champagneux, and A. Corjon. omputation of unsteady turbulent airfoils with an aeroelastic ausm+ implicit solver. *AIAA*, (98-2411), 1998.

[2] C.W Hirt. An arbitrary lagrangian-eulerian computing technique. volume 8. PHYSICS AND ASTRONOMY, 1971.

[3] Andrea Lani, Tiago Quintino, Dries Kimpe, and Herman Deconinck. The coolfluid framework - design solutions for high-performance object oriented scientific computing software. In *International Conference Computational Science 2005*, volume 1, pages 281–286, Atlanta, 2005. Springer-Verlag.

[4] M. S. Liou. A sequel to ausm, part ii: Ausm$^+$-up for all speeds. *Journal of Computational Physics*, 214:137–170, 2006.

[5] G. Simeonides. The contoured mach 15 longshot nozzle: final design parameters and construction. Internal note 87, von Karman Institute for Fluid Dynamics, September 1989.

[6] R. Smith. A geometrically conservative arbitrary lagrangian-eulerian flux splitting scheme. *Journal of computational physics*, 17(150):268–286, 1999.

[7] S. Venkateswaran and Ch. L. Merkle. Analysis of preconditioning methods for the Euler and Navier-Stokes equations.

VKI LS 1999-03, von Karman Institute for Fluid Dynamics, St.-Genesius-Rode, Belgium, March 1999.

[8] T. Wuilbaut. *Multi-Physics*. PhD thesis, Université Libre de Bruxelles, 2008.

Residual Distribution Methods For Atmospheric Entry Aerothermodynamics

Jesús Garicano Mena[1]

Aeronautics and Aerospace Department, von Karman Institute for Fluid Dynamics, Belgium, jesus.garicano.mena@vki.ac.be

Supervisor: Herman Deconinck

Professor, Aeronautics and Aerospace Department, von Karman Institute for Fluid Dynamics, Belgium, deconinck@vki.ac.be

Co-Supervisor: Andrea Lani

Research Engineer, Aeronautics and Aerospace Department, von Karman Institute for Fluid Dynamics, Belgium, lani@vki.ac.be

University Supervisor: Gérard Degrez

Professor, Service Aéro-Thermo-Mécanique, von Karman Institute for Fluid Dynamics, Belgium, Gerard.Degrez@ulb.ac.be

---

Abstract

In the present contribution the issue of simulating hypersonic flows by means of Residual Distribution Schemes is discussed. In particular, this discretization technique is briefly presented and its current capabilities reviewed. It turns out that certain aspects of the technique need some adjustments to deal with the very particular characteristics of the hypersonic regime. Extensive attention is given to the subject of enforcing conservation at the discrete level by means of a suitable conservative linearization.

Keywords: Residual distribution schemes, Conservative Linearization, Non-equilibrium Flow,Hypersonic flow, Compressible Flow.

---

1. Introduction

Numerical simulation of hypersonic flows is a challenging activity, since the complexities of compressible flow aerodynamics have to be addresed together with additional high-temperature effects due to thermal and chemical non equilibrium (or **TCNEQ**) phenomena (further details in [1]).

In the present contribution, we propose to use the Residual Distribution [2] (**RD**) framework for the discretization of the equations that govern the non-equilibrium hypersonic flow of air, as presented in [2]. The system of equations dealt with there expresses the conservation of mass, momentum and energy and can be cast in compact, vector form as:

$$\frac{\partial \vec{U}}{\partial t} + \nabla \cdot \bar{\bar{F}}^c = \nabla \cdot \bar{\bar{F}}^d + \vec{S}, \tag{1}$$

where $\vec{U}$ stands for the vector of conserved variables. For a two temperatures, N chemical species model, $\vec{U}$ includes the species densities ρ_s, the momentum ρu_j and the total ρE and electronic-vibrational energies ρe^v:

$$\vec{U} = \left[\rho_s, \quad \rho u_j, \quad \rho E, \quad \rho e^v\right]^t. \tag{2}$$

Tensors $\bar{\bar{F}}^c$ and $\bar{\bar{F}}^d$ describe the convective and diffusive fluxes of the conserved quantities, while vector $\vec{S}$ contains the chemical and internal energy modes source terms.

Several advantageous features of **RD** schemes justify our conviction of their suitability for the simulation of hypersonic flows. Among them, we stress the following:

- A maximum principle (Local Extrema Diminishing) borrowed from FVM, which allows to capture discontinuities monotonically on general unstructured grids;

---

[1] The author's research is funded by a *FRIA* fellowship provided by the FNRS.

[2] Sometimes **RD** methods are called fluctuation splitting (**FS**) as well.

- Being based on FE approximation theory, it is possible to obtain, on a compact stencil, 2nd order accurate solutions on unstructured grids;
- A better grid insensitivity on simplicial meshes, thanks to a built-in multidimensional dissipation property.

The reasons above encourage the application of **RD** schemes to the simulation of atmospheric entry flow problems. Nevertheless, the particular features of hypersonic flows prevent straightforward application of the method in its present form, since some details are not properly understood or still missing. This contribution focuses on how to enforce conservation at the discrete level, which is essential to capture accurately flow discontinuities.

In the following section, the problem found when trying to extend the Roe averaging procedure[3] (or its multidimensional counterpart[4]) to non-equilibrium flows is reported. Immediately after, a strategy to guarantee discrete conservation taken from the literature is presented and adapted for the N species, 2 temperatures thermo-chemical model we employ; its characteristics are then thoroughly detailed. After stating our conclusions, we close this contribution with a brief appendix containing the basics on **RD** schemes.

2. The importance of discrete conservation

The **RD** formalism has been applied to systems of equations structurally alike to that in Eq. 1, *e.g.*the Navier-Stokes equations for the turbulent flow of a Perfect Gas, as reported in [5] and [6].

For doing so, Eq. 1 is recast in quasilinear form before discretising it by means of **RD** :

$$\frac{\partial \vec{U}}{\partial t} + \bar{\bar{A}}_j^c \cdot \frac{\partial \vec{U}}{\partial x_j} = \nabla \cdot \bar{\bar{F}}^d + \vec{S}, \tag{3}$$

where $\bar{\bar{A}}_j^c$ stands for the Jacobian of the convective flux tensor with respect to the conserved variables $\vec{U}$:

$$\bar{\bar{A}}_j^c = \frac{\partial \vec{F}_j}{\partial \vec{U}}. \tag{4}$$

The steady state residual for cell Ω is defined as:

$$\vec{\Phi}^{\Omega} = \int_V \left(\bar{\bar{A}}_j^c \cdot \frac{\partial \vec{U}}{\partial x_j} - \frac{\partial \vec{F}_j^d}{\partial x_j} - \vec{S}^U \right) dV = \vec{\Phi}^{c,U} - \vec{\Phi}^{d,U} - \vec{\Phi}^{S,U}. \tag{5}$$

In the subsequent discussion we will consider only the convective contribution to the cell residual. Details on the dissipative and source terms discretization are given in the Appendix.

An essential ingredient for the applications reported in [5] and [6] is the possibility to represent the solution as a linear combination of nodal variables $\vec{Z}_j$, as in Eq. 34, such that an average state $\hat{\vec{Z}}$ can be defined at every simplex, with the property that when the Jacobian matrices of the convective term in Eq. 4 are evaluated at it, the following relation is satisfied:

$$\begin{aligned}\vec{\Phi}^{\Omega,c} &= \oint_{\delta\Omega} \bar{\bar{F}}^c \cdot \vec{n}\, ds = \int_\Omega \frac{\partial \vec{F}_j^c}{\partial x_j} dv = \int_\Omega \frac{\partial \vec{F}_j^c}{\partial \vec{Z}} \cdot \frac{\partial \vec{Z}}{\partial x_j} dv \\ &= \left(\int_\Omega \frac{\partial \vec{F}_j^c}{\partial \vec{Z}} dv \right) \cdot \left. \frac{\partial \vec{Z}}{\partial x_j} \right|^h = \Omega \frac{\partial \vec{F}_j^c}{\partial \vec{Z}} \left(\hat{\vec{Z}} \right) \cdot \left. \frac{\partial \vec{Z}}{\partial x_j} \right|^h = \\ &\qquad \Omega\, \bar{\bar{A}}^c \left(\hat{\vec{Z}} \right) \cdot \vec{n} \cdot \underbrace{\frac{\partial \vec{U}}{\partial \vec{Z}} \left(\hat{\vec{Z}} \right) \cdot \left. \frac{\partial \vec{Z}}{\partial x_j} \right|^h}_{\left. \frac{\partial \vec{U}}{\partial x_j} \right|^{consistent}}. \end{aligned} \tag{6}$$

That is, Eq. 6 just states that evaluating the cell convective residual as the product of the Jacobian matrices and the consistent gradient of the conserved variables is equivalent to computing the contour integral of the fluxes across the boundaries of the simplex. This means that the numerical solution obtained respects a conservation principle, which is crucial when simulating flow fields including discontinuities.

For the Perfect Gas case, the variable $\vec{Z}$ is, as in [3]:

$$\vec{Z} = \left[\sqrt{\rho}, \quad \sqrt{\rho} u_j, \quad \sqrt{\rho} H \right]^t, \tag{7}$$

and the average state is -for the multidimensional case- the one corresponding to [4]:

$$\hat{\vec{Z}} = \sum_{i=1}^{d+1} \frac{\vec{Z}_i}{d+1}, \tag{8}$$

where d is the physical dimensionality of the problem.

However, for the general N species, 2 temperatures model we intend to employ for non-equilibrium hypersonic flow computations, obtaining a single, physically meaningful average state is by no means trivial. The difficulty comes from the fact that the pressure, given by:

$$p = \sum_{i=1}^{N} \left(\frac{R}{M_s} \rho_s \right) T, \tag{9}$$

cannot be expressed explicitly in terms of the components of a corresponding $\vec{Z}$ vector.

A reformulation of **RD** schemes guaranteeing conservation (known as Contour Integration Based Residual Distribution or **CRD** scheme, see in [7]) is available; **CRD** schemes are unfortunately not applicable for general hypersonic applications since they sometimes fail in providing monotone solutions across discontinuities, as reported in [8]. This event leads us to resort to the original Linearization Based **RD** approach, as described in [5], based on the multidimensional generalization of the Roe parameter vector described in [4].

In the following section we describe one possible strategy to uniquely define an average state which guarantees conservation at the discrete level.

3. Enforcing discrete conservation for non-equilibrium flow computations

Liu and Vinokur presented a strategy to guarantee discrete conservation when employing the Roe scheme to simulate the hypersonic flow of gas mixtures out of thermal and chemical equilibrium, in [9]. Degrez and van der Weide extended Liu and Vinokur's formulation, limited to dimensionally splitted solvers, to the multidimensional upwind context, though only for chemically reacting flows, in reference [10]. In what follows, we extend the results of Degrez and van der Weide for the case of a non-ionized gas in **TCNEQ** conditions.

Following the path traced by Degrez, we define the variable:

$$\vec{Z} = \left[\sqrt{\rho}\vec{Y}^t, \quad \sqrt{\rho}\vec{u}^t, \quad \sqrt{\rho}H, \quad \sqrt{\rho}e^v \right]^t. \tag{10}$$

The convective flux vector in Eq. 1 is, for the **TCNEQ** case:

$$\vec{F}_j^c = \left[\rho_s u_j, \quad \rho u_i u_j + p\vec{1}_j, \quad \rho H u_j, \quad \rho e^v u_j \right]^t, \tag{11}$$

and the following splitting is possible:

$$\vec{F}_j^c = \underbrace{\left(\vec{F}_j^c - [\vec{0}_{Nx1}, p\vec{1}_j, 0, 0]^t \right)}_{\vec{Q}} + \underbrace{[\vec{0}_{Nx1}, p\vec{1}_j, 0, 0]^t}_{\vec{\Pi}}. \tag{12}$$

It is evident that all terms in $\vec{Q}$ can be expressed as quadratic functions of the components of $\vec{Z}$, and thus entries in $\frac{\partial \vec{Q}}{\partial \vec{Z}}$ will simply be linear functions. On the other hand $\vec{\Pi}$ just contains the pressure. But more than in pressure itself, we are interested in its differential, which can be expressed -following reference [9]- as:

$$dp = \sum_{s=1}^{N} \alpha_s \, d\rho_s + \beta \, d\rho e^{tr}, \tag{13}$$

where terms α_s and β stand respectively for the partial derivatives of pressure with respect to the species densities and the translational-rotational energy, given by:

$$\alpha_s = \frac{\partial p}{\partial \rho_s} = \frac{R}{M_s} T - \beta e_s^{tr},$$
$$\beta = \frac{\partial p}{\partial \rho e^{tr}} = \frac{\sum_{s=1}^{N} y_s \frac{R}{M_s}}{\sum_{s=1}^{N} y_s C_{v,s}^{tr}}, \tag{14}$$

where e_s^{tr} is the s-th species contribution to the translational-rotational energy, $C_{v,s}^{tr}$ is the s-species translational-rotational specific heat at constant volume and y_s is the mass fraction.

In order to employ this principle in a multidimensional upwind framework, we consider:

$$\nabla p = \sum_{s=1}^{N} \alpha_s \, \nabla \rho_s + \beta \, \nabla \rho e^{tr}, \tag{15}$$

which can be immediately recast in terms of the components of parameter vector in Eq. 10 by using the relation:

$$\rho e^{tr} = \rho H - \frac{\rho \vec{u}^t \cdot \vec{u}}{2} - \rho e^v - p, \tag{16}$$

and considering:

$$\begin{aligned}
\rho_s &= \left(\sum_{r=1}^{N} \sqrt{\rho} y_r \right) \sqrt{\rho} y_s, \\
\rho \vec{u}^t \cdot \vec{u} &= \sqrt{\rho}\vec{u}^t \cdot \sqrt{\rho}\vec{u}, \\
\rho H &= \left(\sum_{r=1}^{N} \sqrt{\rho} y_r \right) \sqrt{\rho} H, \\
\rho e^v &= \left(\sum_{r=1}^{N} \sqrt{\rho} y_r \right) \sqrt{\rho} e^v.
\end{aligned} \tag{17}$$

At this point, if it is possible to find values for α_s and β for which Eq. 15 holds, then the gradient of pressure will be defined in terms of $\vec{Z}$, making in turn $\frac{\partial \vec{\Pi}}{\partial \vec{Z}}$ a linear function of the parameter vector as well, so that evaluating $\bar{A}_j^c$ at an averaged state, as that in Eq. 8, would provide a conservative convective flux.

The problem is, however, that Eq. 15 provides as many equations as the dimensionality d of the problem (namely 1, 2 or 3) while $N + 1$ parameters have to be defined for the case of a non-ionized N species gas mixture.

In order to determine these $N + 1$ parameters, we can interpret Eq. 15 as d restrictions:

$$r_j \equiv \frac{\partial p}{\partial x_j} \beta - \sum_{s=1}^{N} \frac{\partial \rho_s}{\partial x_j} \alpha_s - \frac{\partial \rho e^{tr}}{\partial x_j}, \quad j = 1 \ldots d, \tag{18}$$

that the solution we seek for should respect. In that case, it would be sensible to look for a solution which, while fulfilling the aforementioned restrictions (guaranteeing thus conservation), is the closest one to a given a priori approximation, like for example the nodal averages:

$$\hat{\alpha}_s = \sum_{i=1}^{d+1} \frac{\alpha_s|_i}{d+1} \quad \hat{\beta} = \sum_{i=1}^{d+1} \frac{\beta|_i}{d+1}. \tag{19}$$

Under these hypotheses, we are faced with a constrained minimization problem. According to Liu [9], in order not to obtain a solution dependent on the arbitrary reference enthalpy entering in the definition of the parameters α_s, it is better to work on the space $\{\xi_1, \ldots, \xi_N; \omega\}$, where:

$$\xi_s = \frac{\alpha_s}{\beta}, \; s = 1, \ldots, N; \quad \omega = \frac{1}{\beta} \tag{20}$$

We can define then the Lagrangian:

$$\begin{aligned} \mathcal{L} \equiv D - \lambda_{x_j} r_{x_j} = (\omega - \hat{\omega})^2 + \frac{1}{\hat{\sigma}^2} \sum_{s=1}^{N} \left(\xi_s - \hat{\xi}_s\right)^2 \\ - \vec{\lambda}^t \cdot \left(\nabla p \, \omega - \sum_{s=1}^{N} \nabla \rho_s \, \xi_s - \nabla \rho e^{tr}\right), \end{aligned} \tag{21}$$

where the factor $\frac{1}{\hat{\sigma}^2}$ is included for dimensional consistency, σ being typically of the order of the local speed of sound.

The corresponding stationary conditions are:

$$\begin{aligned} \frac{\partial \mathcal{L}}{\partial \xi_r} &= \frac{2}{\hat{\sigma}^2} \left(\xi_r - \hat{\xi}_r\right) + \vec{\lambda}^t \cdot \nabla \rho_r = 0, \quad r = 1 \ldots N, \\ \frac{\partial \mathcal{L}}{\partial \omega} &= 2\,(\omega - \hat{\omega}) - \vec{\lambda}^t \cdot \nabla p = 0, \\ \frac{\partial \mathcal{L}}{\partial \lambda_j} &= \frac{\partial p}{\partial x_j} \beta - \sum_{s=1}^{N} \frac{\partial \rho_s}{\partial x_j} \alpha_s - \frac{\partial \rho e^{tr}}{\partial x_j}, \quad j = 1 \ldots d. \end{aligned} \tag{22}$$

Fig. 1 shows the graphical interpretation of the minimization problem defined by the Lagrangian in Eq. 21 for a $2D$ computation and a 2 species mixture: starting from an approximation $\hat{P}$ in the space $\{\xi_r; \omega\}$, we look for the closest point $\tilde{P}$ which fulfills at the same time the $d = 2$ restrictions, that is, lies on the line where the blue and the green planes intersect.

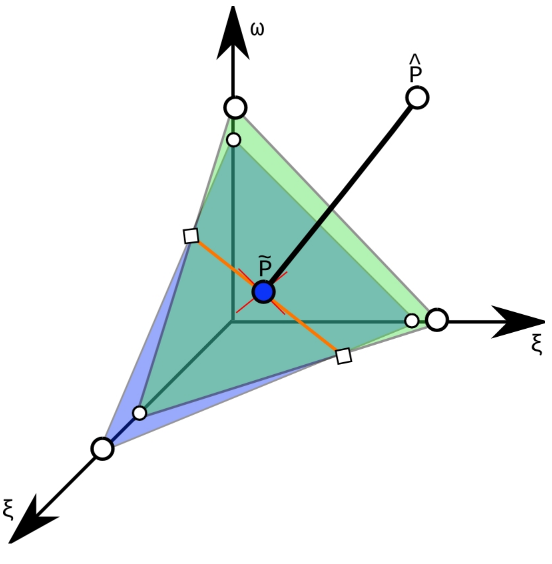

Figure 1: Constrained minimization problem: graphical interpretation.

Out of this stationary conditions, a linear system of equations is obtained:

$$\mathcal{A} \cdot \vec{x} = \vec{b}, \tag{23}$$

which consist, after application of elemental operations, of the coefficient matrix $\mathcal{A}$:

$$\mathcal{A} = \left[\begin{array}{c|c|cc} I_N & 0 & \frac{\hat{\sigma}^2}{2} \frac{\partial \rho \vec{Y}}{\partial x} & \frac{\hat{\sigma}^2}{2} \frac{\partial \rho \vec{Y}}{\partial y} \\ \hline \vec{0}_{1\times N} & 1 & -\frac{1}{2} \frac{\partial p}{\partial x} & -\frac{1}{2} \frac{\partial p}{\partial y} \\ \hline \vec{0}_{1\times N} & 0 & C_{xx} & C_{xy} \\ \vec{0}_{1\times N} & 0 & C_{xy} & C_{yy} \end{array}\right], \tag{24}$$

of the vector of unknowns $\vec{x}$:

$$\vec{x} = \left[\xi_1, \ldots, \xi_N; \omega; \lambda_{x_j}\right]^t, \tag{25}$$

and of the forcing vector $\vec{b}$:

$$\vec{b} = \left[\hat{\xi}_1, \ldots, \hat{\xi}_N; \hat{\omega}; -\hat{\omega}\, \delta p_{x_j}\right]^t, \tag{26}$$

where $C_{x_i x_j}$ stands for:

$$C_{x_i x_j} = \frac{1}{2} \left(\frac{\partial p}{\partial x_i} \frac{\partial p}{\partial x_j}\right) + \hat{\sigma}^2 \sum_{s=1}^{N} \left(\frac{\partial \rho_s}{\partial x_i} \frac{\partial \rho_s}{\partial x_j}\right), \tag{27}$$

while δp_{x_j} is:

$$\delta p_{x_j} = (1 + \hat{\omega}) \frac{\partial p}{\partial x_j} - \sum_{s=1}^{N} \frac{\partial \rho_s}{\partial x_j} \hat{\xi}_s - \frac{\partial \rho e^{tr}}{\partial x_j}. \tag{28}$$

The structure of the linear system in Eq. 23 is such that a $d \times d$ subsystem:

$$\mathcal{B} \vec{\lambda} = -\omega \vec{\delta p}, \tag{29}$$

can be isolated, and once $\vec{\lambda}$ is determined (assuming that a solution exists), ξ_s and ω can be immediately obtained by back substitution.

Concerning the invertibility of $\mathcal{B}$, its determinant can be proven to be:

$$\begin{aligned} |\mathcal{B}| = \hat{\sigma}^2 \Bigg(\hat{\sigma}^2 \sum_{k,l=1,k\neq l}^{N} \left(\frac{\partial \rho_k}{\partial x} \frac{\partial \rho_l}{\partial y} - \frac{\partial \rho_k}{\partial y} \frac{\partial \rho_l}{\partial x}\right)^2 \\ + \sum_{k=1}^{N} \left(\frac{\partial \rho_k}{\partial x} \frac{\partial p}{\partial y} - \frac{\partial \rho_k}{\partial y} \frac{\partial p}{\partial x}\right)^2 \Bigg) \geq 0, \end{aligned} \tag{30}$$

being 0 only if planes r_j are coincident, but in that case we do not face a system of equations but rather a scalar equation, which poses no problem to invert.

The solution for the case $|\mathcal{B}| > 0$ is given by:

$$\lambda_x = \frac{C_{yy}\, \delta p_x - C_{xy}\, \delta p_y}{C_{xx}\, C_{yy} - C_{xy}\, C_{xy}}, \quad \lambda_y = \frac{C_{xx}\, \delta p_y - C_{xy}\, \delta p_x}{C_{xx}\, C_{yy} - C_{xy}\, C_{xy}}. \tag{31}$$

and the values of the pressure derivatives guaranteeing conservation are:

$$\begin{aligned} \tilde{\omega} &= \hat{\omega} + \frac{1}{2} \left(\lambda_x \frac{\partial p}{\partial x} + \lambda_y \frac{\partial p}{\partial y}\right), \\ \tilde{\xi}_s &= \hat{\xi}_s - \frac{\hat{\sigma}^2}{2} \left(\lambda_x \frac{\partial \rho_s}{\partial x} + \lambda_y \frac{\partial \rho_s}{\partial y}\right). \end{aligned} \tag{32}$$

The values that are actually employed in the computation are obtained in a straightforward manner from:

$$\tilde{\beta} = \frac{1}{\tilde{\omega}}, \quad \tilde{\alpha}_s = \tilde{\beta}\,\tilde{\xi}_s. \tag{33}$$

Now that the linearization procedure is well understood, and after testing it in a **FVM** framework, our next step will be to implement it in the non-equilibrium `COOLFluiD` **RD** solver .

4. Conclusions

In the present contribution the importance of having numerical schemes respecting conservation at the discrete level has been discussed. The reasons which make defining a conservative average state an involved task for flows out of equilibrium have been pointed out. A strategy to obtain a conservative linearization has been identified in the literature, and subsequently adapted to be applicable to the N chemical species, 2 temperatures model, and this into the multidimensional upwind framework of our interest. A theoretical analysis on the linearization procedure, and its limits of validity has been performed.

Residual Distribution Schemes: the basics.

A very short review of **RD** for the discretization of (1) is presented in this appendix. The interested reader will find extensive explanations in [5], [11] and [12].
The solution is expressed by means of a finite element representation on P1 linear triangles.

$$\vec{U}^h(\vec{x}, t) = \sum_{j=1}^{\#DOF} \vec{U}_j(t)\, N_j(\vec{x}) \tag{34}$$

where the following property holds:

$$N_j(\vec{x}_k) = \delta_{jk} \tag{35}$$

The steady state residual for cell Ω is defined as:

$$\vec{\Phi}^{\Omega} = \int_{\Omega} \left(\frac{\partial \vec{F}^c_j}{\partial x_j} - \frac{\partial \vec{F}^d_j}{\partial x_j} - \vec{S}^U \right) dv = \vec{\Phi}^{c,U} - \vec{\Phi}^{d,U} - \vec{\Phi}^{S,U} \tag{36}$$

with contributions from the convective, dissipative and source terms.

The nodal system of equations is obtained by distributing fractions of the cell residuals $\vec{\Phi}^{\Omega}$ to the nodes forming part of the cell. The convective contribution to the nodal equation of the cell residual is expressed generically as:

$$\vec{\Phi}^{c,U}_l = \sum_{\Omega_i \in \Xi_l} B_l^{\Omega_i,U}(K^{\pm}) \cdot \vec{\Phi}^{c,U}_{\Omega_i}$$

in terms of the so called distribution matrices $B_l^{\Omega_i,U}$, which depend in turn on the nodal upwind parameters:

$$K_j = A_{j,x}\, n_{j,x} + A_{j,y}\, n_{j,y} + A_{j,z}\, n_{j,z} \tag{37}$$

where A_{j,x_d} is the Jacobian of the advective flux along direction x_d, and n_{j,x_d} are the components of the vectors normal to the element faces.

Different forms of the $B_l^{\Omega_i,U}$ matrices define different schemes. In this work, multidimensional, positive matrix N-scheme (further details in [5]) has been employed.

Distribution of diffusive contributions to the cell residual is done, when a $P1$ element mesh is used, by Galerkin discretization:

$$\vec{\Phi}^{d,U}_j = \int_{\Omega} \beta_j\, \nabla \cdot \bar{\bar{F}}^v\, dv \tag{38}$$

while source terms can be distributed either with the Galerkin method or together with the advective residual.

From the distribution process introduced before results a system of differential equation controlling the time evolution of the solution at the grid nodes. For l-th node, it is:

$$\Xi_l \frac{d\vec{U}_l}{dt} + \vec{\Phi}^{c,U}_l - \vec{\Phi}^{d,U}_l - \vec{\Phi}^{S,U}_l = \vec{0}, \tag{39}$$

where Ξ_l stands for the volume of the median dual cell around l-th node.

Acknowledgment

The author expresses his gratitude to his supervising team, Professors Deconinck and Degrez, and Dr. Lani for their continuous encouragement and support. The funding coming from von Karman Institute and FNRS, through a FRIA fellowship is gratefully acknowledged.

References

[1] J. D. Anderson, Hypersonic and High Temperature Gas Dynamics, McGraw Hill, New York, 1989.

[2] Gnoffo, P., Gupta, R. and Shinn, J., Conservation equations and physical models for hypersonic air flows in thermal and chemical non-equilibrium, TP 2867, NASA (1989).

[3] Roe, P.L., Approximate Riemann Solvers, Parameter Vectors, and Difference Schemes, Journal of Computational Physics 43 (1981) 357–372.

[4] Deconinck, H., Roe, P.L. and Struijs, R., A multidimensional generalization of Roe's flux difference splitter for the euler equations, Computers and Fluids 22 (2-3) (1993) 215–222.

[5] van der Weide, E., Compressible flow simulation on unstructured grids using multi-dimensiona upwind schemes, Ph.D. thesis, Technische Universitet Delft (1998).

[6] Sermeus, K. and Deconinck, H., Solution of steady euler and navier-stokes equations using residual distribution schemes, LS 2003-05, VKI (2003).

[7] Csik, A., Ricchiuto, M. and Deconinck, H., Conservative formulation of the multidimensional upwind residual distribution schemes for general nonlinear conservation laws, Journal of Computational Physics 179 (1) (2002) 286–312.

[8] Lani, A., Garicano Mena, J. and Deconick, H., A residual distribution method for symmetrized systems in thermo-chemical nonequilibrium, in: Proceedings of the 20^{th} AIAA Computational Fluid Dynamics Conference, AIAA, Honolulu (Hawaii), 2011.

[9] Liu, Y. and Vinokur, M., Upwind algorithms for general thermo-chemical nonequilibrium flows, in: 46^{th} AIAA Aerospace Sciences Meeting and Exhibit., Reno, 1989.

[10] G. Degrez, E. van der Weide, Upwind residual distribution schemes for chemical non-equilibrium flows, in: Collection of Technical Papers. Vol. 2, AIAA, 1999, pp. 978–987.

[11] Ricchiuto, M., Construction and analysis of compact residual distribution discretizations for conservation laws on unstructured meshes, Ph.D. thesis, Université Libre de Bruxelles (2005).

[12] Villedieu, N., High order discretisation by residual distribution schemes, Ph.D. thesis, Université Libre de Bruxelles (2009).

Stagnation Line Approximation for Ablation Thermochemistry

Julien de Mûelenaere

Aeronautics and Aerospace Department, von Karman Institute for Fluid Dynamics, Belgium, julien.demuelenaere@vki.ac.be

Supervisor: Thierry Magin

Assistant Professor, Aeronautics and Aerospace Department, von Karman Institute for Fluid Dynamics, Belgium, magin@vki.ac.be

---

Abstract

A stagnation line formulation is derived for ablation thermochemistry and used to solve for the distribution of species, density, and enthalpy in a chemically active boundary layer. The formulation is used to compute B'-tables that include the mass diffusion terms and the effects of wall blowing on the boundary layer. This formulation avoids the need of a blowing correction used in material response modeling. B'-tables are commonly used in ablative material response modeling to determine the consumption rate of material at the surface, B'_c, as a function of pyrolysis gas mass flux, B'_g, temperature and pressure. A thin control volume is considered where conservation of mass, equilibrium chemistry, and the transfer potential approximation to the diffusion transport terms are used to determine B'-tables as a function of temperature and pressure. The sensitivity of the tables to using equilibrium chemistry coefficients from JANAF fits, Gurvich fits and a rigid rotor/harmonic oscillator approximation is investigated. Little effect of the fits is found at temperatures below 2,250K. However, important differences at high temperatures have been identified. Differences at high temperatures were also found between B'-tables derived using the simplest mass transfer approximation and tables derived without the need to approximate the diffusion transport terms. This implies that estimates of the recession rate of ablative material in high enthalpy environments are sensitive to the approach used to build B'-tables.

Keywords: atmospheric entry flows, ablation, porous medium, chemical reactions, multi-physics coupling, Uncertainty Quantification.

---

1. Introduction

Exploration beyond low-earth orbit and sample-return missions require reentering the atmosphere at speeds above 10 km/s. In planning missions to planets with atmospheres, optimization of the mass of the fuel and the mass of the heat shield often results in high speed atmospheric entries. To achieve these missions, the mission designer relies on the availability of ablative materials. These specially designed materials harness interactions between the flow environment and the surface (gas-surface interactions) to protect the payload. They are designed to be an insulator that rejects heat by re-radiating and blowing the majority of the incident heat back into the environment. In this process, ablative materials lose mass and their surface recesses. A crucial tool in the design process of a thermal protection system is therefore a model that predicts the required thickness for the payload to remain protected during atmospheric entry.

A common strategy, first proposed by Kendall et al.[1] in 1968, is to run material and flow codes decoupled and approximate their interactions through the use of heat and mass transfer coefficients. The flow environment code uses "cold-wall" boundary conditions, i.e. independent of the material response code, but provides the heat transfer coefficients, density, pressure, enthalpy, and species mass fractions at the boundary layer edge. The material code, on the other hand, estimates the surface recession rate through the use of tables. Kendall et al.[1] generated non-dimensional pyrolysis-gas mass flux and char consumption rate, B'_g and B'_c, tables (commonly referred to as B'-tables) by considering a thin control volume where the gas-surface interactions occur and where mass balance and equilibrium chemistry are satisfied. To obtain the diffusive transport terms that appear in the mass conservation equation, they used heat and mass transfer coefficients to relate the boundary layer edge quantities to the quantities in the control volume. Because of the efficiency of this strategy, it is still followed today.[2]

A weakness in this strategy is in the model of mass transport due to diffusion into the control volume. In addition, we expect that blowing the byproducts of the ablation process into the boundary layer will change the conditions in the boundary layer. Gnoffo et al. [3] have shown that coupling the byproducts of ablation to the fluid code has an important impact on the flow environment.

While flow solvers have now been developed[3] that can bypass the use of B'-tables, efforts to tightly couple them to an in-depth material response solver are still work-in-progress. These efforts will result in large codes that are designed for applications that require massive parallel computing capability. However, there is a need for approximate solvers that can be used on a personal computer. In this paper, we develop a stagnation line formulation and use it to test one of the approximations for the diffusion mass transport suggested by Kendall et al.[1] We solve for the distribution of species, density, and enthalpy in the boundary layer given conditions at the boundary layer edge. This new capability enables us to produce B'-tables that account for diffusion and blowing into the boundary layer, and we compare these to B'-tables generated using the approximations.

The present paper is organized as follows: in section (2), the thin control volume approach of Kendall et al.[1] is revisited. Their simplest approximation is used to compare B'-tables generated using CEA[4] fits, JANAF[5] fits, and a rigid rotor/harmonic oscillator approximation to the thermodynamics.[6] In section (3), the stagnation line approximation is derived without the use of self similar coordinates to represent the boundary layer at the stagnation line. In section (4), a new approach for the generation of B'-tables is developed by means of coupling the thin control volume formulation to the stagnation line solution. Summary and conclusions are presented in section (5).

2. Thin Control Volume

The B'-tables are built based on conservation of mass and equilibrium chemistry. They are essentially a means to impose a boundary condition on an ablation code without having to couple the flow environment. To compute the equilibrium mixture, the species equilibrium constants (functions of the Gibbs free energy) are obtained from fits to the species thermodynamic properties. Modifications to the equilibrium chemistry assumption may be added to account for heterogeneous finite-rate chemistry or material failure [1]; unfortunately, this methodology relies on rates and ablation mechanisms that are not well understood[7] and will not be considered in this paper. In a companion paper, the heterogeneous finite-rate chemistry of a carbon preform is analyzed[8]. In this section, we revisit the derivation of the open control volume [1] formulation to familiarize the reader with the details of the formulation and our choice of approximation for the diffusion transport terms.

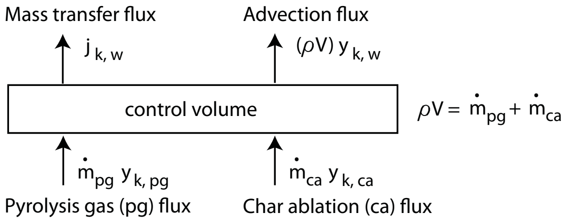

Figure 1: Mass fluxes and compositions at the wall

2.1. Mass Balance

We start with a *Thin Control Volume* (*TCV*), as shown in Fig. 1, that encloses the gas surface interface in the moving reference frame of the surface. We assume that: (1) the surface is chemically active with carbon char (C(gr)), assumed in equilibrium with the gas species, reacting with oxygen and sublimating; (2) the pyrolysis gas products and the gas from the flow environment get transported into the control volume at a rate slow compared to the chemistry time-scale, thus enabling equilibrium to be established for the mixture within the control volume. We further assume no accumulation of gas in the *TCV*. The mass balance of the elements in the control volume is given by,

$$\dot{m}_{pg} y_{k,pg} + \dot{m}_{ca} y_{k,ca} = (\rho V)_w y_{k,w} + j_{k,w} \tag{1}$$

where $y_{k,pg}$, $y_{k,ca}$, and $y_{k,w}$ are the mass fraction of the elements in the gas, the char, and the mixture, respectively; $\dot{m}_{pg}$ and $\dot{m}_{ca}$ are the pyrolysis gas mass flux and the char mass consumption rate $[kg\, m^{-2} s^{-1}]$; ρ is the density of the mixture $[kg/m^3]$; V is the velocity of the gas mixture, $[m/s]$; and $j_{k,w}$ is the diffusion flux of the elements of the mixture, $[kg\, m^{-2} s^{-1})]$ given by,

$$j_{k,w} = \sum_i \nu_k^i \frac{M_k}{M_i} J_{yi,w} \tag{2}$$

where ν_k^i are stoichiometric coefficients that are defined in Eq. 6, M_i is the molar mass of species i, and $J_{yi,w}$ is the mixture species diffusion flux.

By summing over the elements k in Eq. 1, we get the total mass conservation equation,

$$\dot{m}_{pg} + \dot{m}_{ca} = (\rho V)_w \tag{3}$$

Kendall et al.[1] considered several approximations to the species diffusion flux. The simplest of these approximations and the one we will adopt here is the transfer potential method that assumes equal mass diffusion coefficients for all species in the mixture:

$$j_{k,w} = \rho_e u_e C_M \left(y_{k,w} - y_{k,e}\right) \tag{4}$$

where ρ_e is the density of the gas at the boundary layer edge, u_e is the velocity at the boundary edge, $[m/s]$, and C_M is the Stanton number for mass transfer. Corrections to account for unequal diffusion coefficients have been proposed by Kendall et al. but are not currently used[9].

By substituting equations (3) and (4) into (1) and rearranging terms, we get the elemental composition of the mixture,

$$y_{k,w}(\dot{m}_{ca}) = \frac{\dot{m}_{pg} y_{k,pg} + \dot{m}_{ca} y_{k,ca} + \rho_e u_e C_M y_{k,e}}{\dot{m}_{pg} + \dot{m}_{ca} + \rho_e u_e C_M} \tag{5}$$

The mass fractions of the elements in the mixture, $y_{k,w}$, and the ablation mass loss rate, $\dot{m}_{ca}$, are the unknowns that we need to determine. These represent $n_c + 1$ unknowns, where n_c is the number of elements.

2.2. *Chemistry for heterogeneous mixtures*

The convention we will follow starts by expressing the formation reactions for n_s species as[9],

$$\sum_k \nu_k^j N_k \rightarrow \nu_j^j N_j \tag{6}$$

where N_k represents base species for the elements in the system, ν_k^j are the stoichiometric coefficients of the formation reactions, and N_j is the gaseous product species formed by the reaction.

2.2.1. *Gaseous mixture*

To compute the equilibrium composition of a gaseous mixture composed of n_s different chemical species, n_s independent equations are needed. We have $n_r = n_s - n_c$ independent equations obtained from the equilibrium of the formation reactions, Eq. 6, where n_c is the number of *base species* that are elements. Because of the adopted convention for the species formation reactions, n_c species formation reactions are trivial.

Equilibrium of the chemical reactions

Assuming that the species of the mixture are in chemical equilibrium, n_r equations are obtained from the definition of the equilibrium constants,

$$K_j = \left[\frac{Products}{Reactants}\right] = \frac{x_j^{\nu_j^j}}{\prod_k x_k^{\nu_k^j}} \tag{7}$$

From the above convention, the equilibrium constants are given by

$$\ln K_j(T,p) = -\frac{1}{RT}\left(\nu_j^j g_j\left(T, p_{ref}\right) - \sum_k \nu_k^j g_k\left(T, p_{ref}\right)\right) - \ln\left(\frac{p}{p_{ref}}\right)\left(\nu_j^j - \sum_k \nu_k^j\right) \tag{8}$$

where $g_i = h_i - T s_i$ is the species Gibbs free energy and p_{ref} is a reference pressure.

Mass conservation of the elements

The remaining, $n_c = n_s - n_r$, equations are obtained from the mass conservation of the nuclei,

$$\nu_k^k x_k + \sum_j \nu_k^j x_j = \nu_k^k M \frac{y_{k,w}}{M_k} \tag{9}$$

where M, the gas-phase average molecular weight ($M = \sum_i M_i x_i$), is an additional unknown in the system. At this point, we have n_s equations for $n_s + 2$ unknowns. We seek two additional relations.

Mole-Fraction definition

By definition, the mole fractions sum to one. This provides an additional equation:

$$\sum_i x_i = 1 \tag{10}$$

To summarize, for a gaseous mixture, the system of $n_s + 1$ independent equations reads:

$$\left\{\begin{array}{rcl} \nu_k^k x_k + \sum_j \nu_k^j x_j & = & \nu_k^k M y_{k,w}(\dot{m}_{ca})/M_k \\ \sum_i x_i & = & 1 \\ \nu_j^j \ln x_j - \sum_k \nu_k^j \ln x_k & = & \ln K_j \end{array}\right. \tag{11}$$

The remaining constraint is obtained by considering the condensed phase reaction.

2.2.2. Condensed phase species chemistry

In the presence of solid reacting species (as is the case for ablating materials), solid species are added to the system. Therefore, heterogeneous equilibrium reactions are needed to close the system. Our current interest is in carbon-based materials, therefore, we will consider a char composed of a single element, $C(gr)$, formed by the following elementary reaction

$$C \rightarrow C(gr) \tag{12}$$

where C is carbon gas. In the case of ablative materials, it is assumed that the solid behaves as an infinite source of condensed species when present. Therefore, the activity of the solid (or its mole fraction), is taken equal to one, $x_{C(gr)} = 1$, in heterogeneous equilibrium reactions (it is equal to zero when not present). The following system is added to the gaseous species system,

$$\left\{ \begin{array}{rcl} x_{C(gr)} & = & 1 \\ -\ln x_C & = & \ln K_{C(gr)} \end{array} \right. \tag{13}$$

The equilibrium constant for condensed-phase species reads:

$$\begin{aligned} \ln K_{C(gr)}\,(T,p) = & -\frac{1}{RT}\Big(g_{C(gr)}(T) - g_C(T, p_{ref})\Big) \\ & + \ln\left(\frac{p}{p_{ref}}\right) \end{aligned} \tag{14}$$

Fits for the Gibbs free energy of carbon graphite $g_{C(gr)}(T)$ can be found in the literature [6].

2.2.3. Complete System

The complete homogeneous/heterogeneous equilibrium chemistry system coupled to mass transfer reads

$$\left\{ \begin{array}{rcl} \nu_k^k x_k + \sum_j \nu_k^j x_j & = & \nu_k^k M y_{k,w}(\dot{m}_{ca})/M_k \\ \sum_i x_i & = & 1 \\ -\ln x_C & = & \ln K_{C(gr)} \\ \nu_j^j \ln x_j - \sum_k \nu_k^j \ln x_k & = & \ln K_j \end{array} \right. \tag{15}$$

The system is closed: we have $(n_s + 2)$ unknowns and $(n_s + 2)$ equations; M and $\dot{m}_{ca}$ are 2 additional unknowns to the mole fractions of the mixture . The system is quadratic in these unknown quantities and an iterative procedure is used to solve it. It is interesting to note that only gaseous species mole fractions appear in the system. This is due to the fact that the mole fraction of gaseous carbon C is fixed by the heterogeneous equilibrium reaction $-\ln x_C = \ln K_{C(gr)}$ as long as graphite is present in the mixture. Carbon gas is carried out of the wall by diffusion and convection simultaneously, causing ablation.

Two intensive variables need to be fixed to solve the equilibrium chemistry problem. We choose the pressure and temperature as our state variables, because they are the available variables when coupling to a material response code. The input variables are $y_{k,pg}$, $\dot{m}_{pg}$ (given by the material response code), $\rho_e u_e C_M$, and $y_{k,e}$ (e for edge; these depend on the surrounding atmposphere), $y_{k,ca}$, T_w, and p_w. The current code implementation provides $\dot{m}_{ca}$ that is needed to compute the recession rate of the surface:

$$rr = \frac{\dot{m}_{ca}}{\rho_{ca}} = \frac{[kg/m^2/s]}{[kg/m^3]} \tag{16}$$

where ρ_{ca} is the density of the charred ablative material.

The computation also provides the species composition x_i, from which the total enthalpy of the gas in the control volume, h_w, can be evaluated.

The formulation has been implemented in the existing code MUTATION[10]. We refer to the code that implements the algorithm to solve the system given by Eq. 15 as MUTATION-B. The current code may be used to generate pre-computed B'-tables. It provides the dimensionless ablation mass-loss rate, $B'c = \dot{m}_{ca}/\rho_e u_e C_M$, and the wall enthalpy as a function of pressure, temperature, and the dimensionless pyrolysis-gas flow rate $B'_g = \dot{m}_{pg}/\rho_e u_e C_M$.

2.3. Representative B'-tables for carbon fibers with pyrolysis gas from phenolic

We have outlined a procedure where given $\dot{m}_{pg}$, T_w and p_w, and $\rho_e u_e C_M$, we can compute $\dot{m}_{ca}$. Kendall et al.[1] observed that by normalizing Eq. 5 using $\rho_e u_e C_M$, the system becomes independent of the conditions at the boundary layer edge and the Stanton number. Eq. 5 was then normalized and rearranged to read,

$$y_{k,w} = \frac{B'_g y_{k,pg} + B'_c y_{k,ca} + y_{k,e}}{B'_g + B'_c + 1} \tag{17}$$

Rewriting the above equation in terms of B'_c, we get,

$$B'_c = -\frac{B'_g(y_{k,pg} - y_{k,w}) + (y_{k,e} - y_{k,w})}{(y_{k,ca} - y_{k,w})} \tag{18}$$

where $B'_g = \dot{m}_{pg}/\rho_e u_e C_M$ and $B'_c = \dot{m}_{ca}/\rho_e u_e C_M$. We recall that B'_c is the key quantity extracted from the B'-tables to compute the recession rate.

MUTATION-B developed for the system of equations outlined in the previous sections was used to study an ex-phenolic pyrolysis-gas mixture in air. Starting from a mixture of about 150 species (corresponding to the species available in the JANAF [5] and Gurvich [6] tables containing C, H, O, N), we removed species from the mixture and checked that the B' obtained did not change in the temperature range of interest, $500K$ - $4000K$. With 4 elements (C, H, O, and N) included, we were able to reduce the mixture to 19 representative species: C, H, O, N, CH, CH_4, CO, CO_2, CN, C_2, C_2H, C_2H_2, C_3, C_4, C_5, HCN, H_2, H_2O, N_2.

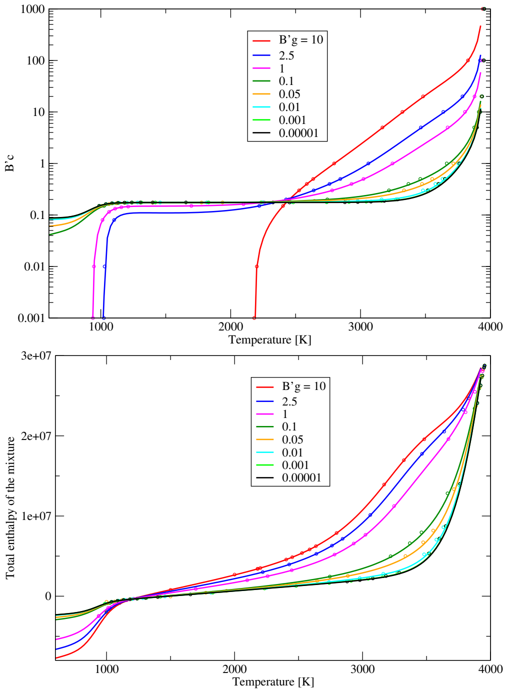

Figure 2: Char rate consumption rate as a function of temperature for a range gas injection rates. The mixture is assumed to be at $p = 1\ atm$. The solid lines are from MUTATION-B, the symbols are from MAT[9].

Figure 2 presents a typical B' table. B'_c is plotted on a logarithmic scale as a function of temperature for a range of pyrolysis-gas injection rates, B'_g. The most noticeable feature is the large plateau over a large temperature range, illustrating the fact that B'_c becomes independent of temperature at low pyrolysis gas injection rate. This illustrates the well known diffusion-limited regime where all of the oxygen transported from the boundary layer edge to the control volume is consumed at the surface. In other words, in this regime, the surface recesses at the same rate independently of the temperature. The gas composition at the wall is plotted in Fig. 3 as a function of temperature for small $\dot{m}_g$. It shows that the gas composition at the surface is independent of temperature in the diffusion-limited regime. At the surface, all of the oxygen available has been consumed by the carbon and is in the form of CO for intermediate temperatures. At lower temperatures, CO_2 is predominant at equilibrium (Boudouard equilibrium); therefore, two moles of oxygen are now necessary to remove one mole of carbon (this corresponds to the lower plateau on the left side of Fig. 2). At very high temperatures, the sublimation regime is observed leading to a sharp increase in the ablation rate.

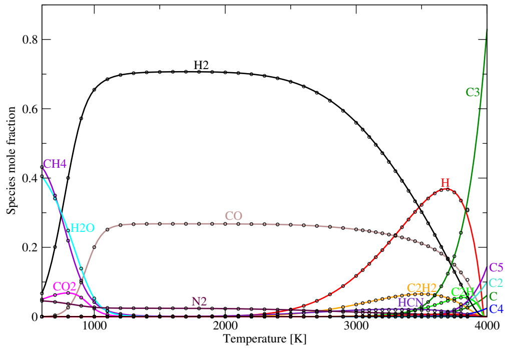

Figure 3: Species mole fractions over temperature for $p = 1atm$ and given $\dot{m}_{pg}$

2.4. Effects of the thermochemical tables on the B'-tables

A key dataset for accurate estimates of ablation rates is the equilibrium constants needed to compute the equilibrium composition. The equilibrium constants are directly related to the value of the Gibbs free energy used for each species. At least three different databases are available to compute the Gibbs free energy, g_i, from equations (8) and (14). An option is to use polynomials with coefficients obtained from the CEA[4] or the JANAF [5] thermochemical tables. Another option is to re-compute the Gibbs free energy using a rigid-rotor/harmonic-oscillator approximation based on Gurvich spectroscopic constants.

Figure 4 compares B'-tables computed using the three methods. Significant differences are observed at high temperatures in the sublimation regime. These differences will impact the predictions of material response to high-enthalpy environments.[11] Further work is necessary to analyze and decide on the most appropriate database for use in material response codes. An objective of the present work is to identify the parameters that impact the B'-tables by revisiting the original derivation and identify/verify the approximations used in the formulation.

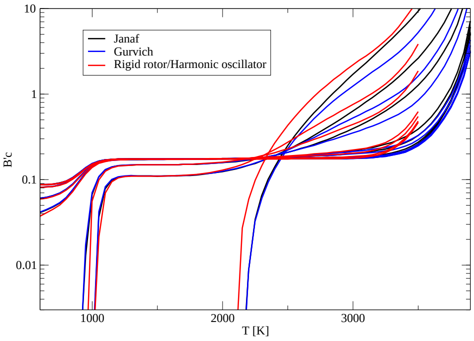

Figure 4: Comparison of Gurvich fit, JANAF fit and Rigid rotor/Harmonic oscillator

3. Stagnation Line Formulation

A major approximation in the previous B'-tables formulation is reliance on the transfer potential approximation, Eq. 4, to compute the diffusion transport. In the next section, we relax this approximation by solving the Navier-Stokes equations along the stagnation line and compute the species transport. The one-dimensional stagnation line equations are derived in this section from the boundary layer equations in cylindrical geometry. This simplification to the full Navier-Stokes equations enables us to have realistic chemistry transport models coupled to an equilibrium chemistry approximation at the boundary. We will show that this formulation will provide us with a powerful tool to develop B'-tables.

3.1. System of Equations

The governing equations written in conservative form read,

$$\frac{\partial \mathbf{Q}}{\partial t} + \frac{\partial \mathbf{G}(\mathbf{Q})}{\partial x} + \frac{\partial \mathbf{F}(\mathbf{Q})}{\partial y} = \mathbf{S} \qquad (19)$$

where $\mathbf{Q}$ is the conservative variable vector, $\mathbf{G}$ and $\mathbf{F}$ are the flux vectors, $\mathbf{S}$ is the source term, x is the coordinate system along the body, and y is along the stagnation line (see Fig.5).

Starting with the 2D axisymetric boundary layer equations [12], we expand the dependent variables, Q_i, in a Taylor series about the center line, $Q_i(x,y,t) = Q_i(0,y,t) + Q_{i,1}(0,y,t)x + Q_{i,2}(0,y,t)x^2/2 + ...$, where $Q_{i,j} = \partial^j Q_i/\partial x^j$. Substituting the expansion into the boundary layer equations and taking the limit $x \to 0$, we get

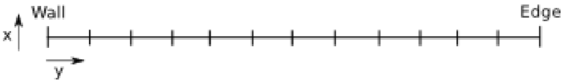

Figure 5: Coordinate system used where x is along the surface of the body and y is along the stagnation line

$$\frac{\partial}{\partial t}\begin{pmatrix}\rho \\ \rho_i \\ \rho u_{,1} \\ \rho e\end{pmatrix} + \frac{\partial}{\partial y}\begin{pmatrix}\rho v \\ \rho_i v + J_{yi} \\ \rho v u_{,1} - \mu\frac{\partial u_{,1}}{\partial y} \\ \rho v h + \phi\end{pmatrix}$$

$$= \begin{pmatrix} -2\rho u_{,1} \\ \omega_i - 2\rho_i u_{,1} \\ -\rho u_{,1e}^2 - \rho v_e \frac{\partial u_{,1}}{\partial y}|_e - 3\rho u_{,1}^2 \\ -2\rho u_{,1} h \end{pmatrix} \qquad (20)$$

Where v is the velocity along the stagnation line direction y, $u_{,1} = \partial u/\partial x$ is the partial derivative with respect to the wall direction of the velocity in that direction,

$$J_{yi} = -\rho D_{im} \partial y_i / \partial y \qquad (21)$$

is the diffusion flux,

$$\phi = -\lambda \partial T/\partial y + \sum_i J_{yi} h_i, \qquad (22)$$

is the heat flux, and ρ_i is the mass density of species i. The mixture mass density is given by the expression $\rho = \sum_i \rho_i$. The mixture energy $e = \sum_i y_i e_i$. The mass fraction $y_i = \rho_i/\rho$, mixture enthalpy $h = e + p/\rho$, and pressure $p = \rho RT \sum_i y_i/M_i$, with M_i the molar mass of species i. The production term of species i is given by ω_i.

The properties of the species are computed assuming a rigid rotor and harmonic oscillator approximations; spectroscopic constants are taken from Gurvich[6]. The transport properties are computed following the Chapman-Enskog method. To estimate the viscosity and thermal conductivity, we solve the transport system using the conjugate gradient method. The collision integrals are computed using polynomials from Park[13]. This provide us only with $\Omega^{(1,1)}$ and $\Omega^{(2,2)}$; we have set $\Omega^{(1,2)}$ and $\Omega^{(2,1)}$ to zero. The diffusion fluxes have been computed with the following approximation for Fick's law:

$$D_{im} = \frac{1 - x_i}{\sum_j x_j / \mathcal{D}_{ij}} \tag{23}$$

where $\mathcal{D}_{ij}$ is the binary diffusion coefficient.

3.2. Boundary Conditions for the Stagnation line formulation

To complete the system, boundary conditions need to be established for the stagnation line formulation. The boundary conditions of interest for coupling to the control volume formulation are as follows:

Boundary condition at the edge:

At the stagnation line, the height of the boundary layer cannot be defined in terms of the streamwise velocity, and the size of the domain can be arbitrary as long as the assumption of constant pressure holds. Magin[10] defines the edge of the boundary at the stagnation line to be the inflection point of the velocity gradient that is either measured or obtained from a simulation.

At the boundary edge, we specify the species density, $\rho_i|_e$, the normal (to the stagnation line) derivative of the normal velocity, $u_{,1}|_e$, the temperature, T_e, as well as, $\partial u_{,1}/\partial y|_e$. The last term provides information about the shape of the heat-shield in the stagnation line approximation.

The normal velocity at the edge, $v|_e$, is computed by integrating from the wall to the boundary edge using the continuity equation. This insures mass conservation under the constant pressure constraint.

The gas composition at the boundary layer edge, $\rho_i|_e$, is assumed to be in chemical equilibrium. This assumption is valid for large bodies or when the shock is far from the body.

Boundary condition at the wall:

At the wall, the blowing velocity is computed from the relation $v_w = (\dot{m}_{ca} + \dot{m}_{pg})/\rho_w$ and the species mass fraction, $y_i|_w$, is obtained from the *TCV* formulation for a fixed T_w. We set $u_{,1}|_w = 0$, i.e. the pyrolysis gas is injected normal to the wall.

3.3. Change of variables

A common problem in reacting flows is that the temperature is needed to compute the properties of the gas, such as the transport coefficients D_{im}, μ, λ, and the production term ω_i, but temperature is not a conserved variable and needs to be derived from the internal energy. In addition, the density, ρ, is computed using the equation of state to ensure that the pressure, p, is constant in the domain. The vector unknown of interest is then: $\mathbf{U} = [v, \rho_i, u_{,1}, T]^T$.

Because the natural unknowns in the integration procedure is the vector of conserved variables $\mathbf{Q} = [\rho, \rho_i, \rho u_{,1}, \rho e]^T$, the following change of variables is required: $\delta\mathbf{Q} = \mathbf{\Gamma}\delta\mathbf{U}$, where $\mathbf{\Gamma} = \partial\mathbf{Q}/\partial\mathbf{U}$. This will lead to a singular matrix, but this has no effect since we are only interested in the steady-state solution. Our equations are written as follows,

$$\mathbf{\Gamma}\frac{\partial \mathbf{U}}{\partial t} + \frac{\partial \mathbf{F}(\mathbf{Q})}{\partial y} = \mathbf{S} \tag{24}$$

3.4. Numerical procedure: time and space discretization

The governing equations in conservation law form are solved numerically by means of a finite volume method. The first-order implicit (backward) Euler scheme is use to discretize in time. Second-order differences on a staggered mesh are used to discretize space.[14] The fully discretized equation for cell i at time step n is:

$$A_i \delta U_{i-1} + B_i \delta U_i + C_i \delta U_{i+1} = R_i^n \tag{25}$$

where $\delta U_i = U_i^{n+1} - U_i^n$ and the matrices A_i, B_i, C_i and vector R_i^n are:

$$A_i = -\frac{1}{\Delta y}\left(\frac{\partial F_{i-1/2}}{\partial U_{i-1}}\right)^n \tag{26}$$

$$B_i = \frac{1}{\Delta t}(\Gamma_i)^n - \left(\frac{\partial S_i}{\partial U_i}\right)^n + \frac{1}{\Delta y}\left(\frac{\partial F_{i+1/2}}{\partial U_i} - \frac{\partial F_{i-1/2}}{\partial U_i}\right)^n \tag{27}$$

$$C_i = \frac{1}{\Delta y}\left(\frac{\partial F_{i+1/2}}{\partial U_{i+1}}\right)^n \tag{28}$$

$$R_i^n = S_i^n - \frac{1}{\Delta y}\left(F_{i+1/2}^n - F_{i-1/2}^n\right) \tag{29}$$

The variables within cell i are coupled to their neighbors $i - 1$ and $i + 1$. Writing Eq. 25 for each cell gives us a block tri-diagonal system which is inverted using the generalized Thomas algorithm. This can be solved for each δU_i^n so that the solution can be advanced in time: $U_i^{n+1} = U_i^n + \delta U_i$. We note that we are not interested in the time-accurate evolution of the solution, the time dependence being kept only for convergence purposes.

All variables are cell-centered except for v which is computed at the interface (staggered grid) to ensure pressure-velocity coupling at low speed. This would not be possible by means of a preconditioning technique, since p is constant inside the boundary layer.

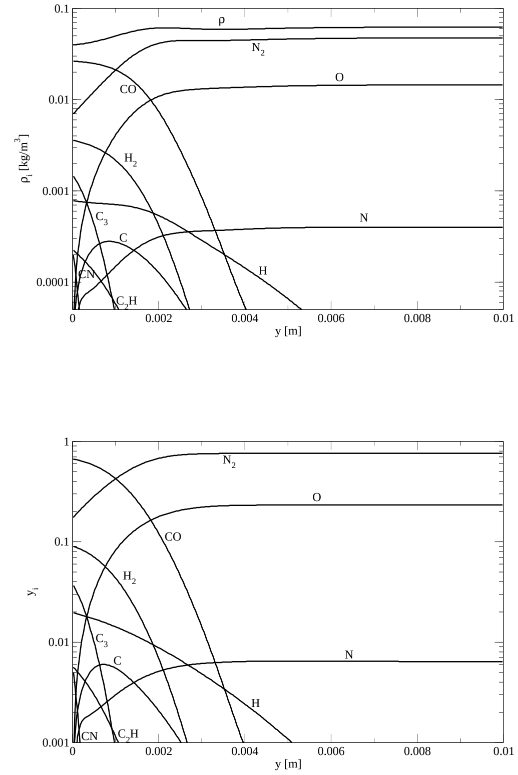

Figure 6: Species-density and mass fraction distribution at the stagnation line of a simulated VKI plasmatron[15] experiment on an ablative carbon-phenolic surface

3.5. *Simulation of an ablating sample in the VKI plasmatron*

We have implemented the stagnation-line formulation in a code that we call MUTATION-SL and have verified the implementation by comparing our results to results from the boundary layer code of Barbante [15]. In what follows, we present results for our simulation of the VKI "plasmatron" torch on an ablative material where we have set $p_e = 101325$ [Pa], $T_e = 4640$ [K], $u_{,1e} = 1143[\mathrm{s}^{-1}]$, $u_{,12}|_e = 82069.[\mathrm{m}^{-1}\mathrm{s}^{-1}]$. The wall was set at $T_w = 3200$ [K], with phenol mass injection of $m_{pg} = 0.1$ [Kg m^{-2}s^{-1}]. The velocity at the wall and at the boundary edge were computed to be $v_w = 2.21$ [ms^{-1}] and $v_e = 25.7$ [ms^{-1}] respectively.

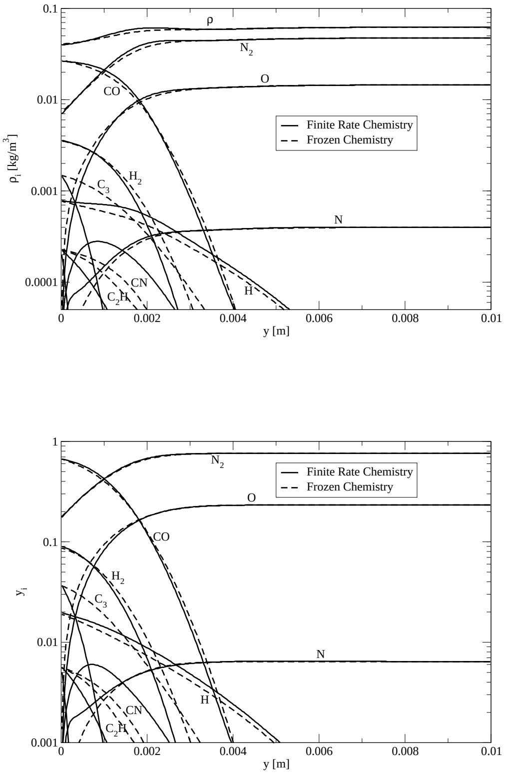

Figure 7: Effects of frozen chemistry compared to finite rate chemistry species-density and mass fraction distribution at the stagnation line of a simulated plasmatron [15] experiment on an ablative carbon-phenolic surface

Figure 6 shows the species mass fractions as a function of the distance from the wall. At the boundary layer edge we have mostly atomic oxygen and nitrogen entering the boundary layer. Some mass gets convected as seen in the total density of the N_2 profiles near the wall. It should be noted that it is hard to distinguish between convection and consumption of the species. However, we observe that the atomic species O and N become negligible at the wall. We have oxidation and nitridation as reflected in the profiles of CO and CN. All of the atomic oxygen, O, and atomic nitrogen, N, are consumed at the wall. The main reaction near the wall is the carbon oxidation reaction that produces CO: $C + O \rightarrow CO$. The second important species produced at the wall is hydrogen, H_2.

It observed in non-equilibrium Navier-Stokes simulations that frozen chemistry for air is a good approximation in the boundary layer. In Fig. 7 the composition profiles for frozen chemistry and finite rate chemistry (with and without the reaction term ω_i in Eq. 20) are compared. We find that frozen chemistry holds until the gas from the flow environment start to interact with the gas from the ablation products. We also observe that the slope of the two main species at the wall does not change. This is an indication that the concentrations of CO and H_2 are close to equilibrium, but the minor species, C_3 for example, is not. The implications of active chemistry near the wall may become important at high entry speeds where we expect high temperatures and higher blowing rates.

4. Computing B'-tables using the stagnation line formulation

The complete system of equations for the equilibrium boundary condition at the wall is given by Eq. 15; without the transfer potential approximation, the mass balance at the wall reads,

$$y_{k,w}(\dot{m}_{ca}) = \frac{\dot{m}_{pg} y_{k,pg} + \dot{m}_{ca} y_{k,ca} - j_{k,w}}{(\dot{m}_{pg} + \dot{m}_{ca})} \tag{30}$$

The strategy that we will follow is to compute the species diffusive flux at the wall $j_{k,w} = \sum_i \nu_k^i \frac{M_k}{M_i} J_{yi,w}$ from the stagnation line approximation.

4.1. Marching procedure

The boundary layer formulation as well as the *TCV* formulation require information from each other: the *Stagnation Line* requires v_w, y_{i_w}, and $j_{k,w}$; the *TCV* formulation requires $j_{k,w}$, as well as $\rho_e u_e C_M$.

To build a B'-table, we need to be able to fix B'_g and vary T_w. Our iteration strategy is shown schematically in Fig. 8,

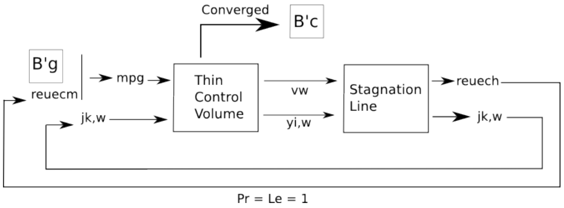

Figure 8: Marching strategy followed to compute the B'_c give B'_g

The simplest case to compare the formulation in MUTATION-B with the current formulation is for the case where $Le = Pr = 1$ is assumed to hold. In that case, the B'-table user assumes $\rho_e u_e C_M = \rho_e u_e C_H = \phi_w/(h_e - h_w)$. We start with the stagnation line approximation to compute the cold wall case. This gives us $r_e u_e C_M$. For a given B'_g, we compute $\dot{m}_{pg} = \rho_e u_e C_M B'_g$. Having $\dot{m}_{pg}$, we iterate to compute $y_{k,w}$ and $\dot{m}_{ca}$. Having, values for $\dot{m}_g$ and $\dot{m}_{ca}$, we can compute the velocity at the wall $v_w = (\dot{m}_{ca} + \dot{m}_{pg})/\rho_w$. The wall conditions are taken as input to the *Flow solver* which in turn gives us a new $\rho_e u_e C_M = \phi_w/(h_e - h_w)$ that needs to be iterated. Once the process has converged, we have $B'_c = \dot{m}_{ca}/\rho_e u_e C_M$. At this point we are ready to move to the next B'_g.

4.2. Preliminary B'-tables comparison

Because the transport properties are not known for all of the pairs of species present in the mixture that were used to produce Fig. 2, we have reduced the number of species to a set for which all the transport coefficients are available. We reduce the mixture of 19 species that we have discussed previously, to the 11 species set: C, H, O, N, CO, CN, C_2, C_2H, C_3, H_2, N_2.

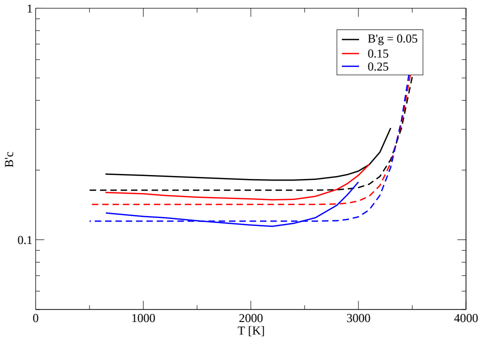

Figure 9: B'_c (char consumption rate) as a function of temperature for a range of B'_g (mass injection rate) rates for $p = 1atm$. The solid lines are from MUTATION-SL, the dashed lines are from MUTATION-B

Figure 9 shows a comparison between the stagnation line formulation in MUTATION-SL, and the formulation in MUTATION-B. We find surprising agreement between the two formulations given that the species profiles (shown in Fig. 6) show little similarity to each other. The B' generated by MUTATION-SL include the effects of blowing.

Figure 10 compares B'_c profiles computed using frozen chemistry to the profiles generated using finite-rate chemistry. These results are not surprising because we have seen that the effects of chemistry on the profiles of the major species are not strong, and that B'_c, in the diffusion limited regime, is a function of the atomic oxygen and atomic nitrogen supplied to the boundary, and these are the same for the frozen and equilibrium chemistry.

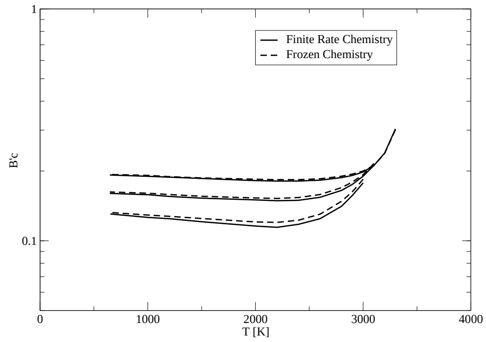

Figure 10: B'_c (char consumption rate) as a function of temperature for a range of B'_g (mass injection rate) rates for $p = 1atm$. Comparison between Finite Rate Chemistry and Frozen Chemistry

5. Summary and Conclusions

A stagnation line formulation has been developed to compute the gas surface interactions between an ablating surface and a chemically reactive flow. We find little effect of the treatment of chemistry on the species profiles for the conditions that we have considered. We also find that the frozen chemistry approximation yields reasonable results when compared to treating the chemistry with finite-rate reactions.

The classical *Thin Control Volume* formulation has been implemented in a way that easily couples to a stagnation line approximation (T, p, $\dot{m}_{pg}$ as input, $\dot{m}_{ca}$ as output). A procedure using the stagnation line approximation has been developed to evaluate the standard approximations used to build B'-tables. The new formulation builds into the B' tables the effects of blowing on the boundary layer transport.

We find that the tables are sensitive to the polynomials used to generate them. But at the conditions tested, the transfer potential approximation seems to hold surprisingly well.

Finally, comparing B'-tables using CEA data, JANAF data, and a rigid-rotor and harmonic-oscillator approximation, we find important differences at high-temperatures.

6. Acknowledgment

This research work will be sponsored by the European Research Council Starting Grant "*AEROSPACEPHYS: Multiphysics models and simulations for reacting and plasma flows applied to the space exploration program,*". I also wish to gratefully thank Dr. Nagi N. Mansour and Dr. Jean Lachaud for their contribition and advises on this project.

References

[1] Kendall, R. M., Barlett, E. P., Rindal, A. R., and Moyer, C. B., "An Analysis of the Chemically Reacting Boundary Layer and Charring Ablator. Part V: A General Approach to the Thermochemical Solution of Mixed Equilibrium-Nonequilibrium, Homogeneous or Heterogeneous Systems," *NASA CR-1064*, 1968.

[2] Göķcen, T., Chen, Y.-K., Skokova, K., and Milos, F., "Computational Analysis of Arc-Jet Wedge Tests Including Ablation and Shape Change," *AIAA Paper 2010-4644*, 2010.

[3] Gnoffo, P. A., Johnston, C. O., and Thompson, R. A., "Implementation of Radiation, Ablation, and Free Energy Minimization Modules for Coupled Simulations of Hypersonic Flow," *AIAA 2009-1399*, 2009.

[4] Gordon, S. and McBride, B. J., "Computer Program for Calculation of Complex Chemical Equilibrium Compositions and Applications I. Analysis," NASA Reference Punblication 1311, NASA, 1994.

[5] Chase, M. W. e. a., "NIST-JANAF Thermochemical Tables (4th ed.)," *Journal of Physical Chemical Reference Data*, Vol. 14, 1985.

[6] Gurvich, L. V., Veyts, I., and Alcock, C., Thermochemical Properties of Individual Substances Fourth Edition.

[7] Lachaud, J., Cozmuta, I., and Mansour, N. N., "Multiscale Approach to Ablation Modeling of Phenolic Impregnated Carbon Ablators," *Journal of Spacecraft and Rockets*, Vol. 47, No. 6, NovemberDecember 2010, pp. 910–921.

[8] Lachaud, J., Mansour, N. N., Ceballos, A., Pejakovic, D., Zhang, L., and Marschall, J., "Validation of a volume-averaged fiber-scale model for the oxidation of a carbon-fiber preform," AIAA Paper 2011-2223, 2011.

[9] Milos, F. S. and Chen, Y.-K., "Comprehensive Model for Multi-Component Ablation Thermochemistry," *AIAA Paper 97-0141*, 1997.

[10] Magin, T. E., *A Model for Inductive Plasma Wind Tunnels*, Ph.D. thesis, von Karman Institute for Fluid Dynamics, Universite Libre de Bruxelles, 2004.

[11] Milos, F. S. and Chen, Y.-K., "Ablation Predictions for Carbonaceous Materials Using CEA and JANNAF-Based Species Thermodynamics," *42nd AIAA Thermophysics Conference*, 2011.

[12] Cousteix, J., Aérodynamique - Couche limite laminaire, *Cepadues, 1997.*

[13] Park, C., "Chemical-Kinetic Parameters of Hyperbolic Earth Entry," *Journal of Thermophysics and Heat Transfer*, 2001.

[14] Munafo, A., "Vibrational State to State Kinetics in Expanding and Compressing Nitrogen Flows," *American Institute of Aeronautics and Astronautics*, 2010.

[15] Barbante, P. F., Accurate and Efficient Modelling of High Temperature Nonequilibrium Air Flows, Ph.D. thesis, *von Karman Institute for Fluid Dynamics, 2001.*